Development of a Numerical Tool for the Optimisation of Vascular Prosthesis towards Physiological Compliance

by

Helena van der Merwe

(Student Number: VMRHEL004)

SUBMITTED TO THE UNIVERSITY OF CAPE TOWN

in fulfilment of the requirements for the degree

MSc(med) in Computational Biomechanics

Faculty of Health Sciences

UNIVERSITY OF CAPE TOWN

Date: 24 January 2007

Supervisors: Dr. T. Franz, Prof. B.D. Reddy, Prof. P.P. Zilla

THIS THESIS IS DEDICATED TO:

My father and "Oupa Jannie"

The scientists who won't stop learning, a true inspiration.

DECLARATION

I, Helena van der Merwe, hereby declare that the work on which this dissertation is based is my original work (except where acknowledgements indicate otherwise) and that neither the whole work nor any part of it has been, is being, or is to be submitted for another degree in this or any other university.

I empower the university to reproduce for the purpose of research either the whole or any portion of the contents in any manner whatsoever.

Signature: Signed by candidate

Date: 23 May 2007

Acknowledgements

I would like to thank my supervisor Dr. Franz for his guidance and patience throughout the last two years, I have learnt a lot from him. I would also like to thank my co-supervisors Prof. Reddy for his guidance and support throughout this time and Prof. Zilla for his input and the opportunity to conduct my research at one of the best run internationally acknowledged research units.

I would like to thank Shaun Moore, who sometimes had to drag me through the frustrating times to make sure I complete the project, and for being there at when I made it through. My family, for always having a sympathetic ear, even though they are far away. My friends Louise Bezuidenhout and David Long, for dealing with my constant complaining towards the end and for struggling through endless drafts of this thesis.

I would also like to thank all my other colleagues at the CVRU, in particular Deon Bezuidenhout, for always being there to listen, Johann Eygelaar, for providing well needed conversation and comic relief and Dorothy Daws, for providing the "fuel that keeps us going" on Fridays.

Table of Contents

List of Figures

List of Tables

Glossary

Abluminal: Lying radially external in a blood vessel or graft

Anastomosis: The connection between a native artery and a vascular graft

Angioplasty: The repair of a blood vessel by inserting a balloon-tipped catheter to unclog it

Antigenic: Elicits an immune response

Aorta: Largest artery in the body. Runs from the heart.

Arterioles: Smallest type of arteries, found before capillaries in the vascular tree.

Arteriosclerosis: Arterial disease causing stiffening and dilation of the major arteries.

Arteriovenous Shunt: A passage of blood directly from arteries to veins, without going through the capillary network

Atherosclerosis: Arterial disease causing the narrowing of one or more major artery

Atrium: The heart chamber receiving blood

Austenite Phase: A material solid phase. The high temperature/low stress phase of SMAs.

Autologous: From the same organism

Cardiac Cycle: One complete heartbeat, consisting of one complete contraction and relaxation of the heart muscle.

Capillaries: Fine blood vessels between the arterial and venous system, where oxygen exchange between blood and cells takes place.

Collagen: An extracellular protein found in blood vessel walls, exhibited as fibres of high stiffness.

Compliance: Measure of radial dissention with respect to pressure change.

Dacron (PET): Polymer used to create woven or knitted vascular grafts.

De-endothelialisation: Stripping of the endothelial cell layer residing on the luminal surface of a blood vessel.

Diastole: Dilation of heart muscle during the cardiac cycle, related to low point of blood pressure

Distal: Further from the heart

Elastic Modulus: See Young's Modulus

Elastic: An object's ability to return to its original shape after the removal of a deforming load.

Elastin: A protein constituting the basic substance of elastic tissue. Found in blood vessel walls.

Embolism: The obstruction of a blood vessel by a clot.

Endothelial Cells: Cells lining the luminal surface of blood vessels, making up the endothelium.

Fatigue: Damage caused to a structure due to repeated load cycling.

Gastroepiploic Artery: Artery lying close to the stomach, sometimes used as a vascular bypass grafts.

Haemodynamics: The study of blood flow.

Heterologous: Derived from a different specie

Hysteresis: The area between the loading and unloading curve of a material.

In vitro: Performed experimentally in a controlled environment not in an organism

In vivo: Performed in an organism.

Internal Mammary Artery: Artery situated close to the heart, sometimes used as a vascular graft in coronary artery bypass surgery.

Intravascular: Inside a blood vessel

Intima: Inner layer of a blood vessel.

Intimal Hyperplasia: Wall thickening of a vascular graft, especially at the anastomosis.

Ischemia: Local deficiency of blood supply produced by vasoconstriction or local obstacles to the arterial flow.

Isotropic: Equal properties in all directions

Luminal: Lying radially internal in a blood vessel or graft

Martensite Phase: A material solid phase. The low temperature/high stress phase of SMAs.

Morphology: The study of the form and structure of an object.

Myointimal: Concerning the intima and media of a blood vessel.

Neo-Adventitia: The adventitial layer forming on a vascular graft after implantation.

Neo-Intima: The intimal layer forming on the luminal surface of a vascular graft after implantation.

Nitinol: A nickel-titanium shape memory alloy.

Occlusion: Closing/blocking of blood vessel or graft.

Patency: State of open

Pathologic: involving disease

Periphery (peripheral): Further from the heart

Plasticity: The deformation undergone by a plastic object as a result of stress application will remain after the removal of the stress.

Plaque: Fatty build up on the luminal surface of a vascular wall

Platelets: Red blood cells.

Prosthetic: a device, either external or implanted, that substitutes for or supplements a missing or defective part of the body

Proximal: Close to heart

Pulse Pressure: The difference between the systolic and diastolic pressure

Radial artery: Artery found in the arm

Recoil: To shrink back

Saphenous Vein: Vain found in the leg

Shape Memory Alloy: Metallic alloy exhibiting superelastic behaviour and the shape memory effect.

Shear Stress: Stress caused by force parallel to the surface

Stent: a small, expandable tube used for inserting in a blocked vessel or other part

Strain: Measure of the deformation of a body in response to an applied force.

Stroke Volume: The amount of blood that gets released from the heart into the arterial system during one cardiac cycle.

Stenosis: A constriction of a duct or passage.

Suture: A joining of the edges of a wound or the like by stitching or some similar process

Systole: The normal rhythmical contraction of the heart, during which the blood in the chambers is forced onward

Teflon (PTFE): Polymer used to create vascular grafts

Thrombus: A fibrinous clot that forms in and obstructs a blood vessel

Tunica Adventitia: External layer of a blood vessel.

Tunica Intima: internal (luminal) layer of a blood vessel.

Tunica Media: Middle layer of a blood vessel. Resides between the intima and the media.

Vascular Soft Tissue: Tissue constituting blood vessels

Vascular Bypass Graft: Conduit used to bypass a diseased blood vessel

Vasoconstriction: Narrowing of blood vessel

Vasodilation: Dilation of blood vessel

Vena Cava: Vein discharging blood to the heart

Venules: Small veins joining capillaries and larger veins.

Viscoelastic: pertaining to a substance having both viscous and elastic properties

Viscosity: The property of a fluid that resists the force tending to cause the fluid to flow.

Young's Modulus: A coefficient of elasticity of a substance, expressing the ratio between a stress that acts to change the length of a body and the fractional change in length caused by this force

List of Abbreviations

bcc:	Body Centred Cubic
bpm:	Beats per minute
CAD:	Computer Aided Design
ePTFE:	Expanded Polytetrafluoroethelene
FEM:	Finite Element Method
IH:	Intimal Hyperplasia
PET:	Polyethylene terephthalate
PU:	Polyurethane
SMA:	Shape Memory Alloy
SMC:	Smooth muscle cell
SIM:	Stress Induced Martensite
UMAT:	ABAQUS User Material

List of Symbols

A	Area
A_S	Austenite start temperature
A_f	Austenite finish temperature
$\mathbf{a}$	Acceleration
$\mathbf{B}$	Tensor for expressing strain in term of DOF
∂B	Boundary of body B
∂B_c	Boundary of body B with contact conditions
∂B_t	Boundary of body B with surface tractions
∂B_u	Boundary of body B with displacement conditions
$\mathbf{C}$	Largest displacement correction
C	Nitinol material constant
C_D	Diametric compliance
c	Damping factor
$\mathbf{M}^*$	Artificial mass matrix
D_1 and D_2	Diameter values
$\mathbf{D}$	Rate of deformation tensor
$\mathbf{D}^e$	Fourth order elasticity function
D_D	Convergence control parameter
D_B	Convergence control parameter
d	Distance between two contact surfaces
d_{crit}	Minimum distance allowed between contact surfaces
$\mathbf{E}$	Infinitesimal strain tensor
E_A	Austenite Young's modulus
E_M	Martensite Young's modulus
e	Euler's constant
F	Loading function
$\mathbf{F}$	Displacement gradient
$\mathbf{F}_{eff}$	Effective force on the reference point
$\mathbf{F}_x$	x-component of $\mathbf{F}_{eff}$
$\mathbf{F}_y$	y-component of $\mathbf{F}_{eff}$
$\mathbf{F}_v$	Viscous damping forces

$\mathbf{f}$	Force vector
$\mathbf{f}^B$	Body force acting on body B
G	Shear Modulus
g	Isoparametric coordinate
$H^1(B)$	Sobolev space
$\mathbf{I}$	Identity matrix
I_G	Convergence control parameter (ABAQUS)
I_L	Convergence control parameter (ABAQUS)
K	Bulk Modulus
$\mathbf{K}$	Stiffness Matrix
L	Length
$L_2(B)$	Function space
$\mathbf{L}$	Nitinol material parameter
M_S	Martensite start temperature
M_f	Martensite finish temperature
$\mathbf{m}$	Normal vector to a surface
$\mathbf{N}$	Nitinol material parameter
N_A	Number of annealings performed
$\mathbf{n}$	Normal vector to a surface
P	Pressure
q	Isoparametric coordinate
R	Radius
$\mathbf{R}$	Largest residual force
R_s	Flow resistance
r	Isoparametric coordinates
S	Length of $\mathbf{X}$
s	Length of $\mathbf{x}$
T	Temperature
t	Time
$\mathbf{t}_n$	Surface traction on boundary with normal vector $\mathbf{n}$
$\mathbf{u}$	Displacement vector
u	Element of a vector space
V	Volume
$\mathbf{v}$	Velocity
ν_A	Austenite Poison's ratio

ν_M	Martensite Poison's ratio
$\mathbf{W}$	Spin tensor
$\mathbf{w}$	Test functions
w	Elements of a vector space
$\mathbf{X} = (X_1, X_2, X_3)$	Initial position
$\mathbf{x} = (x_1, x_2, x_3)$	Position at time equals to t
α	Circumferential section of the graft that is modelled
$\boldsymbol{\alpha}$	Degrees of freedom
$\boldsymbol{\beta}$	Degrees of freedom
$\boldsymbol{\varepsilon}$	Total strain
$\boldsymbol{\varepsilon}^e$	Elastic strain
$\boldsymbol{\varepsilon}^{tr}$	Transformation strain
ε_L	Material parameter
ε^L	Transformation strain
$\boldsymbol{\varepsilon}'$	Scaled transformation strain
$\boldsymbol{\varepsilon}_V'$	Volumetric part of the scaled transformation strain
ε_V^L	Volumetric transformation strain
ε_d'	Deviatoric part of the scaled transformation strain
$\boldsymbol{\varphi} = \begin{bmatrix} \phi_1 \\ \vdots \\ \phi_r \end{bmatrix}$	Basis Vector
η	Nitinol material parameter
κ	Nitinol material parameter
λ_i	Eigenvalues
μ	Viscosity
ρ	Density
$\boldsymbol{\sigma}$	Cauchy stress tensor
$\boldsymbol{\tau}$	Tangential vector to a surface
$\boldsymbol{\omega}$	Angular velocity
ξ_S	Fraction of martensite phase present in a sample
ψ	Free energy function

Subscripts and Superscripts

X_0	Denoting initial state
$\dot{X}$	Denotes derivative
X^{AS}	Denotes austenite to martensite transformation
X^{SA}	Denotes martensite to Austenite transformation
X_S	Denotes start of transformation
X_S	Denotes end of transformation
X^r	Dimension of a vector space
$\hat{X}$	Denotes isoparametric element
X_m	Denotes the element index
X_L	Denotes loading
X_U	Denotes unloading

CHAPTER 1: INTRODUCTION

The circulation system forms a pivotal part of the functioning of the body, as it facilitates the transport of oxygen and nutrients to and the removal of carbon dioxide from the cells in the body. Every blood vessel has very specific mechanical properties which allow it to fulfil its role in the circulation system. Without the effective functioning of the blood vessels, this process is severely compromised and could have fatal consequences. Native blood vessels, and in particular arteries, are compliant, changing their diameter in response to a change in blood pressure during the cardiac cycle. This behaviour is attributed to their heterogeneous structure. They consist of different layers which in turn consist of different components. All the layers interact with each other and have different mechanical properties and the mechanical properties of arteries are therefore due to contributions from all these components.

Arterial degradation occurs with aging and disease, but various treatments are available e.g. angioplasty, intravascular stenting and arterial bypass grafting. This thesis focuses on vascular grafting. Commonly used existing vascular grafts are stiff and incompliant and as such do not allow adjustment of the luminal diameter in response to the systolic-diastolic blood pressure change. This difference between vascular grafts and native blood vessels has been identified to cause physiological problems after implantation.

It has been proposed that if a vascular prosthesis is to more closely approximate the mechanical behaviour of a native vessel, it should similarly feature a multi-component structure. One of the components could be a metal support structure, similar to an endovascular stent.

The objective of the project was to develop a numerical tool, using the Finite Element Method (FEM) to aid in the development and optimization of such a metallic support structure. This tool was used to simulate the behaviour of different designs under simulated in vivo conditions. The numerical results of the predicted mechanical behaviour are then analysed.

An approach is presented based on the underlying governing equations of mechanics and material behaviour. This approach is verified by a number of verification models and comparisons are made with techniques reported in the literature on intravascular stent

models [1-10]. These models resemble the structure considered in this thesis and differences in modelling strategy, resulting from the different outcomes required, are highlighted.

Models of six variations of the original geometry of the structure are created and analysed to highlight the ease with which the modelling approach can be applied. It is shown that none of the designs analysed exhibit optimum behaviour, and further evaluation of varied models is suggested.

In summary the aims of the thesis are:

- To create a numerical model, describing the wire support structure mentioned above, to aid in understanding the mechanical behaviour of the structure.
- To verify that the Finite Element Model is numerically stable.
- To formulate guidelines for creating such models
- To create models of different designs in order to analyse the variation in mechanical behaviour resulting from design variation.

The rest of the thesis will take the following form:

Chapter 2 presents the relevant theory underlying the problem. General background is given on a healthy circulation system as well as the structure and functioning of arteries and veins within this system. Next an introduction on arterial diseases is presented, followed by a discussion on currently used vascular prosthesis and their shortcomings. The mathematical background underlying the Finite Element Method (FEM) is given as well as a mathematical description of the material behaviour of Nitinol. A literature review on previous FEM models created to analyse the mechanical behaviour of intravascular stents concludes this chapter. Chapter 3 presents the experimental material model determination as well as the modelling procedures used in the thesis. A detailed description is given of the modelling procedure proposed for analysis of the metallic support structures, followed by description of the application of this procedure in the analysis of different designs. Models used in the verification of the numerical procedure are also described. Chapter 4 summarises the results of all the different models, which are then discussed in Chapter 5. This chapter also discusses the modulating strategies used with respect to verification and compares them to literature. A comparison to previously conducted experimental tests of the analysed structures is also made followed by a

description of the relevance of the results to the medical field. Concluding remarks follow in Chapter 6.

CHAPTER 2: THEORY

2.1 Biological Theory

2.1.1 Circulation

The heart and circulation system function as a transportation system to deliver oxygen from the lungs to the different cells of the body and to carry carbon dioxide away from the cells back to the lungs. The system forms a closed loop, with the heart as the driving force behind the motion of the blood through the system [11, 12].

The heart consists of 4 chambers, a right and left atrium and a right and left ventricle, as shown in *Figure 2-1*.

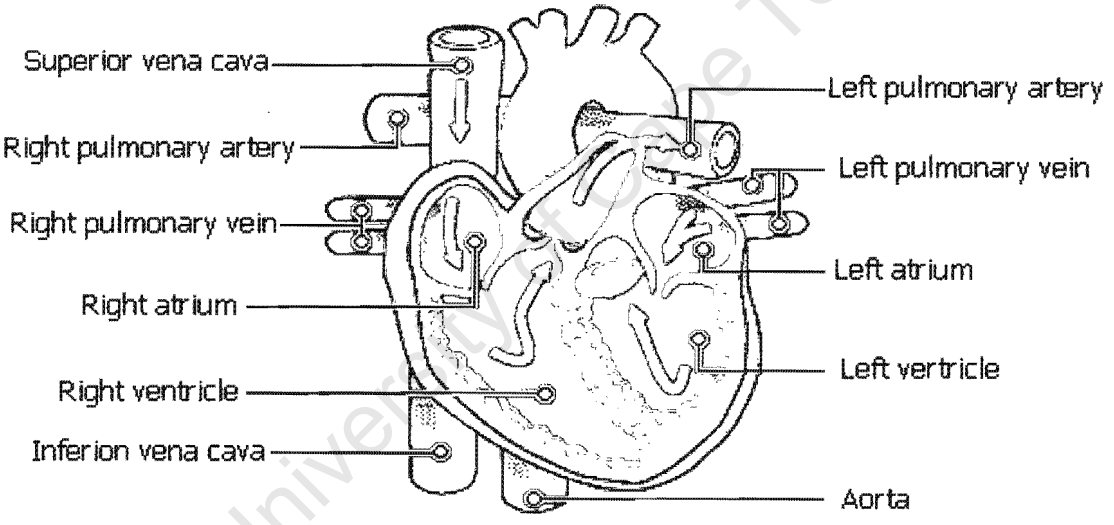

Figure 2-1: The structure of the heart (adapted from [13]).

Blood flows through the heart as a result of contraction (systole) and relaxation (diastole) of the heart muscles. The same events occur in the left and right side of the heart at different time intervals, the only difference being that the pressure in the right side is much lower than that of the left side. The process here is described for the left of the heart, with the corresponding terms for the right side of the heart in brackets. Throughout ventricular diastole, blood flows from the left (right) atrium to the left (right) ventricle with the mitral (tricuspid) valve remaining open. The pulmonary (aortic) valve remains

closed during diastole as the pressure in the atrium is lower than that in the aorta (pulmonary artery). During early ventricular diastole, the atrium is also in diastole and blood flows into it from the pulmonary vein (vena cava). During late diastole, the atrium is in systole, forcing blood into the ventricle through the mitral (tricuspid) valve. At the end of ventricular diastole, the mitral (tricuspid) valve closes and ventricular systole occurs. The contraction of the ventricle causes its internal pressure to rise above that in the aorta (pulmonary artery) and results in the aortic (pulmonary) valve to opening to release blood into the aorta (pulmonary artery). The volume of blood pumped out of the each ventricle during ventricular systole is termed the stroke volume. At the end of ventricular systole the aortic (pulmonary) valves closes. The pressure inside the ventricle drops as it relaxes and the mitral (tricuspid) valve opens as soon as this pressure falls below that of the atrium while the aortic (pulmonary) valve closes as soon as the pressure falls below that in the aorta (pulmonary artery). This process occurs cyclically over time and the pressure variation with respect to time, during one cycle, is referred to as the cardiac cycle [14].

The circulatory system can be divided into the pulmonary and systemic circulations as shown in *Figure 2-2*. The pulmonary artery, pulmonary vein and exchange region within the lungs make up the pulmonary circulation. The remaining parts of the circulatory system make up the systemic circulation. The pulmonary circulatory system will not be discussed further here, as the current work deals only with vascular grafting in the systemic circulatory system and when referring to circulation, systemic circulation is implied [14, 15].

The systemic circulation consists firstly of an arterial system, which transports the oxygen rich blood from the heart to the capillaries, where oxygen exchange takes place. From the capillaries, a venous system carries the carbon dioxide rich blood back to the heart [11, 14, 15].

All the arteries in the systemic circulation stem from the aorta, either directly or indirectly. They are arranged in such a way as to allow independent adjustment of blood volume to each organ as required. This takes place through vasoconstriction and vasodilation, governed by smooth muscle cells (SMC) in their walls. This adjustment helps to keep the total systemic arterial pressure constant even when the needs of the different organs change [11, 14, 15].

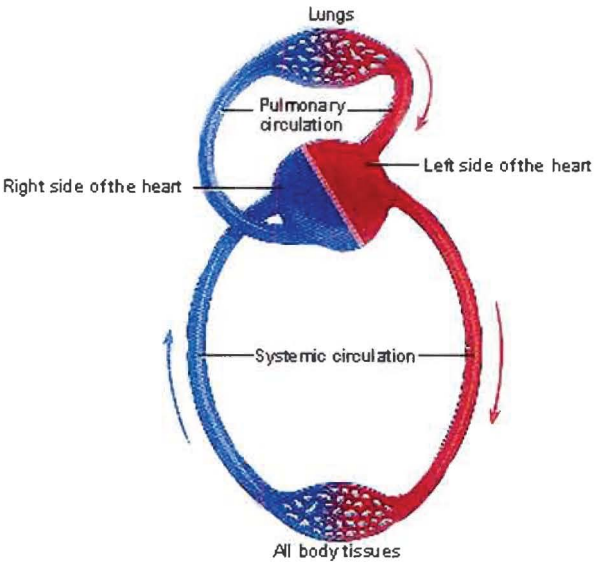

Figure 2-2: Systemic and Pulmonary circulation (adapted from [16]).

Other than regulating flow, the arteries also perform a cushioning function. During the cardiac cycle the pressure and flow velocity of the blood entering the arterial tree vary with time such that the peak values are much greater than the mean values. The variation in pressure compels the heart to deliver much more power to the system than would be needed if a more constant flow was maintained because blood has to be constantly accelerated and decelerated. The pressure variation can also be damaging to the endothelial cells, as it causes a larger drag force to be imposed on them [17, 18].

These negative effects can be minimised if flow towards and through the peripheral capillary bed approaches steady flow. This is achieved physiologically through the elastic properties of the arteries, which provide passive extension and elastic recoil. The elastic properties of the different arteries differ due to a gradual change in the artery structure from the aorta to the periphery. The structural differences will be discussed in more detail in the Section 2.1.2.

Major vessels (closer to the heart) act as an elastic reservoir. Each time the heart contracts to release blood (systole) they expand to accommodate the volume of the blood released from the left ventricle. When the aortic valve closes at the end of systole, these major arteries release the stored blood by elastically recoiling throughout the diastole phase in order to maintain blood flow. This means that the variation in flow and pressure of the blood occurring during the cardiac cycle is dampened by the expansion and elastic recoil of arteries. The dampening of the pressure variation is equivalent to a reduction in pulse pressure (difference between systolic and diastolic pressures). As the blood moves

through the arterial tree towards the periphery, the flow and blood pressure becomes steadier. This is a result of the combined pulse pressure reducing effect of the arteries through which the blood has passed. The aorta, being the most proximal of all the arteries, expands to accommodate nearly two thirds of the stroke volume. In the arterial circulation of a healthy young human systolic pressure is around 120mmHg and diastolic pressure is around 80mmHg (measured in the brachial artery) [11, 17-19].

Even though the major arteries are more elastic and are responsible for most of the pulse pressure reduction, the more peripheral arteries also contribute, albeit a smaller amount, to the pulse reduction process. On the other hand, most of the flow regulation takes place in the peripheral arteries by means of vasodilation and vasoconstriction. The arterioles have the smallest radii of all the arteries in the arterial system and they are responsible for most of the resistance to flow in the circulatory system. Flow resistance is given by

$$R_s = \frac{8\mu L}{\pi R^4} \tag{2.1}$$

where R_s is the vascular resistance, μ is the blood viscosity, L is the length of the vascular channel (constant), R is the blood vessel radius [20]. From equation (2.1) it can be seen that flow resistance is inversely proportional to the fourth power of the vessel radius. This means that even a small difference in vessel radius can have a large effect on the resistance, with larger radii leading to decreased resistance [20, 21].

From the arterioles, blood moves to the capillaries where the blood flow velocity is much smaller. The total combined cross-sectional area of the vessels at the capillary level is larger than that of the preceding levels of arteries, but the same flow rate is still maintained. This principle is illustrated by the definition [14, 20]

$$\text{Flow Rate} = \frac{\text{Flow Velocity}}{\text{Crossectional Area}} \quad . \tag{2.2}$$

After oxygen exchange has occurred in the capillaries, blood moves through the venous system back to the heart. The total cross-sectional area of the venous system gradually decreases towards the heart, increasing the blood velocity. Veins have much larger radii than arteries at the same level and the venous system contains the largest portion of the systemic blood volume (about 80%). This means that even large changes in blood volume leads to only relatively small pressure variations in the venous system [11, 14].

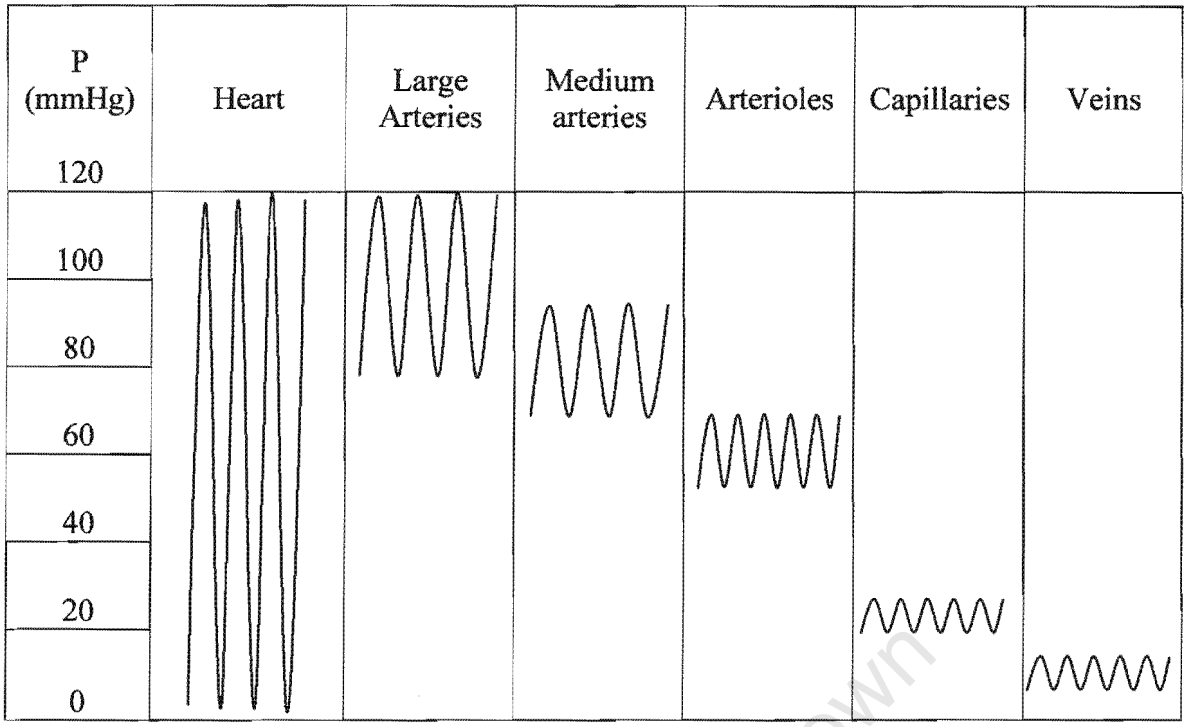

Figure 2-3: Pressure variation in circulatory system (adapted from [11])

2.1.2 Vascular Soft Tissue

The main components of vessel walls are elastin (elastic proteins), collagen (stiff reinforcing fibres) and SMCs. Elastin is highly distensible with and elastic modulus of approximately 1MPa while collagen is relatively stiff in comparison, with an elastic modulus of approximately 100MPa. In a vessel wall subjected to zero pressure loading, elastin layers are observed to be wavy and disorganised. As pressure (and therefore distension) increases from zero, these elastin laminae straighten and inter-laminar distance decreases. When the distending pressure reaches approximately 80mmHg the elastic laminae are straight and appear as concentric cylinders with uniform thickness and spacing. The number of elastic laminae in each vessel varies according to specie and position only. The thickness of the laminae, and not the number of laminae, increases with age [17, 18, 22].

The mechanical behaviour of blood vessels exhibits a hysteresis between loading and unloading curves. For arteries, this hysteresis relates to the energy that is stored in the vessel wall during circumferential extension in the systolic (loading) phase, which is again released by the vessel wall during elastic recoil in the diastolic (unloading) phase. Blood vessels exhibit non-linear mechanical behaviour (see *Figure 2-4*) since the elastic stiffness, described by Young's modulus, increases with the applied load. The Young's

modulus is thus not a constant, but can be described as a function of strain. The non-linear behaviour of vessel walls is brought about by their composite structure and depends on the relative proportion, spatial organisation and material properties of each component in the structure. The initial distensability of the vessel is related to the elasticity of the elastin, but as the vessel is distended the initially wavy collagen fibres are straightened out and their contribution to the total wall stiffness increases causing the compliance to decrease. The compliance value for an artery is used to describe its distension in response to applied pressure and is defined by

$$C_D = \frac{D_2 - D_1}{(P_2 - P_1)D_1} \times 100 \times 100 \tag{2.3}$$

where C_D is the diametric compliance, D_1 is the diameter of the vessel at internal pressure P_1, D_2 is the vessel diameter at internal pressure P_2 and the compliance is expressed in % per 100mmHg [19, 23, 24]. Diametric compliance is defined in (2.3) and will be always be implied in this document when speaking of compliance.

The region of transition from low to high stiffness corresponds to the mechanical recruitment of the collagen fibres in the vessel wall (see *Figure 2-4*). The distension of the vessel wall thus gives rise to a load transfer from the elastin laminae (indicated in purple) to the collagen fibres (indicated in blue) [17-19]. In the case of uniaxial tensile testing of an artery a pressure-strain curve as the one shown in *Figure 2-4* will be obtained demonstrating the non-linear behaviour. The tensile stresses will be distributed fairly uniformly throughout the thickness of the wall.

Since veins consist of the same material as arteries, they will undergo a similar response. Veins however consist of different proportions of the materials (more collagen, less elastin) because physiologically they have to operate at different pressures in vivo. The collagen's properties will be recruited at much lower pressures and the hysteresis will therefore be present at a lower pressure range.

Compliance is an important mechanical property of vascular soft tissue. Diametric or volumetric compliance can be reported, but in this work diametric compliance is used. It is also approximated to be linear over the physiological (or other relatively small range) and apply only to the pressure range P_1 to P_2. A vessel's compliance is a measure of how easily it dilates in response to internal pressure increases [12]. In human femoral arteries

a compliance value of 5.3 ± 0.5 %/100mmHg has been reported, but the pressure range to which this applies has not been given [25]. Another documented value for arterial compliance is 8.1±5.9 %/100mmHg over the pressure range 30 to 100mmHg, but the position of the artery is not documented [26]. The compliance of the human vein is documented as 4.4±0.8 %/100mmHg in the saphenous vein over an unknown pressure range [25] and 5.0±6.7 %/100mmHg over the pressure range 30 to 100mmHg at an unknown position [26].

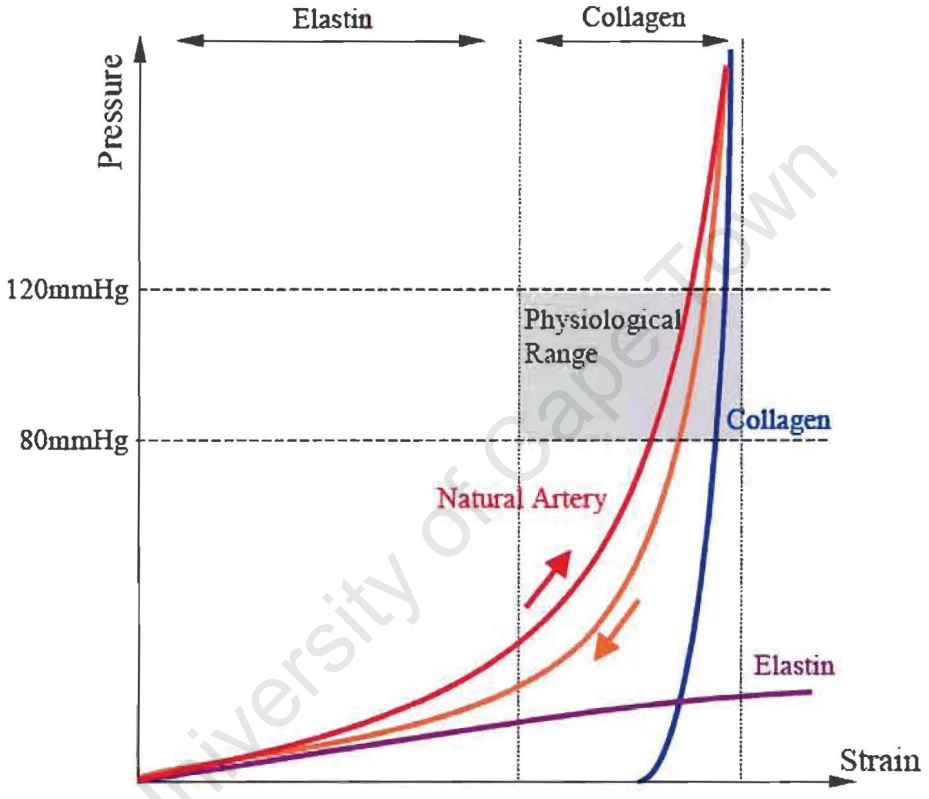

Figure 2-4: The non-linear behaviour of an artery and the dependence on elastin and collagen fibres [27].

Blood vessels consist of three different layers as shown in *Figure 2-5*. On the inside of the vessel lies the Tunica Intima which consists of a layer of endothelial cells, lying luminally to a thin basal lamina, which consists mostly of collagen fibres. On the outer surface of the basal layer lies a sub-endothelial layer consisting of loose connective tissue, elastic fibres and fibroblasts and a few SMCs. The sub-endothelial layer separates the Tunica Intima from the Tunica Media where the Tunica Intima lays luminal to the Tunica Media. Elastic laminae separate the media into a varying number of well-defined,

concentric, fibre-reinforced, layers each consisting of a complex three dimensional network of SMCs, collagen and elastin. The smooth muscle fibres are arranged in a helical fashion with a small pitch that leads to an almost circumferential orientation. The elastin and collagen fibres are not connected to each other, but are both connected to the smooth muscle fibres. The Tunica Media in turn lays luminal to the Tunica Adventitia, which is made up predominantly of thick bundles of wavy collagen fibres loosely arranged in a helical pattern. At low blood pressures the adventitia is less stiff than the media, but as the pressure increases the collagen fibres straighten out until the adventitia lends a greater contribution to the overall wall stiffness than the media. [22, 28].

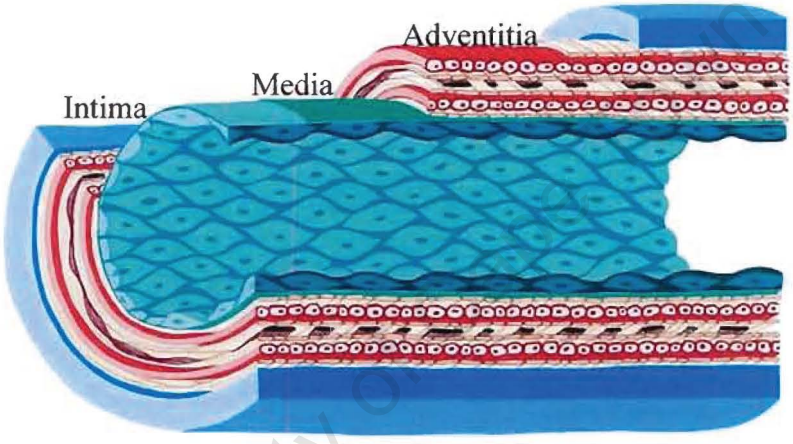

Figure 2-5: Layers of an artery [18].

2.1.2.1 Arteries

The non-linear behaviour and high distensability of artery walls is the source of their elastic stability and helps to protect against aneurysms and "blowouts". As the pressure increases in the artery, the wall becomes more rigid due to non-linear decrease in compliance. "Blowouts" in healthy adult arteries of humans are only predicted as distending pressures approach 1000mmHg, which is just under ten times normal blood pressure [17, 18]. The elasticity of arteries decreases towards the periphery as does the elastin to collagen ratio [19]. Arteries can be subdivided into 3 categories according to their structure, even though in reality the changes in structure occur gradually along the arterial tree. They all contain the three layered structure described previously and the differences in structure are highlighted in the following descriptions:

1) Large (elastic) arteries

These arteries contain a high proportion of elastic tissue and therefore have a high compliance. This leads them to be the category with the biggest influence in the pulse pressure reduction. They are low resistance conduits for blood transportation from the heart to the muscular arteries. Their walls are relatively thin (about 1/10 of the vessel outer diameter). The sub-endothelial layer is so thin that the interface between the intima and media is ill-defined. The media comprises the greatest proportion of the vessel wall, and can contain between 40 and 70 elastic laminae. The adventitia comprises a relatively small proportion of the artery wall and the collagen fibres are not highly organised [19, 28].

2) Medium (muscular) arteries

These arteries contain a high proportion of muscular tissue and have a smaller effect on pulse pressure decrease than elastic arteries. Their high proportion of SMCs make them useful in the regulation of blood flow to different areas in the systemic circulation as these muscle cells can dilate and constrict the artery in response to nerve signals. The majority of arteries belong to this class. The vessel wall is thicker than that of elastic arteries and represents around one quarter of the total vessel outer diameter. The proportion of sub-endothelial layer present becomes less with decreasing vessel diameter. The media is mostly muscular and consists of 10 to 40 concentrically arranged helical layers. The elastic laminae are thin and decrease in number towards the periphery. The adventitia makes up a greater proportion of the vessel wall than in elastic arteries, but the media is still thicker than the adventitia [28].

3) Arterioles

The arterioles are the smallest vessels in the artery class and transport blood from the muscular arteries to the capillary bed. Their combined surface area is the highest in the arterial tree and due to frictional forces they therefore constitute the biggest proportion of resistance in the system. They offer a very large contribution to the arterial pressure. Their intima consists of the endothelium and a very thin basal layer and subendothelial layer. In most cases the media consists of only one, but sometimes two layers of SMC's which are layered between thin basal laminae and some collagen fibrils. They also have a very thin adventitia [28].

2.1.2.2 Veins

Although veins have the same 3 layered structure as arteries, they differ slightly in structure since they function in an environment with a much lower blood pressure and flow. The interfaces between the layers are much less defined than in arteries [17, 18, 28, 29].

Their compliance is much higher at venous pressures than the compliance of arteries at arterial pressures. Due to this high compliance their diametric response to an increase in distending pressure allows virtually no change in overall venous blood pressure, even with relatively large changes in blood volume. At arterial pressures, veins are much less compliant than arteries since their compliance increases more rapidly with distending pressure than that of arteries. This is due to the differences in their wall structure; veins have thinner walls, which unlike arteries, collapse when they are empty. Veins are also much more sensitive to vasodilators and vasoconstrictors than arteries [14, 15, 29, 30].

Veins are also subdivided into different categories. From capillaries, blood flows to venules and then to veins whose size increase from the periphery to the heart. Structure is less dependent on the size of the conduit in veins than in arteries. They generally have a much thinner media relative to wall thickness than arteries [11, 15, 17, 18, 28, 29].

1) Venules

Pericytic venules transport blood from the capillaries to muscular venules. Their intimae are thin, although the muscular venules' intimae are slightly thicker than that of the Pericytic venules. In Pericytic venules the media is practically non-existing, while muscular venules have a media consisting of one or two layers of SMC's with little collagen and elastin. Pericytic venules have a thin adventitia compared to the adventitia of muscular venules, whose adventitia is thick relative to the vessel wall thickness [28, 29].

2) Small veins

Their diameters vary between 0.2mm and 1mm. The intima is thin and the media contains two to four layers of SMCs interspersed between a thin network of elastin and collagen. The adventitia contains collagen bundles and some elastic fibres [28, 29].

3) Medium sized veins

They vary in diameter between 1mm to 10mm and their wall thickness represents only one tenth of their outer diameter. They too have a thin intima; to which valves are attached to prevent blood flowing in back towards the periphery. The media consists of two to four layers of SMCs separated by bundles of collagen and a delicate network of elastin. The adventitia is thicker than the media [28].

4) Large veins

These veins are larger than 10mm in diameter. The intima is the same as in medium sized arteries and also contains valves. The media is thin and may even be absent in some areas of the vena cava but otherwise is similar to that of medium sized arteries. The adventitia makes up the largest percentage of the wall thickness and consists of thick bundles of elastin and collagen fibres arranged longitudinally [28].

2.2 Introduction to Arterial Diseases

Arterial degeneration occurs with aging and disease. There are two main arterial diseases: Atherosclerosis and Arteriosclerosis.

Atherosclerosis is the narrowing of a major artery that causes ischemia or infraction of the organ or tissue downstream of it. It occurs locally, affects mainly the intima and is occlusive and disturbs the conduit function of the artery. An area of atherosclerotic plaque rupture exposes intimal elements below the endothelium to the circulating blood which can cause the development of an occlusive thrombus. It has been suggested that localised atherosclerosis is caused by shear stress alterations in the artery wall. The plaque which forms as a result causes a flow disturbance which increasingly alters the shear stress, causing further plaque growth and the process becomes self-perpetuating. Atherosclerosis mainly occurs when arteries, poorly supported by connective tissues, are subjected to repetitive bending or where a relatively narrow artery is subjected to rapid variable flow. Important factors in the development of atherosclerotic plaque are the expansion of the vessel wall, the drag on the vascular interface, bending and flexing, presence of secondary flow, and highly variable shear stress [21]. It has been suggested that atherosclerotic arteries have larger diameters than their normal counterparts possibly

in an attempt to increase luminal area due to the high circumferential stress experienced through conduit narrowing [31].

Arteriosclerosis is the stiffening and dilation of major arteries. It is diffuse, dilatory and mainly affects the media, but leads to dilation of the whole artery. It does not affect the conduit function of the arteries, but disturbs the dampening function. The disturbance in the dampening function leads to disruption of the pressure profile that occurs during the cardiac cycle which in turn causes an increased load on the heart. Increased arterial stiffness causes reflection waves from the periphery to return during systole, further augmenting the systolic pressure. It occurs due to the mechanical weakening of elastin fibres in the arteries. Muscular arteries which contain less elastin therefore undergo much less degeneration of this kind than elastic arteries [19, 21].

Different treatments are available for diseased arteries; including balloon angioplasty, internal stenting, as well as vascular grafting. Intravascular stents are inserted to maintain vessel patency as recoil of the artery can occur after balloon angioplasty [1, 32, 33]. This work deals with a proposed technique of numerically investigating proposed components of vascular grafts and therefore only vascular grafts will be discussed.

2.3 Vascular Grafts

Vascular grafts are used to augment insufficient functioning of blood vessels. The demand for vascular grafts has been estimated to be over one million cases per year world wide. Graft failure generally occurs due to thrombosis and/or occlusion. Intimal hyperplasia (IH) is the main cause of thrombotic complications in vascular grafts within the first two years and is mainly a result of SMC migration and proliferation [13, 34-41].

The difference in mechanical properties of host arteries and vascular grafts produce changes in the shape and amplitude of the pulse wave at the junction of the two tubes. This leads to increased stress and altered haemodynamics at the anastomosis, where IH is most likely to form. More IH is experienced at the distal than at the proximal anastomosis. Circumferential wall deformation and wall shear stress variations have all been identified as contributing factures to wall thickening while altered haemodynamics and injury of the vessel during suture can cause endothelial denudation. Endothelial cell damage in the presence of wall thickening stimuli leads to IH and eventual graft failure [23, 34, 35, 37-39, 41-52].

Compliance mismatch can lead to endothelial cell damage as well as altered haemodynamics. Grafts usually have a lower compliance than the artery which they replace would have in a healthy state. A general problem experienced due to the lack of compliance is the reduction in pulsatile energy. The vascular system requires the exact amount of pulsatile energy to be delivered to the periphery, in order to both overcome peripheral resistance of the capillaries while at the same time not placing too much stress on the periphery with greatly increased pulsatility. A hyper-compliance zone forms just proximal and distal of the anastomosis presumably due to the suturing in this area. There is a strong correlation between degree of compliance matching and graft patency as can be seen in *Table 2-1* [23, 24, 35, 43-47, 49, 51-53].

Table 2-1: Vessel compliances and patency [25, 43-45, 47].

Vessel	Compliance	Patency
Host artery	5.33 ± 1.15	
Saphenous vein	4.08 ± 0.65	82 ± 6 %
Dacron	1.9 ± 0	47 ± 15 %
ePTFE	1.6 ± 0	39 ± 19 %

Compliance mismatch is not the only cause of flow disturbances; diameter mismatch between the graft and artery will also cause flow disturbances and altered haemodynamics which have been implicated in promoting IH. Flow disturbances can cause changes in haemodynamics and vessel wall shear stress. Size matching between the implanted graft and the native artery is therefore a very important consideration [35, 43, 44, 48, 52, 54].

Wall shear stress that is either too high or too low can cause IH. While increased shear stress leads to endothelial damage, decreased shear stress causes areas of relative stasis between the blood and vessel, where excessive interaction between platelets and the vessel wall can occur. From this it can be postulated that there must exist an optimal wall shear stress at which no wall thickening will occur. Reduction in wall shear stress can also be a result of a lack of compliance. Not only can an absolute change in wall shear stress result in wall thickening, but also an increase in wall shear stress pulsatility. A more pulsatile wall shear stress, which could result from compliance mismatch between the graft and the artery, can lead to increased vessel wall thickening. There have also been suggestions that it is not changes in wall shear stress alone causing IH, but that the interactions between the wall shear stress and the circumferential strain can be

implicated. It has also be shown that the interaction between flow velocity and pressure plays a role, which is a similar result as flow velocity is a determinant of shear stress and pressure a determinant of circumferential strain. [34, 35, 38, 41, 43-45, 47, 49, 51, 52, 55, 56].

Some non-mechanical factors can also give rise to IH including thrombogenicity, absence of vascular endothelium and non-biocompatibility. Vessel wall damage during suture causes endothelial cell damage acting as a stimuli for the onset of IH [43, 44, 49, 50, 57].

Two other important considerations for the design of vascular grafts are: (1) their structural integrity to withstand pressure at the suture line (to prevent suture pull out) and (2) sufficient resistance to kinking and flattening in order to retain open lumen [36].

Vascular grafts can be subdivided into two main categories namely bioprosthetics and synthetic grafts. Bioprosthetic grafts are of biological origin and are composed mainly of autologous, homologous of heterologous tissue. These grafts are sometimes also cross-linked with fixatives and/or reinforced with synthetic materials. Synthetic grafts comprise entirely or mostly of synthetic materials [36].

2.3.1 Bioprosthetics

Autologous vessels (native veins and arteries) remain the grafts of choice in vascular surgery, with saphenous vein the best option in most cases and the Internal Mammary artery also used routinely to replace the coronary artery specifically. Radial and Gastroepiploic arteries are sometimes used as vascular grafts. The Radial artery is usually used to replace the right Internal Mammary Artery and is useful due to its diameter, length, safety, ease of harvest and encouraging mid-to-long-term results. Autologous vessels are either excised and re-implanted, or left in situ with only the distal or proximal ends repositioned and anastomosed to bypass the occluded artery [23, 24, 36, 37, 52, 57-61].

There are various problems associated with implanting veins into the arterial circulation. They undergo degradation when exposed to the arterial circulation environment. Shortly after implantation a vein will over distend to its limit, followed by myointimal thickening in a process termed arterialisation. Thereafter re-endothelialisation will typically take place. Due to the overdistention caused by the pressure increase, a vein graft acts as a

rigid tube in the arterial circulation [31, 36, 38-40, 43, 44, 50-52, 59, 62-64]. Arterialisation is in response to different wall thickening factors associated with arterial circulation. The increased pressure in the arterial circulation, causing veins to undergo greater circumferential deformation than in the venous circulation, is known to be a primary stimulus for myointimal thickening. Prolonged cyclic stretching of a vein graft is also known to promote vessel wall thickening. It has been shown that an increase in wall tension is more strongly related to medial thickening while shear stress changes more strongly correlated to intimal thickening. Decreased flow velocity is another stimulus which causes wall thickening, while increased flow velocity has been implicated in dilation of vein grafts over time. Low flow could increase wall thickening due to increased interaction time between blood and graft wall cellular elements. It has been suggested that the flow waveform, more than the absolute flow velocity, has a major impact on the wall thickening [31, 34, 38, 39, 41, 43, 49-51, 53, 54, 57, 65, 66].

A few weeks after implantation the vein graft thickness usually reaches equilibrium where the luminal radius and the wall thickness equals a relatively universal value for all the arteries in the patient. In 50% of vein grafts however the adaptive wall thickening becomes pathologic to the extent that the main problem associated with vascular grafts is the formation of IH. By ten years only 50 to 60 % of Saphenous vein grafts remain patent and of the patent grafts another 50% is significantly stenosed [23, 31, 34, 38, 40, 51, 52, 54, 57, 63, 66, 67].

Reduction in wall thickening is a key goal in preventing vein graft failure. The mechanical factors associated with wall thickening and the formation if IH has already been discussed. Other problems encountered when using vein grafts are the limited number of veins available for use (without causing venous circulation disturbances) while the available veins may be unusable due to preexisting conditions [36, 37, 43, 62].

Tests have also been conducted to develop an off-the-shelf conduit scaffold which can be subsequently seeded with autologous vascular cells. Decellularised vein has been tested as a possible scaffold to this end. The decellularisation process has been shown to decrease antigenicity, reducing the risk of graft rejection and does not significantly alter the morphology of the vessel so that burst strength and suture pull-out is not influenced. The negative point to this approach is the time taken to seed such a scaffold making these grafts unusable at short notice [61].

In heterologous grafts, changes occur that resemble atherosclerosis and they are less reliable as autologous grafts. These grafts were however used in various forms before the development of synthetic grafts. The use of heterologous arterial tissue is limited mostly to arteriovenous shunts [36].

2.3.2 Synthetic Grafts

There is widespread use of Dacron (PET) and Teflon (ePTFE) grafts in vascular surgery [24, 43, 44, 57, 62]. Dacron grafts consist of crystalline filaments bundles into multifilament yarns which are then either knitted of woven to produce tubular grafts pictured in *Figure 2-6*. The knitted grafts are less prone to fraying than the woven ones while the woven grafts are less prone to kinking. ePTFE grafts consist of a solid nodes linked by inter-connecting fibrils pictured in *Figure 2-7* [36].

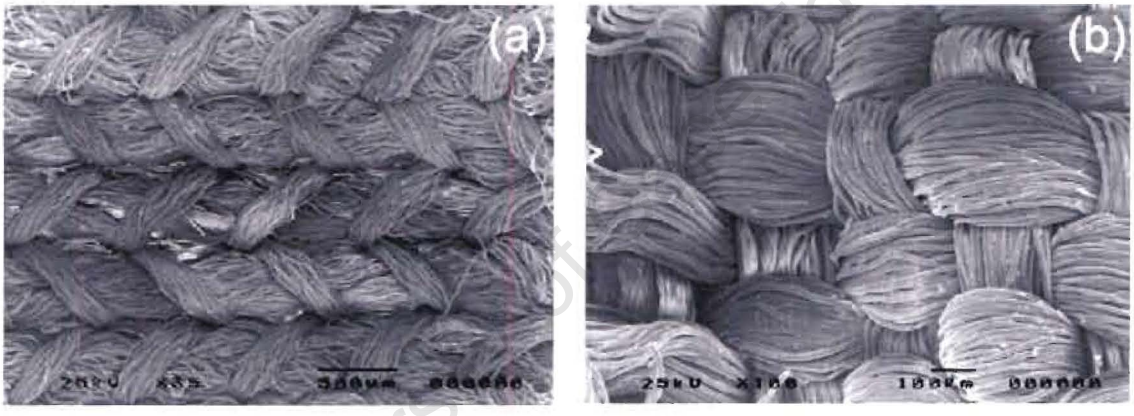

Figure 2-6: Electron microscope images of portions of (a) a knitted Dacron graft and (b) a woven Dacron graft [36].

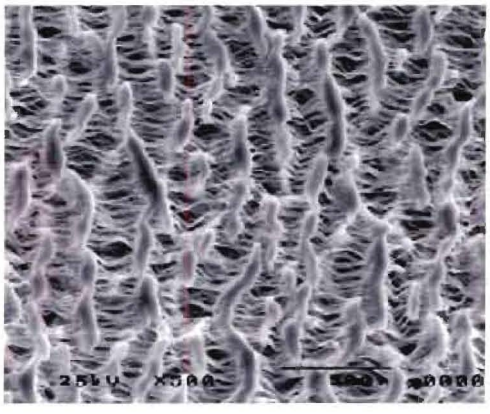

Figure 2-7: Electron microscope image of a section of an ePTFE graft [36].

While Dacron grafts are favoured for use as large diameter grafts, where they have a 93% patency rate at 10 years, ePTFE grafts are favoured for medium sized grafts and have a patency of 40-50% at 4 years [36, 43, 62]. In small diameter cases however both of these grafts fail rapidly due to occlusion caused by thrombosis and IH [23, 36, 37, 43, 52, 61, 62]. IH occurs mainly at the anastomosis of synthetic grafts [38, 43, 48]. This is where the artery, to which the synthetic graft is sutured, will be damaged initiating the IH [43]. Both Dacron and ePTFE are also inherently thrombogenic and once implanted require continual washing of the surface with high blood flow. If low flow velocity is the experienced, reducing shear stress, intimal thickening will also be seen in synthetic grafts. It is interesting to note that more IH will occur in prosthetic conduits than autologous grafts, with the same haemodynamic variation [23, 37, 38]. Other mechanical and non-mechanical factors causing IH have already been discussed.

Polyurethane (PU) grafts have been created which mimic arterial compliance, but they have not progressed past clinical trials. PU grafts (shown in *Figure 2-8*) show good biocompatibility, deformational and strength properties, but are susceptible to degradation over long implantation periods. The mechanical properties can be varied by varying the porosity of the material. When PU grafts were implanted into the canine model, more compliance loss over time occurred for compliance-matched grafts compared to the non-compliance-matched grafts. This could be due to the increased porosity needed to create the matched grafts, as the increased porosity can lead to augmented ingrowth and therefore greater compliance change. A negative point to PU grafts is that they have been associated with thrombosis and embolism formation after implantation [23, 36, 42, 43, 46, 61, 62].

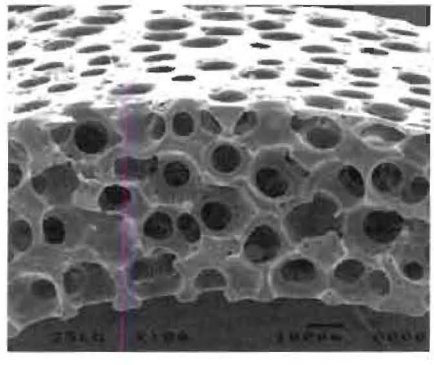

Figure 2-8: Electron microscope image of a section of porous polyurethane graft [36].

Autologous grafts undergo some chronic physiological changes (like wall thickening) after implantation, but this does not cause any change in their compliance. For prosthetic grafts this is however not the case. The surrounding tissues cause prosthetic grafts to lose compliance over time. This is especially true for porous structures where considerable fibrous tissue ingrowth takes place [37, 44-46].

2.3.3 Towards the Ideal Vascular Graft

The ideal graft has been described to have the following properties [43, 46, 68, 69]:

- Resistance to infection
- Biocompatibility
- Non-thrombogenicity, even in low flow states.
- Generation of optimum tissue reaction: allowing healing while preventing fibrous capsule formation
- Facilitate ease of suturing and allow minimal size of needle holes and bleeding following implantation. It must allow sutures to hold when under longitudal and circumferential tension and retain axial and radial compliance and pulsatility
- Durability
- Resistance to degradation
- Flexibility
- Compliance
- Similar viscoelastic properties to the artery it is replacing
- Availability in a wide range of sizes
- Manufactured cheaply in a relatively short space of time.

Unfortunately no ideal graft has been developed to date and work is being done to create a graft with the best possible properties. Native veins and arteries remain the reference material for medium and small diameter arteries as they function the best of all grafts under these conditions [58, 62]. Work continues in order to obtain the ideal graft and different avenues have been explored.

Using vein cuffs make the compliance and size mismatch more gradual leads to improved patency by redistributing the IH away from the anastomosis, even though the overall extent of the IH remains the same [44].

Mechanical suitability alone does not guarantee the success of a graft [36, 70]. Grafts also need to be non-thrombogenic and burst resistant [71]. In this respect, surface modification of existing grafts or the incorporation of autologous vessel cells into the synthetic grafts have been suggested [37, 62]. Increasing porosity of synthetic grafts leads to increased healing by the formation of an endothelial layer in the lumen [72]. In ePTFE grafts the porosity can be increased and used advantageously to promote ingrowth stimulating the formation of an endothelial layer. The increased porosity unfortunately also increased the adherence of other materials to the graft that could be damaging [43]. There does however exist a need for vascular grafts to have the same mechanical properties as that of the native artery which they need to replace [46, 62, 71].

Attention should be given to designing more compliant grafts. This could be done by increasing porosity or possibly using double tubular grafts consisting of more compliant inner linings with less compliant outer linings [44]. Many such composite grafts have undergone some degree of testing, but have not yet passed clinical trials. Tests have been conducted on PU grafts with polycarbonate urethane inner mesh and an outer layer consisting of meshed Dacron, sealed to prevent leakage. These composite grafts showed improved patency as well as decreased stenosis and intimal thickening compared to ePTFE grafts when tested in the canine model [62]. Another graft tested in the canine model constituted a woven graft of pre-stretched PU monofilament yarn and polyester multifilament yarn. These showed the development of a stable neointima within 6 months. PU grafts reinforced with knitted polyester also showed several advantageous over ePTFE when tested in 52 patients, however the cumulative patency rate was still inferior to ePTFE grafts [62]. Applying external support to synthetic grafts leads to a decrease in intimal thickening. PU grafts which are very porous can be unstable and it appears that by adding an external wrap around the graft shields it partially from the degradation while still allowing healing though ingrowth.

Composite grafts containing saphenous vein have also been researched extensively. It has been suggested that the patency of Saphenous vein bypass grafts might be improved in future if the wall properties can be manipulated to approach that of a artery [53]. Composite grafts consisting of vein grafts wrapped in tightly fitting Dacron mesh (diameter downsizing about 10 %) were tested in the canine model. In this case the myointimal wall thickening was decreased compared to both normal vein graft controls and vein grafts with loosely fitting Dacron wrap [31]. New Zealand white rabbits tight

and loosely fitting ePTFE wraps and wall thickening was seen to be greater in the loosely wrapped grafts than in the tightly wrapped ones [34]. Rat vein grafts were also wrapped in polyester stents, reducing the formation of IH [73]. In the porcine model, vein grafts supported by external polyester stents also showed less IH than control grafts even at one month. At six months the luminal area of the wrapped grafts was even greater than at one month. A decrease in medial as well as intimal thickening was reported Space between the stent and the vein graft was initially occupied by thrombus, which over time reorganized to form a neo-adventitia. A loose fitting porous Dacron mesh also improved the overall thickening by decreased SMC proliferation. A tightly fitting PTFE stent however still decreased medial thickening, but increased IH. The porosity of the external stent is closely related to its healing abilities, in particular the formation of the neo-intima [39, 64, 66]. Vein grafts supported by a Dacron mesh were implanted in sheep and this caused severely decreased intimal thickening compared to unsupported grafts [52]. Ten patients who received vein grafts wrapped in Gore-Tex ring enforced vascular grafts and showed good patency after long term follow up [73]. Saphenous vein grafts inserted into a 8 mm diameter ePTFE wrap of external bead support type was shown to have reduced compressions and kinks [74]. By applying a tight ePTFE wrap to a vein graft in order to decrease the diameter, a decrease in IH was shown, while a loose wrap did not have any positive effect [35]. Dashwood et al (2002) showed that externally stenting vein grafts with a polyester stent affected the nerve distribution. The formation of paravascular nerve bundles is significantly reduced, while nerve distribution on the medial/adventitial border is unaffected. The formation of a neointima was also reduced in the stented grafts and it is therefore postulated that the presence of paravascular nerves could influence graft thickening. The formation of a dense and organized neo-adventitia is though to block to formation of the nerves to some extent [59].

External support of vein grafts prevents over dilation beyond the artery size, decreasing disrupted flow patterns and de-endothelialisation. Vessel wall thickening appears to be a response to normalize changed wall mechanics experienced in the arterial circulation by decreasing tangential wall stress and increasing wall shear stress. External stenting decreases this thickening by performing this function [52-54, 64].

From these experiments it can be deduced that increasing wall shear stress contributes to decreasing the wall thickening. The observed reduction in wall thickening can thus be due to the reduction of graft distention by the restrictive external supports and/or due in

to increased blood velocity (determinant of shear stress). Both of these mechanical factors have been implicated in reduction of wall thickening and IH in both bioprosthetic and synthetic graphs. However wall shear stress has been shown to play less of a role in wall thickening than the decrease of circumferential wall tension. [31, 49, 63, 72, 73]. It appears that tight fitting non-porous external stents do not show the same improvements in graft patency as porous non-restrictive external wraps. This has been postulated to be due to the more effective adventitial macro vascular network which develops in porous and oversized grafts.[39, 53, 64, 66]. Problems associated with external support generally relate to stent size and material used, as well as the application of the external support [53, 73]. An external support in the form of a perivenous fibrin glue spray has been proposed. This allows the vein to preserve some pulsatility while overdistention is prevented [53].

Some of the mechanical factors implicated in IH can also be altered by varying the anastomotic geometries. This has been investigated through computer modeling [48].

2.4 Shape Memory Alloys

The structure examined in this work consists of a material type called a Shape Memory Alloy (SMA). A number of different SMAs exist e.g.: Ag-Cd, Au-Cd, Cu-Zn-Al, Cu-Al-Ni, Ni-Al, Fe-Pt, Mn-Cu and Ni-Ti [75-77]. The attribute that separates SMAs from other metals and metallic alloys is that they can exist in two solid phases, whose crystal structures depend on temperature and their state of stress. At high temperatures the SMA exists in the austenite phase and at lower temperatures it is in the martensite phase. The two properties for which SMA's are best known are: the Shape Memory Effect and Superelasticity. Superelasticity occurs at sufficiently high temperatures and is the recovery of large strains through a loading-unloading curve. The shape memory effect describes the recovery of large strains by a combination of mechanical and thermal effects [77-80].

Of all the SMAs Nitinol (Ni-Ti alloy) is probably the most used in the medical field due to its high degree of biocompatibility. It is also strong, sufficiently non-reactive, does not fatigue as easily as other metals and is non-magnetic (ensuring Magnetic Resonance Imaging will still be possible) [9, 78, 81, 82]. Another feature that makes Nitinol suitable

for biological applications is that the temperature range in which it is superelastic includes the temperature of the human body [83].

The martensite phase will start to transform into the austenite phase upon heating. In the stress-free state, the temperature at which this transformation initiates is called the austenite start temperature (A_S), while the temperature at which it ends is called the austenite finish temperature (A_f). Similarly, cooling Nitinol from the austenite phase will result in a phase transformation back to the martensite phase. This transformation begins at the martensite start temperature (M_S) and ends at the martensite finish temperature (M_f). *Figure 2-9* illustrates how the percentage of austenite phase present in a sample changes with a change in the temperature. The composition and stress state of the alloy influences the characteristic temperatures at which these transformations occur. The difference between the characteristic transition temperatures for heating and cooling is called the hysteresis. For Nitinol this is usually around 20-50 °C [78-80].

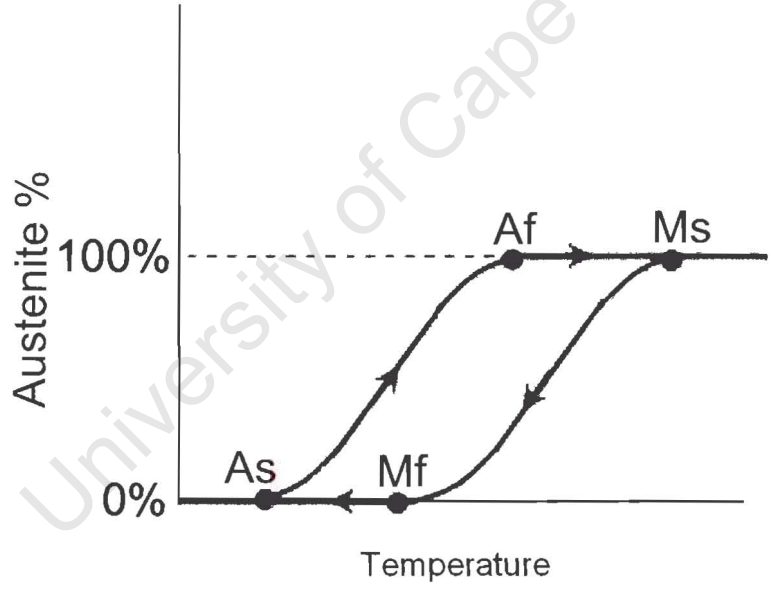

Figure 2-9: The percentage austenite phase present in the alloy during the heating and cooling of an SMA.

The two different solid phases have different crystal structures. The austenite phase has a body-centred cubic (bcc) crystal structure, while the martensite phase has a monoclinic crystal structure. This crystal structure can exist in multi-variant or single variant phase [76, 77, 83]. Due to their distinct crystal structures, a difference can be observed in the physical properties of the martensite and austenite phases. In the martensite phase the

alloy is softer and more ductile, whereas it is strong and hard when it is in the austenite phase [78]. The multi-variant martensite phase is shown in *Figure 2-10*.

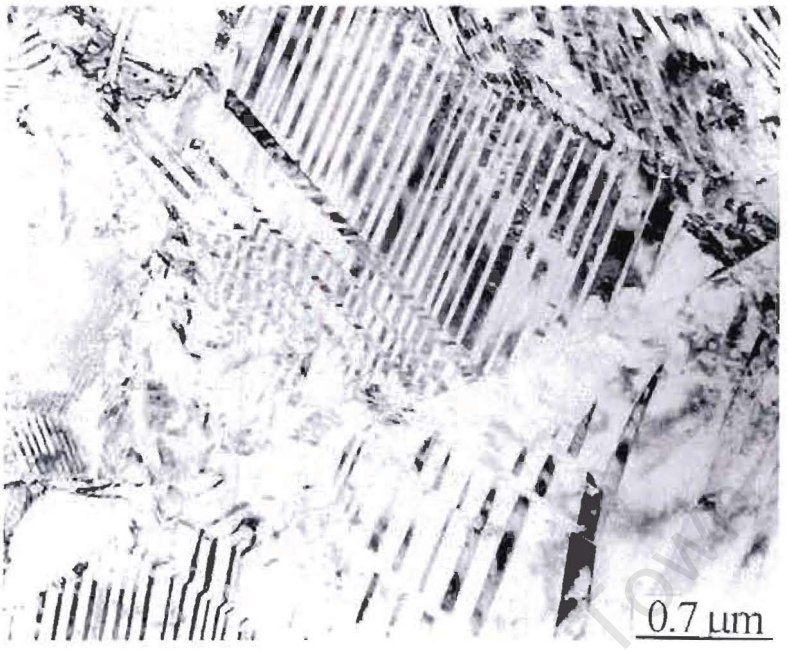

Figure 2-10: Multi-variant martensite crystals [84].

When the metal is the austenite phase (i.e. above the temperature A_f) it can transform to the martensite phase in two different ways. If it is cooled the bcc crystals will start to form multi-variant monoclinic crystals, representing the martensite phase. Otherwise, if stress is applies to it, the bcc crystals will start to transform to single variant monoclinic crystals, lying in the direction most preferential to the applied stress. This is called the stress induced martensite phase (SIM).

This property is based on the fact that the martensite phase can form at temperatures higher that M_S if it is in a state of stress. There is, however, a maximum temperature (labelled M_d) above which the austenite phase cannot form SIM.

If multi-variant martensite is places under stress, the crystals will re-orient themselves in the direction most preferential to the applied stress in a process termed martensite re-orientation. This processes and the formation of SIM have equal maximum theoretical recoverable inelastic strain, as both end in the single-variant martensite state [81]. The orientation will be such that it produces the maximum strain with respect to the applied stress [78]. Applying further stress to single variant martensite will lead to distortion of its lattice causing unrecoverable strain [77].

The two most well-known responses of SMA's can be explained as follows:

1) The Shape Memory Effect is a temperature induced response. When Nitinol is cooled from the austenite phase to the martensite phase; the alloy will retain its shape. It can easily be inelastically deformed in the martensite phase (by undergoing martensite re-orientation at a crystallographic level). Subsequent heating to above the A_f temperature results in the resumption of the original shape and rigidity by the formation bcc crystals of the austenite phase. This process is known as the one-way Shape Memory Effect [78].

The two-way Shape Memory Effect occurs when the alloy recovers a preset shape upon heating it above A_f, but also returns to a specified but different shape when cooled below M_f [78].

2) Superelasticity (also called pseudoelasticity) is a stress induced phase transformation. Superelasticity refers to Nitinol's property which allows it to return to its original shape after substantial deformation. This can only occur when the alloy is in the austenite phase and occurs due to single variant SIM [81]. The stress-strain relationship that occurs during the superelastic effect is illustrated in *Figure 2-11*. While this mechanism is recoverable upon unloading, the addition of more stress again leads to unrecoverable strain due to lattice distortion [77]. Superelasticity can only occur at temperatures from A_f up to M_d [78].

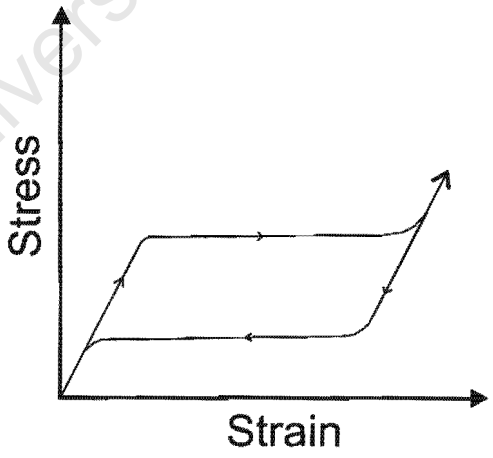

Figure 2-11: Stress-strain graph of Nitinol illustrating the superelastic effect.

The mechanisms and transformations do not always occur in such a structured fashion. Sometimes SIM does not form completely and as little as 70 % of the material can become martensitic even after full transformation. One of the reasons for this anomaly is impurities trapped in the alloy, which cause some plates to become locked in and unable

to transform further [75]. Another interesting phenomenon is that the end of the stress plateaus, which can be see in *Figure 2-11*, does not necessarily mark the end of the phase transformation. It only needs to mark the end of the strain localization [81]. All of this should be taken into account to fully explain the behaviour observed in experimental testing [81].

2.5 Continuum Mechanics

2.5.1 Kinematics

The information in the following three sub-sections was summarised from [85, 86]. Continuum mechanics is the study of mathematical models describing the behaviour of continuous media such as fluids and solids. Properties are assumed to vary smoothly with position and time ($\mathbf{X}$ and t). Continuum mechanics studies the response of materials to different loading conditions and consists of two main areas: (1) principles common to any medium and (2) constitutive models describing the behaviour of particular materials. In this section only the common principles will be dealt with. The constitutive equations will be described in Section 2.5.4.

When a continuum is deformed, a particle that was originally at position $\mathbf{X} = (X_1, X_2, X_3)$ at time t_0 will be at a position $\mathbf{x} = (x_1, x_2, x_3)$ at time t. This is illustrated in *Figure 2-12*.

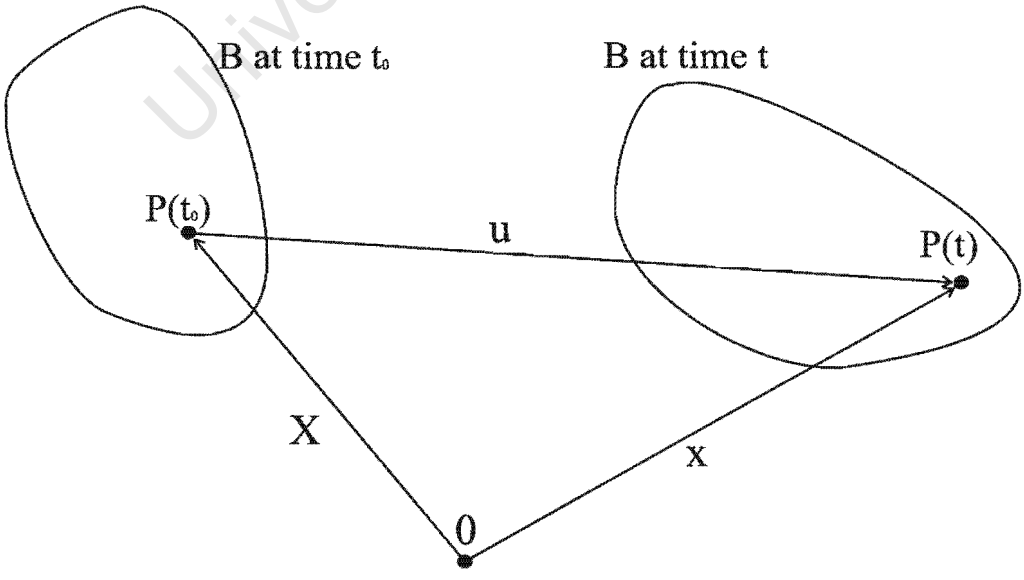

Figure 2-12: The deformation of a body B.

That is, the motion is described by $\mathbf{x} = \hat{\mathbf{x}}(\mathbf{X}, t)$. This function is invertible and therefore governing equations can be described in two different ways, the Lagrangian description or the Eulerian description. In the Lagrangian (Material or Reference) description the function is described in terms of the reference coordinates $\mathbf{X}$ and time t. In the Eulerian (Spatial) description the function is described in terms of the spatial coordinates $\mathbf{x} = (x_1, x_2, x_3)$ and time t.

The time rate of change of any function Θ is defined by the material derivative and is associated with a distinct material point $\mathbf{X}$. If the function uses the Lagrangian description its material derivative is defined as

$$\frac{D\Theta}{Dt} = \left(\frac{\partial \Theta}{\partial t}\right)_{X_i - fixed}. \tag{2.4}$$

If the Eulerian description is used to define $\Theta(\mathbf{x}, t)$, the material derivative of $\Theta(\mathbf{x}, t)$ is

$$\frac{D\Theta}{Dt} = \frac{\partial \Theta}{\partial x_i}\frac{\partial x_i}{\partial t} + \left(\frac{\partial \Theta}{\partial t}\right)_{X_i - fixed} = v \cdot \nabla \Theta + \frac{\partial \Theta}{\partial t}. \tag{2.5}$$

The material derivative of motion is the velocity and of velocity ($\mathbf{v}$) is the acceleration ($\mathbf{a}$). We therefore define

$$\mathbf{v} = \frac{D\mathbf{x}}{Dt} \tag{2.6}$$

$$\mathbf{a} = \frac{D\mathbf{v}(\mathbf{X}, t)}{Dt} = \frac{\partial \mathbf{v}(\mathbf{X}, t)}{\partial t} \text{ OR } \mathbf{a} = \frac{D\mathbf{v}(\mathbf{x}, t)}{Dt} = \frac{\partial \mathbf{v}}{\partial t} + (\nabla \mathbf{v})\mathbf{v}. \tag{2.7}$$

The displacement field is defined by

$$\mathbf{u} = \mathbf{x}(\mathbf{X}, t) - \mathbf{X}, \tag{2.8}$$

so that

$$\mathbf{x}(\mathbf{X}, t) = \mathbf{X} + \mathbf{u}(\mathbf{X}, t). \tag{2.9}$$

Deformation of a neighbouring element to $\mathbf{x}$ will then be

$$\mathbf{x} + d\mathbf{x} = \mathbf{X} + d\mathbf{X} + \mathbf{u}(\mathbf{X} + d\mathbf{X}, t). \tag{2.10}$$

To determine the deformation of the body the changes in the distances between the neighbouring points must be analysed. This can be done by subtracting equation (2.10) from equation (2.9) to obtain

$$\begin{aligned} d\mathbf{x} &= d\mathbf{X} + \mathbf{u}(\mathbf{X} + d\mathbf{X}, t) - \mathbf{u}(\mathbf{X}, t) \\ d\mathbf{x} &= d\mathbf{X} + (\nabla \mathbf{u}) d\mathbf{X} \end{aligned} \tag{2.11}$$

where $\nabla \mathbf{u}$ is the displacement gradient with components $\partial u_i / \partial X_j$; that is

$$[\nabla \mathbf{u}] = \begin{bmatrix} \frac{\partial u_1}{\partial X_1} & \frac{\partial u_1}{\partial X_2} & \frac{\partial u_1}{\partial X_3} \\ \frac{\partial u_2}{\partial X_1} & \frac{\partial u_2}{\partial X_2} & \frac{\partial u_2}{\partial X_3} \\ \frac{\partial u_3}{\partial X_1} & \frac{\partial u_3}{\partial X_2} & \frac{\partial u_3}{\partial X_3} \end{bmatrix}. \tag{2.12}$$

Equation (2.11) can be simplified by writing

$$d\mathbf{x} = \mathbf{F} d\mathbf{X} \tag{2.13}$$

where $\mathbf{F}$ is the deformation gradient, defined by $\mathbf{F} = \nabla \mathbf{x} = \mathbf{I} + \nabla \mathbf{u}$. The square of the distance between the particles is defined by

$$(ds)^2 = d\mathbf{X} \cdot \mathbf{F}^T \mathbf{F} d\mathbf{X}. \tag{2.14}$$

For small displacements $\mathbf{F}^T \mathbf{F} \approx \mathbf{I} + 2\mathbf{E}$ where $\mathbf{E}$ is the infinitesimal strain tensor defined by

$$\mathbf{E} = \tfrac{1}{2}[(\nabla \mathbf{u})^T + \nabla \mathbf{u}] = sym(\nabla \mathbf{u}). \tag{2.15}$$

Considering a material element $\mathbf{dX} = dS\mathbf{n}$ the difference between the square of the deformed length ds and the original length dS is given by

$$(ds)^2 - (dS)^2 = 2(dS)^2 \mathbf{n} \cdot \mathbf{E}\mathbf{n}. \tag{2.16}$$

In the case of small deformations this difference can also be written as

$$(ds) - (dS) = (ds + dS)(ds - dS) \approx 2dS(ds - dS). \tag{2.17}$$

From equations (2.16) and (2.17) the unit elongation in direction $\mathbf{n}$ is defined approximately by

$$\frac{ds - dS}{dS} = \mathbf{n} \cdot \mathbf{E}\mathbf{n} . \tag{2.18}$$

Let $d\mathbf{X}_m = dS_1\mathbf{m}$ and $d\mathbf{X}_n = dS_2\mathbf{n}$ with $\mathbf{m}$ and $\mathbf{n}$ are orthogonal unit vectors. Then

$$(ds_1)(ds_2)\cos\theta = 2(dS_1)(dS_2)\mathbf{m} \cdot \mathbf{E}\mathbf{n} \tag{2.19}$$

where θ is the angle between $d\mathbf{x}_1$ and $d\mathbf{x}_2$. If we let $\theta = \frac{\pi}{2} - \gamma$ then γ measures the small decrease in angle between the undeformed elements to the angle between the deformed elements. Since $\cos(\frac{\pi}{2} - \gamma) = \sin\gamma$ and for small strain $\sin\gamma = \gamma, \frac{ds_1}{dS_1} \approx 1, \frac{ds_2}{dS_2} \approx 1$ the change in angle is defined by

$$\gamma = 2\mathbf{m} \cdot \mathbf{E}\mathbf{n} . \tag{2.20}$$

The eigenvalues of the strain tensor are called the principal strains. Each principal strain acts in the direction of its eigenvector (or principal direction). The principal strains λ_i and respective principal directions $\mathbf{n}_i$ are thus defined by

$$\mathbf{E}\mathbf{n}_i = \lambda_i \mathbf{n}_i . \tag{2.21}$$

The strain tensor has three real eigenvalues corresponding to 3 orthogonal eigenvectors.

The material rate of change of $d\mathbf{x}$, a material element, is defined by

$$\left(\frac{D}{Dt}\right)\mathbf{x} = \nabla\mathbf{v}d\mathbf{x} \tag{2.22}$$

where $(\nabla\mathbf{v})_{ij} = \frac{\partial v_i}{\partial x_j}$ is the velocity gradient which can also written as

$$\nabla \mathbf{v} = \begin{bmatrix} \frac{\partial v_1}{\partial x_1} & \frac{\partial v_1}{\partial x_2} & \frac{\partial v_1}{\partial v_3} \\ \frac{\partial v_2}{\partial x_1} & \frac{\partial v_2}{\partial x_2} & \frac{\partial v_2}{\partial x_3} \\ \frac{\partial v_3}{\partial x_1} & \frac{\partial v_3}{\partial x_2} & \frac{\partial v_3}{\partial x_3} \end{bmatrix} = \mathbf{D} + \mathbf{W}. \tag{2.23}$$

In equation (2.23) $\mathbf{D} = symm(\nabla \mathbf{v})$ is the rate of deformation tensor and $\mathbf{W} = skw(\nabla \mathbf{v})$ is the spin tensor. From equation (2.23),

$$d\mathbf{x} \cdot \frac{D}{Dt}(d\mathbf{x}) = d\mathbf{x} \cdot (\nabla \mathbf{v}) d\mathbf{x} = d\mathbf{x} \cdot \mathbf{D} d\mathbf{x} + d\mathbf{x} \cdot \mathbf{W} d\mathbf{x}, \tag{2.24}$$

but since $\mathbf{W}$ is anti-symmetric $d\mathbf{x} \cdot \mathbf{W} d\mathbf{x} = 0$ and equation (2.24) becomes

$$d\mathbf{x} \cdot \frac{D}{Dt} d\mathbf{x} = d\mathbf{x} \cdot \mathbf{D} d\mathbf{x}. \tag{2.25}$$

Taking the material derivative of $d\mathbf{x} \cdot d\mathbf{x} = (ds)^2$ gives

$$2d\mathbf{x} \cdot \frac{D}{Dt}(d\mathbf{x}) = 2ds \frac{D}{Dt}(ds). \tag{2.26}$$

Using equations (2.25) and (2.26) the rate of extension (stretching) in the direction $\mathbf{n}$ is defined by

$$\frac{1}{ds} \frac{D(ds)}{Dt} = \mathbf{n} \cdot \mathbf{D} \mathbf{n} = D_{nn}. \tag{2.27}$$

Similar to equation (2.20), $\mathbf{m} \cdot \mathbf{D} \mathbf{n}$ is the rate of decrease in angle between two elements $dS_1 \mathbf{m}$ and $dS_2 \mathbf{n}$. $\mathbf{W}$ defines the angular velocity $\boldsymbol{\omega}$ by $\mathbf{W}\mathbf{x} = \boldsymbol{\omega} \times \mathbf{x}$.

2.5.2 Balance Laws

Conservation of mass implies that

$$\frac{D}{Dt}(\rho dV) = 0 \tag{2.28}$$

where ρ is the material density and V is volume. Equation (2.28) can then be rewritten as

$$\frac{D\rho}{Dt} = \frac{\partial \rho}{\partial t} + \mathbf{v} \cdot \nabla \rho = 0 \tag{2.29}$$

Equation (2.29) is called the equation of conservation of mass or the continuity equation.

The surface traction at a point on the boundary of B in a continuum is defined by

$$\mathbf{t}_n = \lim_{\Delta A \to o} \frac{\Delta \mathbf{f}}{\Delta A} \tag{2.30}$$

where $\Delta \mathbf{f}$ is the force acting on surface area ΔA. Assume the vector $\mathbf{n}$ is normal to the boundary then surface traction is given by

$$\mathbf{t}_n = \boldsymbol{\sigma}\mathbf{n} \tag{2.31}$$

where $\boldsymbol{\sigma}$ is the Cauchy stress tensor. The balance of momentum requires that the rate of change of linear momentum must equal the total force. This leads to Cauchy's equations of motion

$$div\boldsymbol{\sigma} + \rho \mathbf{f}^{\mathbf{B}} = \rho \mathbf{a} \tag{2.32}$$

where $\mathbf{f}^{\mathbf{B}}$ is the body force acting on the body and $(div\boldsymbol{\sigma})_i = \frac{\partial \sigma_{ij}}{\partial x_j}$.

When a body is at equilibrium with the forces acting on it no acceleration will be experienced. Equation (2.32) then becomes

$$div\boldsymbol{\sigma} + \rho \mathbf{f}^{\mathbf{B}} = 0 \tag{2.33}$$

and is known as the equations of equilibrium.

2.5.3 Boundary Conditions

In addition to the equations of motion, boundary conditions are also needed to define a problem. Consider a body B with boundary $\partial B = \partial B_u \cup \partial B_t \cup \partial B_c$ such that $\partial B_u \cap \partial B_t \cap \partial B_c = \varnothing$ (*Figure 2-13*). We consider 3 types of boundary conditions.

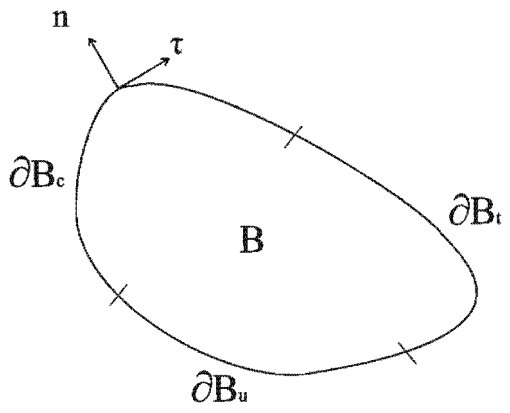

Figure 2-13: Domains of different boundary conditions on B.

(1) Displacements can be defined on one or more regions of the boundary, i.e.

$$\mathbf{u} = \mathbf{u}_0 \text{ on } \partial B_u . \tag{2.34}$$

(2) Surface tractions can be defined on one or more regions of the boundary, i.e.

$$\mathbf{t} = \mathbf{t}_0 \text{ on } \partial B_t . \tag{2.35}$$

(3) Contact can be defined on one or more regions of the boundary. In the problems considered in this work friction is zero while normal contact pressure uses the softened contact formulations. Let d be the distance between two contact surfaces and P the pressure they exert on each other. In hard contact formulation the surfaces will exert zero pressure while $d > 0$ and non-zero pressure when $d = 0$. In softened contact however, there exists some value d_0 on d from where pressure starts to increase according to some function. In the problems considered in this work, softened contact with an exponential curve is defined. For this definition a distance d_0 on the $d-axis$ and pressure value P_0 on the $P-axis$ must be given in order to define the distance-pressure curve shown in *Figure 2-14.*

The contact boundary condition on ∂B_c is therefore

$$\begin{aligned} &\mathbf{t}\cdot\boldsymbol{\tau} = 0 && \forall d && \text{on } \partial B_c \\ &\mathbf{t}\cdot\mathbf{n} = 0 && \forall d > d_0 && \text{on } \partial B_c \\ &\mathbf{t}\cdot\mathbf{n} = \frac{P_0}{e-1}\left(1+\frac{d}{d_0}\right)\left(e^{1+\frac{d}{d_0}}-1\right) && \forall d \le d_0 && \text{on } \partial B_c \end{aligned} \tag{2.36}$$

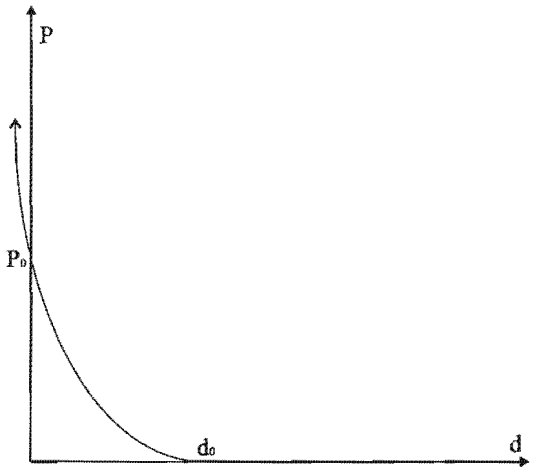

Figure 2-14: Softened contact pressure curve.

Summary

The governing equations of this problem are as follows:

$$div\boldsymbol{\sigma} + \rho \mathbf{f}^{\mathbf{B}} = 0 \tag{2.33}$$

$$\boldsymbol{\sigma} = f(\mathbf{E}) \tag{2.37}$$

With boundary conditions:

$$\mathbf{u} = \mathbf{u}_0 \text{ on } \partial B_u \tag{2.34}$$

$$\mathbf{t} = \mathbf{t}_0 \text{ on } \partial B_t \tag{2.35}$$

$$\begin{aligned} &\mathbf{t}\cdot\boldsymbol{\tau} = 0 && \forall d && on \quad \partial B_c \\ &\mathbf{t}\cdot\mathbf{n} = 0 && \forall d > d_0 && on \quad \partial B_c \\ &\mathbf{t}\cdot\mathbf{n} = \frac{p_0}{e-1}\left(1+\frac{d}{d_0}\right)\left(e^{1+\frac{d}{d_0}}-1\right) && \forall d \le d_0 && on \quad \partial B_c \end{aligned} \tag{2.36}$$

To define the relation between the stress and strain distributions in equation (2.37), constitutive equations for the specific material under consideration is needed. In the next section the constitutive theory is discussed for the material model which will be used in this work.

2.5.4 Shape Memory Alloy Constitutive Theory

The constitutive equations used in ABAQUS CAE 6.4-5 (Abaqus Inc., Providence, RI, USA) to define superelastic material behaviour are based on the following theory [79, 80, 87].

In this constitutive model, the material is assumed to be isotropic. Three transformation processes are considered:

- Conversion from austenite to single-variant martensite phase (A => S).
- Conversion from single-variant martensite to austenite phase (S => A).
- Single variant martensite reorientation.

The one-dimensional transformation processes is illustrated by *Figure 2-15*. The loading function can be defined as

$$F = \sigma - CT \tag{2.38}$$

Where σ is applied stress, C is a material parameter and T is the temperature of the system. For the A => S transformation $\dot{F} > 0$ while for the S => A transformation $\dot{F} < 0$.

The A => S transformation starts when the increasing loading function crosses the line

$$F_S^{AS} = \sigma - C(T - M_S) = 0 \tag{2.39}$$

where M_S is a material parameter. At this point the martensite fraction (ξ_s) present in the material is equal to zero as the material still consists entirely of austenite phase material. This transformation is completed when the increasing loading function crosses the line

$$F_f^{AS} = \sigma - C(T - M_f) = 0 \tag{2.40}$$

where M_f is a material parameter. At this point $\xi_s = 1$ and the material has been completely transformed into the single-variant martensite phase.

The S => A transformation starts when the decreasing loading function crosses the line

$$F_S^{SA} = \sigma - C(T - A_S) = 0 \tag{2.41}$$

where A_S is a material parameter. At the point where the two lines cross $\xi_s = 1$, as the material is entirely in the martensite phase. The transformation to the austenite phase is completed when the decreasing loading function crosses the line

$$F_f^{SA} = \sigma - C(T - A_f) = 0 \tag{2.42}$$

where A_f is another material parameter. As the transformation is then completed, $\xi_s = 0$.

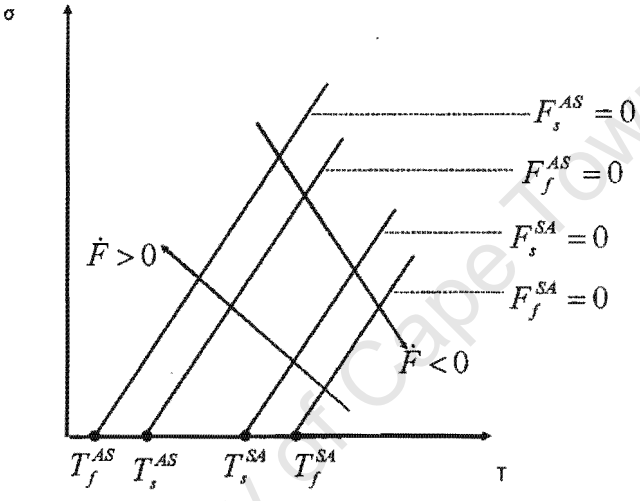

Figure 2-15: One dimensional transformation processes.

Next the three dimensional model is considered. The total strain experienced by the material is given by the equation

$$\boldsymbol{\varepsilon} = \boldsymbol{\varepsilon}^e + \boldsymbol{\varepsilon}^{tr} \tag{2.43}$$

where $\boldsymbol{\varepsilon}^e$ is the elastic strain and $\boldsymbol{\varepsilon}^{tr}$ is the transformation strain and

$$\boldsymbol{\varepsilon}^{tr} = \varepsilon_L \boldsymbol{\varepsilon}' \tag{2.44}$$

where ε_L is a scalar parameter representing the maximum deformation obtainable by only the detwinning of the single variant martensite and $\boldsymbol{\varepsilon}'$ is the scaled transformation strain.

During each of the 3 transformation processes listed earlier, changes in $\boldsymbol{\varepsilon}'$ and ξ_s occur. To define the constitutive relation for the material it is necessary to analyse

$$\dot{\boldsymbol{\varepsilon}}^{t} = \dot{\boldsymbol{\varepsilon}}^{tAS} + \dot{\boldsymbol{\varepsilon}}^{tSA} + \dot{\boldsymbol{\varepsilon}}^{tSS}$$
$$\dot{\xi}_S = \dot{\xi}_S^{AS} + \dot{\xi}_S^{SA} \tag{2.45}$$

Note that during the martensite reorientation phase the fraction of martensite present in the material does not change. $\therefore \dot{\xi}_S^{SS} = 0$.

Austenite to Single-Variant Martensite Transformation

A Drucker-Prager-type loading function is employed as a function of stress ($\boldsymbol{\sigma}$) and temperature (T)

$$F^{AS}(\boldsymbol{\sigma}, T) = \|\boldsymbol{t}\| + 3\eta P + C^{AS}T \tag{2.46}$$

where $\boldsymbol{t}$ is the deviatoric stress tensor ($\boldsymbol{t} = \boldsymbol{\sigma} - \frac{tr(\boldsymbol{\sigma})}{3}\boldsymbol{I}$) and P is the pressure. C^{AS} and η are material parameters and $\|\cdot\|$ indicates the euclidean norm.

The initial and final transformation functions also differ from that of the one dimensional model and are given by

$$F_S^{AS} = F^{AS} - R_S^{AS}$$
$$F_f^{AS} = F^{AS} - R_f^{AS} \tag{2.47}$$

where

$$R_S^{AS} = \sigma_S^{AS}\left(\sqrt{\frac{2}{3}} + \eta\right) - C^{AS}M_S$$
$$R_f^{AS} = \sigma_f^{AS}\left(\sqrt{\frac{2}{3}} + \eta\right) - C^{AS}M_f \tag{2.48}$$

with $\sigma_S^{AS}, \sigma_f^{AS}, M_S, M_f$ all material parameters.

The transformation can only take place as long as the following conditions (activation conditions) are satisfied: $F_S^{AS} > 0$; $F_f^{AS} < 0$; $\dot{F}^{AS} > 0$.

The scaled transformation strain is assumed to evolve as follows

$$\dot{\boldsymbol{\varepsilon}}^{tAS} = \dot{\xi}_S \boldsymbol{N}^{AS} \tag{2.49}$$

where $N^{AS} = \frac{\mathbf{L}^{AS}}{\|\mathbf{L}^{AS}\|}$; $\mathbf{L}^{AS} = \frac{\partial F^{AS}}{\partial \boldsymbol{\sigma}}$.

The single-variant martensite fraction in equation (2.49) evolves either as a linear or exponential form. The material model used in this work assumes the exponential form

$$\dot{\xi}_S^{AS} = H^{AS}\kappa^{AS}(1-\xi_S)\frac{\dot{F}^{AS}}{(F_f^{AS})^2} \tag{2.50}$$

Where κ^{AS} is a material parameter measuring the speed of transformation and H^{AS} embeds the activation conditions for the transformation.

$$H^{AS} = \begin{cases} 1 \; if \; F_S^{AS} > 0, F_f^{AS} < 0, \dot{F}^{AS} > 0 \\ 0 \; if \; Otherwise \end{cases} \tag{2.51}$$

Single variant martensite to austenite transformation

A Drucker-Prager-type function is again employed to define the loading function

$$F^{SA}(\boldsymbol{\sigma}, T) = \|\boldsymbol{t}\| + 3\eta P - C^{SA}T \tag{2.52}$$

Where C^{SA} is a material parameter and the other variables are defined as for equation (2.46).

The initial and final transformation functions are given by

$$\begin{aligned} F_S^{SA} &= F^{SA} - R_S^{SA} \\ F_f^{SA} &= F^{SA} - R_f^{SA} \end{aligned} \tag{2.53}$$

where

$$\begin{aligned} R_S^{SA} &= \sigma_S^{SA}\left(\sqrt{\frac{2}{3}} + \eta\right) - C^{SA}A_S \\ R_f^{SA} &= \sigma_f^{SA}\left(\sqrt{\frac{2}{3}} + \eta\right) - C^{SA}A_f \end{aligned} \tag{2.54}$$

with $\sigma_S^{SA}, \sigma_f^{SA}, A_S, A_f$ all material parameters.

The conditions for this transformation to take place are $F_S^{SA} > 0$; $F_f^{SA} < 0$; $\dot{F}^{SA} > 0$.

The scaled transformation strain is given by

$$\dot{\boldsymbol{\varepsilon}}'^{SA} = \dot{\xi}_S \boldsymbol{N}^{SA} \tag{2.55}$$

$$\text{where } \boldsymbol{N}^{SA} = \frac{\boldsymbol{\varepsilon}}{\|\boldsymbol{\varepsilon}\|} \tag{2.56}$$

The single variant martensite fraction again evolves as an exponential form such that

$$\dot{\xi}_S^{SA} = H^{SA} \kappa^{SA} (1 - \xi_S) \frac{\dot{F}^{SA}}{(F_f^{SA})^2} \tag{2.57}$$

with κ^{SA} a material parameter measuring the speed of transformation and H^{SA} embedding the activation conditions for the transformation.

$$H^{SA} = \begin{cases} 1 \; if \; F_S^{SA} < 0, F_f^{SA} > 0, \dot{F}^{SA} < 0 \\ 0 \; if \; Otherwise \end{cases} \tag{2.58}$$

Single-Variant Martensite Reorientation Process

The loading function and initial transformation function is given by

$$F^{SS}(\boldsymbol{\sigma}, T) = \|\boldsymbol{t}\| + 3\eta P - C^{SS} T \tag{2.59}$$

$$F_S^{SS} = F^{SS} - R_S^{SS} \tag{2.60}$$

where

$$R_S^{SS} = \sigma_S^{SS} \left(\sqrt{\frac{2}{3}} + \eta \right) - C^{SS} T_S^{SS} \tag{2.61}$$

with $\sigma_S^{SS}, T_S^{SS}, C_S^{SS}$ all material parameters.

The activation condition takes the form

$$F_S^{SS} > 0; \dot{\boldsymbol{N}}^{SS} \neq 0 \tag{2.62}$$

$$\text{where } \boldsymbol{N}^{SS} = \frac{\mathbf{L}^{SS}}{\|\mathbf{L}^{SS}\|}, \; \mathbf{L}^{SS} = \frac{\partial F^{SS}}{\partial \boldsymbol{\sigma}}. \tag{2.63),(2.64}$$

The scaled transformation strain corresponding to the single-variant martensite re-orientation transformation is

$$\dot{\boldsymbol{\varepsilon}}'^{SS} = H^{SS}\dot{\xi}_S \hat{\boldsymbol{N}}^{SS} \tag{2.65}$$

$$\text{where } H^{SS} = \begin{cases} 1 \; if \; F_S^{SS} > 0 \\ 0 \; if \; Otherwise \end{cases}. \tag{2.66}$$

Additional Considerations

In practice if the SMA material has enough energy to induce the phase transformation from austenite to single-variant martensite phase, it would also have enough energy to re-orient the fraction of material already transformed. $\therefore C^{AS} = C^{SS}$ and $R_S^{AS} = R_S^{SS}$ which leads to $F_S^{AS} = F_S^{SS}$. From the expressions of F^{AS} and F^{SS} it can be calculated that

$$\begin{aligned} \mathbf{L}^{AS} &= \mathbf{L}^{SS} = \frac{\boldsymbol{t}}{\|\boldsymbol{t}\|} + \eta \boldsymbol{I} = \mathbf{L} \\ \boldsymbol{N}^{AS} &= \boldsymbol{N}^{SS} = \frac{1}{1+3\eta}\left(\frac{\boldsymbol{t}}{\|\boldsymbol{t}\|} + \eta \boldsymbol{I}\right) = \boldsymbol{N} \end{aligned} \tag{2.67}$$

To obtain an expression for the scaled transformation strain, the rate equations from the previous sections must be integrated. Then

$$\boldsymbol{\varepsilon}' = \xi_S \hat{\boldsymbol{N}} \tag{2.68}$$

where $\hat{\boldsymbol{N}}$ is the current value of N while $H^{SS} = 1$, otherwise it is equal to the last value of N attained when $H^{SS} = 1$.

Model review

The scaled transformation strain $\boldsymbol{\varepsilon}'$ can be split into a deviatoric and volumetric part

$$\boldsymbol{\varepsilon}' = \boldsymbol{\varepsilon}_V' + \left(\frac{\varepsilon_d'}{3}\right)\boldsymbol{I} \tag{2.69}$$

w and $\boldsymbol{v}$ can be written as

$$\varepsilon_d' = 3\eta\xi_s = tr(\boldsymbol{\varepsilon}'); \; \boldsymbol{\varepsilon}_V' = \xi_s \hat{\boldsymbol{N}}_d \tag{2.70); (2.71}$$

where $\hat{N}_d$ is the deviatoric part of $\hat{N}$. The martensite fraction evolution is the only part of the model that still remains in rate form.

$$\dot{\xi}_S = \dot{\xi}_S^{AS} + \dot{\xi}_S^{SA} \tag{2.72}$$

$$\dot{\xi}_S^{SA} = H^{SA}\kappa^{SA}(1-\xi_S)\frac{\dot{F}^{SA}}{(F_f^{SA})^2} \tag{2.73}$$

$$\dot{\xi}_S^{AS} = H^{AS}\kappa^{AS}(1-\xi_S)\frac{\dot{F}^{AS}}{(F_f^{AS})^2} \tag{2.74}$$

where the variables have been define previously. The strain has previously been defined as

$$\boldsymbol{\varepsilon} = \boldsymbol{\varepsilon}^e + \boldsymbol{\varepsilon}^{tr} \tag{2.75}$$

$$\text{where } \boldsymbol{\varepsilon}^{tr} = \varepsilon_L \boldsymbol{\varepsilon}' \tag{2.76}$$

The free energy function (ψ) represents the portion of energy available for doing work at a constant temperature. Given that $\psi = \psi(\boldsymbol{\varepsilon}^e)$ a free energy function that is quadratic in the elastic strain is chosen

$$\psi = \frac{1}{2}\boldsymbol{\varepsilon}^e \boldsymbol{D}^e \boldsymbol{\varepsilon}^e \tag{2.77}$$

where $\boldsymbol{D}^e$ is a fourth-order elastic modulus tensor.

The stress distribution is then defined by

$$\boldsymbol{\sigma} = \frac{\partial \psi}{\partial \boldsymbol{\varepsilon}} = \boldsymbol{D}^e \boldsymbol{\varepsilon}^e = \boldsymbol{D}^e(\boldsymbol{\varepsilon} - \varepsilon_L \boldsymbol{\varepsilon}') \tag{2.78}$$

The elastic tensor $\boldsymbol{D}^e$ is assumed to be isotropic. The strain equations can then be split into volumetric and deviatoric parts as follows

$$\boldsymbol{\varepsilon} = \boldsymbol{\varepsilon}_V - \frac{\varepsilon_d}{3}\boldsymbol{I} \tag{2.79}$$

$$\boldsymbol{\varepsilon}_V = \boldsymbol{\varepsilon}_V{}^e + \varepsilon_L \xi_s \hat{N}_d \tag{2.80}$$

$$\varepsilon_d = \varepsilon_d^{\,e} + 3\eta\varepsilon_L\xi_S \tag{2.81}$$

$$\boldsymbol{\varepsilon}^e = \boldsymbol{\varepsilon}_V^{\,e} + \frac{\varepsilon_d^{\,e}}{3}\boldsymbol{I} \tag{2.82}$$

Also

$$p = K\theta^e = K(\theta - \varepsilon_L w) \tag{2.83}$$

$$\boldsymbol{t} = 2G\boldsymbol{e}^e = 2G(\boldsymbol{e} - \varepsilon_L \boldsymbol{v}) \tag{2.84}$$

2.6 Numerical modelling

2.6.1 Finite Element Method

The information in this section was summarised from [88, 89]. A direct solution method for solving the governing equations of the problem given in Section 2.5 is not always available; therefore an approximate solution method is required. Different approximate solution methods are available, but in the current work, FEM is used and will be described. In this method the body under consideration is subdivided (refer to *Figure 2-16*) and an approximate solution is constructed using simple functions (e.g. polynomials). In order to apply the approximation solutions, the problem needs to be stated in its weak form.

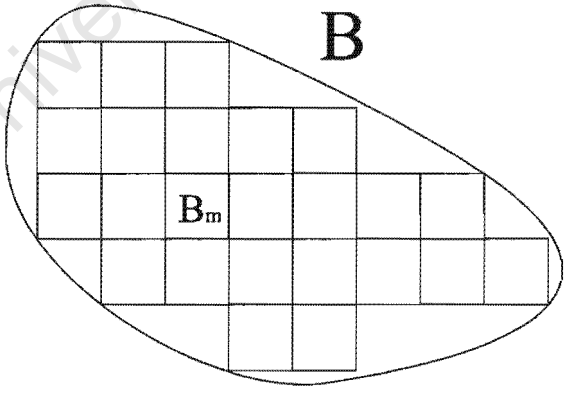

Figure 2-16: A continuum body B represented by elements B_m.

Principle of Virtual Work

Two function spaces must be defined in order to formulate the problem effectively. The space $L_2(B)$ of square-integrable functions is defined as

$$L_2(B) = \{u : \int_B u^2 dV < \infty\} \tag{2.85}$$

This space can be employed to define the Sobolev space $H^1(B)$ as

$$H^1(B) = \{u : u \in L_2(B), \frac{\partial u}{\partial x_i} \in L_2(R), i = 1,2,3\} \tag{2.86}$$

Both of these spaces are inner product spaces with their inner products and norms defined by

$$\begin{aligned} (u,w)_{L_2} &= \int_B uw dV \\ \|w\|_{L_2} &= \sqrt{(w,w)_{L_2}} \end{aligned} \tag{2.87}$$

for $L_2(B)$ and

$$\begin{aligned} (u,w)_{H^1} &= \int_B (uw + \nabla u \cdot \nabla w) dV \\ \|w\|_{H^1} &= \sqrt{(w,w)_{H^1}} \end{aligned} \tag{2.88}$$

for $H^1(B)$.

To formulate the weak form of the displacement problem, a set of actual displacements, $\mathbf{u}$, and a set of test functions $\mathbf{w}$ must be defined from the respective Sobolev spaces. These test functions are defined by the sets

$$\begin{aligned} V &= \{\mathbf{w} : w_i \in H^1(B), w_i|_{\partial B_U} = 0\} \\ U &= \{\mathbf{u} : u_i \in H^1(B), u_i|_{\partial B_U} = (u_0)_i\} \end{aligned} \tag{2.89}$$

where ∂B_U is the section of the boundary of B where the displacement conditions are applied. The only displacement boundary condition considered here is $u_i = 0$ and therefore the two sets are equivalent.

When Cauchy's equilibrium equation is multiplied through by $\mathbf{w} \in V$ and then integrated over the entire body it becomes

$$\int_B \mathbf{w} \cdot div\boldsymbol{\sigma} dV + \int_B \mathbf{w} \cdot \mathbf{f}^B dV = 0. \tag{2.90}$$

It can be shown that

$$div(\boldsymbol{\sigma}\mathbf{w}) = \boldsymbol{\sigma} \cdot \nabla \mathbf{w} + \mathbf{w} \cdot div\boldsymbol{\sigma}\,. \tag{2.91}$$

Substituting equation (2.91) into equation(2.90) we obtain

$$\int_B div(\boldsymbol{\sigma}\mathbf{w})dV - \int_B \boldsymbol{\sigma} \cdot \nabla \mathbf{w} dV = -\int_B \mathbf{w} \cdot \mathbf{f}^B dV\,. \tag{2.92}.$$

The divergence theorem gives

$$\int_B div(\boldsymbol{\sigma}\mathbf{w})dV = \oint_{\partial B} (\boldsymbol{\sigma}\mathbf{w}) \cdot \mathbf{n} dS = \int_{\partial B} \mathbf{t} \cdot \mathbf{w} dS \tag{2.93}$$

and since $\boldsymbol{\sigma}$ is symmetric, it can be shown that

$$\boldsymbol{\sigma} \cdot \nabla \mathbf{w} = \boldsymbol{\sigma} \cdot \boldsymbol{\varepsilon}(\mathbf{w})\,. \tag{2.94}.$$

Taking equation (2.92), (2.93) and (2.94) into account, the variational or weak form of the problem becomes:

Find $\mathbf{u} \in U$ (the actual displacement) such that for any $\mathbf{w} \in V$ (virtual displacement) the following equation holds:

$$\int_B \boldsymbol{\sigma}(\mathbf{u}) \cdot \boldsymbol{\varepsilon}(\mathbf{w}) dV = \int_{\partial B} \mathbf{t} \cdot \mathbf{w} dS + \int_B \mathbf{w} \cdot \mathbf{f}^B dV\,. \tag{2.95}.$$

Equation (2.95) is known as the principal of virtual work (or displacement) or simply as the virtual work statement. The stress distribution, $\boldsymbol{\sigma}(\mathbf{u})$, can be written in terms of strain through the constitutive theory described in the previous section. The strain can be defined in term of displacement, $\mathbf{u}$, using the infinitesimal strain tensor.

Galerkin Formulation

Since equation (2.95) cannot in general be solved analytically, an approximate displacement solution must be found. The Galerkin method can be used to construct an approximate solution to the virtual work statement by replacing V, an infinite dimensional space, by V^r, a finite-dimensional space, where

$$V^r \subset V$$

$$V^r = span\left\{\begin{matrix}\phi_i \\ \phi_i \\ \phi_i\end{matrix}\right\}_{i=1}^{r} \tag{2.96}$$

$$\text{where } V^r \to V \text{ as } r \to \infty$$

and $r = \dim(V^r)$. The larger the value of r the closer the approximate solution resembles the exact solution. The approximate solutions to the test functions $\mathbf{u}$ and $\mathbf{v}$ can be given in terms of the basis $\{\varphi_1 \quad \dots \quad \varphi_r\}$ as

$$\begin{aligned}\mathbf{u}^r &= \sum_{i=1}^{r} \boldsymbol{\alpha}_i \phi_i, \\ \mathbf{w}^r &= \sum_{i=1}^{r} \boldsymbol{\beta}_i \phi_i, \\ \mathbf{u}^r, \mathbf{w}^r &\in V^r,\end{aligned} \tag{2.97}$$

where

$$\boldsymbol{\beta} = \begin{pmatrix}\boldsymbol{\beta}_1 \\ \boldsymbol{\beta}_2 \\ \vdots \\ \boldsymbol{\beta}_r\end{pmatrix} \text{ and } \boldsymbol{\alpha} = \begin{pmatrix}\boldsymbol{\alpha}_1 \\ \boldsymbol{\alpha}_2 \\ \vdots \\ \boldsymbol{\alpha}_r\end{pmatrix}$$

Substituting equation (2.97) into equation (2.95) the approximate virtual work equation becomes

$$\int_B \boldsymbol{\sigma}(\mathbf{u}^r) \bullet \boldsymbol{\varepsilon}(\mathbf{w}^r) dV = \int_{\partial B} \mathbf{t} \bullet \mathbf{w}^r dS + \int_B \mathbf{w}^r \bullet \mathbf{f}^B dV \tag{2.98}$$

known as the Galerkin formulation.

Finite Element Method Formulation

From here of, Voigt notation will be used to describe the stress and strain tensors as follows:

$$\boldsymbol{\sigma} = \begin{pmatrix}\sigma_{11} & \sigma_{22} & \sigma_{33} & \sigma_{12} & \sigma_{13} & \sigma_{23}\end{pmatrix}^T \tag{2.99}$$

$$\text{and } \boldsymbol{\varepsilon} = \left(\varepsilon_{11} \quad \varepsilon_{22} \quad \varepsilon_{33} \quad 2\varepsilon_{12} \quad 2\varepsilon_{13} \quad 2\varepsilon_{23}\right)^T. \tag{2.100}$$

Since the strain is a function of displacement, using equation (2.97) it can be written as

$$\boldsymbol{\varepsilon}(\mathbf{w}^r) = \mathbf{B}\boldsymbol{\beta} \tag{2.101}$$

Equation (2.98) can then becomes

$$\int_B \boldsymbol{\beta}^T \mathbf{B}^T \boldsymbol{\sigma}(\boldsymbol{\alpha}) dV = \boldsymbol{\beta}^T \int_{\partial B} \mathbf{t} \bullet \boldsymbol{\varphi} dS + \boldsymbol{\beta}^T \int_B \mathbf{f}^B \bullet \boldsymbol{\varphi} dV \tag{2.102}$$

where

$$\boldsymbol{\varphi} = \begin{bmatrix} \phi_1 \\ \vdots \\ \phi_r \end{bmatrix}$$

Since $\boldsymbol{\beta}$ is arbitrary, equation (2.102) leads to

$$\int_B \mathbf{B}^T \boldsymbol{\sigma}(\boldsymbol{\alpha}) dV = \int_{\partial B} \mathbf{t} \bullet \boldsymbol{\varphi} dS + \int_B \mathbf{f}^B \bullet \boldsymbol{\varphi} dV, \tag{2.103}$$

which can also be written as

$$\mathbf{K}(\alpha) = \mathbf{F}. \tag{2.104}$$

$\mathbf{K}$ is the global stiffness matrix while $\mathbf{F}$ is the global loading vector defined by

$$\mathbf{K}(\boldsymbol{\alpha}) = \int_B \mathbf{B}^T \boldsymbol{\sigma}(\boldsymbol{\alpha}) dV \tag{2.105}$$

$$\mathbf{F} = \int_{\partial B} \mathbf{t} \bullet \boldsymbol{\varphi} dS + \int_B \mathbf{f}^B \bullet \boldsymbol{\varphi} dV \tag{2.106}$$

Element Definition

In FEM, the domain B is subdivided into distinct elements $B_1, \ldots, B_m, \ldots, B_e$. These elements obey the conditions

- $B_l \cap B_m = \varnothing$ if $l \neq m$,
- $\bigcup_{m=1}^{e} B_m = B$.

Equation (2.103) can then be written in term of the elements as

$$\sum_{m=1}^{e} \int_{B_m} \mathbf{B}^T \boldsymbol{\sigma}(\boldsymbol{\alpha}) dV = \sum_{m=1}^{e} \int_{\partial B_m} \mathbf{t} \bullet \boldsymbol{\varphi} dS + \sum_{m=1}^{e} \int_{B_m} \mathbf{f}^B \bullet \boldsymbol{\varphi} dV \qquad (2.107)$$

There are three conditions for the displacement function to converge to the exact solution as r increases.

- The displacement model must be continuous within the element and the displacements between adjacent elements must be compatible. The first part is accomplished by choosing continuous polynomials and the second part holds if the displacement of the element boundary depends only on the nodes that lie on it.
- The displacement models must include rigid body displacement of elements
- The displacement model must include constant strain states of the element

Isoparametric Element

To avoid having to compute an inverse matrix, $\mathbf{B}$ can be constructed directly with the use of interpolation (or shape) functions. These functions are most conveniently described in terms of the natural coordinate system used to define isoparametric elements.

A local coordinate system is one that is defined for one element only, while a global coordinate system is defined for the entire body. A natural coordinate system is a local coordinate system which permits the specification of a point in the element by a set of dimensionless numbers whose magnitudes never exceed unity. Expressing an element's nodal displacements in the natural coordinate system generalises and simplifies equation formulation and allows the numerical integration used to solve the virtual work equation to be carried out more easily. Each element expressed in the global coordinate system (the actual element) has a parent element in its local natural coordinate system associated with it. There exists an invertible mapping from the isoparametric element $\hat{B}_m$ to the actual element B_m

$$F : \hat{B} \rightarrow B$$
$$x = F(\hat{x}) \tag{2.108}$$

The linear quadrilateral element together with it's parent element is illustrated in *Figure 2-17.*

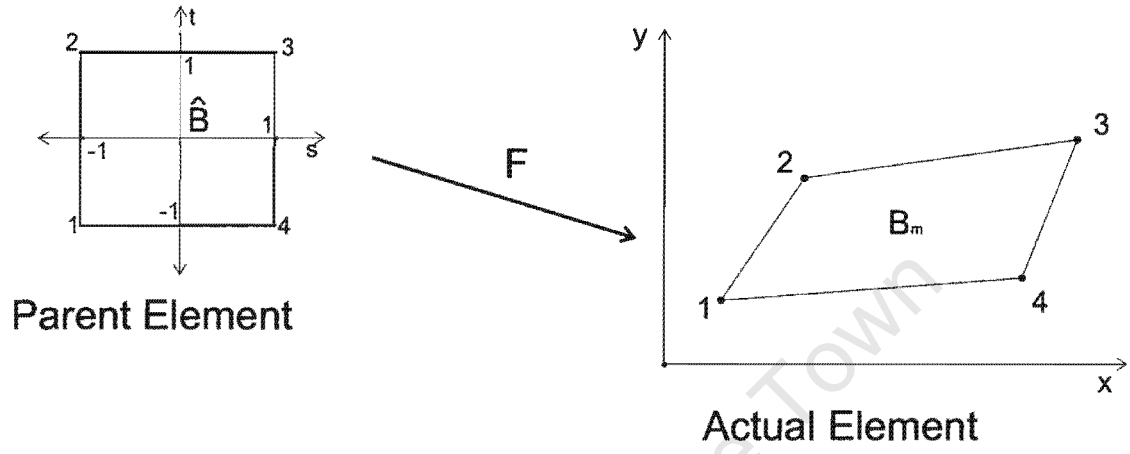

Figure 2-17: The quadrilateral element in natural (parent element) and cartesian (actual element) coordinate systems, mapping $\hat{B}$ onto B_m.

A point in a tri-linear hexahedral isoparametric element is defined in terms of $\mathbf{g} = (g,q,r)$ where $0 < g < 1$, $0 < q < 1$ and $0 < r < 1$. The mapping onto the parent element takes the form

$$\mathbf{x} = \mathbf{x}(\mathbf{g}) = \sum_{i=1}^{n} x_i \hat{\phi}_i \tag{2.109}$$

The sum is taken over all nodes in the element. The linear hexahedral isoparametric element has 8 nodes which are numbered as shown in *Figure 2-18.*

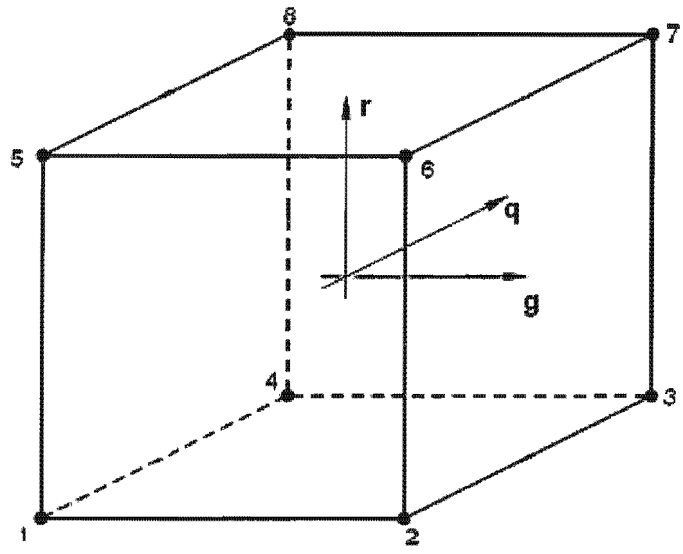

Figure 2-18: A hexahedral isoparametric element.

The stiffness matrix $\mathbf{K}$ for an isoparametric element can easily be directly constructed with the use of interpolation functions. Interpolation (or shape) functions are defined as functions which have a value of one at one nodal point and zero value at all other nodal points. To define a displacement vector $\mathbf{u}$ at a point in the element in terms of nodal displacements, an interpolation function is needed corresponding to each nodal displacement. The equation then becomes for the hexahedral element:

$$u' = \begin{bmatrix} \hat{\phi}_1 & 0 & 0 & \hat{\phi}_2 & 0 & 0 & \cdots & \hat{\phi}_8 & 0 & 0 \\ 0 & \hat{\phi}_1 & 0 & 0 & \hat{\phi}_2 & 0 & \cdots & 0 & \hat{\phi}_8 & 0 \\ 0 & 0 & \hat{\phi}_1 & 0 & 0 & \hat{\phi}_2 & \cdots & 0 & 0 & \hat{\phi}_8 \end{bmatrix} \tag{2.110}$$

where

$$\hat{\phi}_1 = \tfrac{1}{8}(1-g)(1-q)(1-r) \quad \hat{\phi}_5 = \tfrac{1}{8}(1-g)(1-q)(1+r)$$
$$\hat{\phi}_2 = \tfrac{1}{8}(1+g)(1-q)(1-r) \quad \hat{\phi}_6 = \tfrac{1}{8}(1+g)(1-q)(1+r)$$
$$\hat{\phi}_3 = \tfrac{1}{8}(1+g)(1+q)(1-r) \quad \hat{\phi}_7 = \tfrac{1}{8}(1+g)(1+q)(1+r)$$
$$\hat{\phi}_4 = \tfrac{1}{8}(1-g)(1+q)(1-r) \quad \hat{\phi}_8 = \tfrac{1}{8}(1-g)(1+q)(1+r)$$

The stiffness and force integrals can be written for each element in term of the isoparametric element. In order to do this it is necessary to define the Jacobian matrix

$$\mathbf{J} = \frac{\partial \mathbf{x}}{\partial \mathbf{g}} = \begin{pmatrix} \frac{\partial x}{\partial g} & \frac{\partial y}{\partial g} & \frac{\partial z}{\partial g} \\ \frac{\partial x}{\partial q} & \frac{\partial y}{\partial q} & \frac{\partial z}{\partial q} \\ \frac{\partial x}{\partial r} & \frac{\partial y}{\partial r} & \frac{\partial z}{\partial r} \end{pmatrix}. \tag{2.111}$$

In calculating the matrix $\mathbf{B}$ the derivatives of the basis functions are used. The Jacobian can then be employed to map $B(\mathbf{x}) \rightarrow \hat{B}(\mathbf{g})$ by using

$$\frac{\partial \phi_i}{\partial \mathbf{x}} = \mathbf{J}^{-1} \frac{\partial \phi_i}{\partial \mathbf{g}}. \tag{2.112}$$

Also needed to transform $\mathbf{K}$ and $\mathbf{F}$ is

$$dV = dxdydz = \det \mathbf{J} dgdqdr = Jd\hat{V} \tag{2.113}$$

Similarly

$$dS = jd\hat{S} \tag{2.114}$$

$\mathbf{K}(\boldsymbol{\alpha}) = \mathbf{F}$ can then be written for each element in terms of its natural coordinate system.

$$\hat{\mathbf{K}}_m(\boldsymbol{\alpha}) = \int_{\hat{B}_m} \hat{\mathbf{B}}^T \boldsymbol{\sigma}(\boldsymbol{\alpha}) J d\hat{V} \tag{2.115}$$

$$\hat{\mathbf{F}}_m = \int_{\partial \hat{B}_m} \mathbf{t} \bullet \boldsymbol{\varphi} j d\hat{S} + \int_{\hat{B}_m} \mathbf{f}^B \bullet \boldsymbol{\varphi} J d\hat{V} \tag{2.116}$$

The integrals that define $\mathbf{K}$ and $\mathbf{F}$ must be calculated to solve the displacement problem. These integrals can usually not be solved analytically and must be solved using numerical integration of which the Gaussian Quadrature formulation is used in this work to solve the integrals. It consists of evaluating the function at certain points defined by the roots of Legandre polynomials, multiplying each function value obtained by a predefined constant ad then summating the results, as shown in equation (2.117).

$$\int_B f(\mathbf{x}) dV = \sum_{i=1}^{k} c_i f(\mathbf{x}_i) \tag{2.117}$$

Convergence Criteria

Equation (2.110) can be expressed as some function of nodal displacement in the form

$$\Psi(\alpha^r) = 0 \tag{2.118}$$

Let α_i be the i^{th} approximation to the solution and let $\Psi(\alpha_i) = \Psi_i$. Then α is solved to a close approximation using Newton's method. Ψ_i must therefore converge to zero as i increases and is known as the force residual. The following criteria are checked to establish whether a converged solution has been obtained within the increment:

(1) The largest force residual must be less than or equal to R times the instantaneous magnitude of the force at the time specified time, averaged over the entire body. $\mathbf{R}$ has a default value of 0.005.

(2) The largest displacement correction at any node in the current Newton iteration must be less than or equal to C times the maximum nodal displacement difference between the current and previous increment. C has a default value of 0.01.

In ABAQUS the size of the time increment for the next step can be controlled automatically in which case the ease of convergence of the current increment is used to check whether the time increment for the next step should be increased, decreased or stay the same. This allows for fast convergence of each increment and therefore also the overall problem solution. The automatic time incrementation is controlled by predefined parameters I_G, I_L, D_D and D_B. If the number of iterations needed for current increment is less than I_G, then the next time increment is increased by factor D_D -1. If the number of iterations needed however, is less than I_L, then the time increment will be decreased by a factor 1-D_B. The default values for these parameters are $I_G = 4$, $I_L = 10$, $D_D = 1.5$ and $D_B = 0.75$.

Contact Modelling

Different contact formulations are possible but in the version of ABAQUS (6.4-5) used, only surface-to-node contact is available for use in finite sliding problems between deformable bodies. Master-Slave surface-to-node contact will be discussed in this section.

The slave surface is described by the element nodes on the surface while the master surface is described by an element based surface. A contact pair is defined between a slave node and the element surfaces on the master surface. The distance between them is defined as d and a distance d_{crit} is defined. If $d < d_{crit}$ the contact pair is assumed to be in the closed state (the pair is in contact) and if not it is assumed to be open. If $d < 0$ it means the slave node has penetrated the master surface. In such a case overclosure has occurred which is not allowed and the increment will be attempted again using a smaller time increment.

In closed contact pair, contact pressure is exerted by the master surface on the slave surface, to which it will respond by displacement as for any other surface traction.

In contact problems, severe discontinuity iterations can occur in each increment in addition to the normal convergence iterations. A severe discontinuity iteration occurs if contact conditions have changed, i.e. if contact pairs have opened or closed. When the contact state has converged the increment will continue with the normal iterations.

Stabilization

The difference between the internal and external forces will be equal to the force residual at each iteration i. Therefore from equations (2.104) and (2.118) together with the definition of the force residual it can be written that

$$\mathbf{K}(\boldsymbol{\alpha}_i) - \mathbf{F} = \boldsymbol{\Psi}_i = \mathbf{R}. \tag{2.119}$$

However in some models local instabilities can occur resulting in a local transfer of strain energy from one part of the model to another. This instability can be avoided by the addition of volume proportional damping to the system of equations. Viscous forces can be added to the global system of equilibrium equations in the form of

$$\mathbf{F}_v = c\mathbf{M}^*\mathbf{v} \tag{2.120}$$

where c in a damping factor, $\mathbf{M}^*$ is the artificial mass matrix calculated with unit density and $\mathbf{v}$ is a vector of nodal velocities, calculated by the increase in nodal velocities over time. If the nodal velocities are small the viscous forces in that region should be small enough to be negligible, however if large nodal velocities are experienced (as would be

the case in local instabilities) the viscous forces will dampen the unstable behaviour. The viscous forces are added to the equilibrium equations as follows:

$$\Psi_i - \mathbf{F}_v = \mathbf{R} \tag{2.121}$$

2.6.2 Finite Element Modelling of Intravascular Stents

The literature offering the best comparison to the wire support structures modelled in this thesis is that pertaining to FEM models created for the analysis of intravascular stents. These tiny wire structures are inserted into arteries that have become clogged over time by a build up of fat, cholesterol and other substances. An intravascular stent is a metal mesh made either from fine wires or by laser cutting the desired patterns into tubes. They are set into place to act as a long term support structure for a critically stenosed artery [3, 6, 8, 9].

Experimental mechanical tests on these small structures are difficult and in vivo tests on stent-artery interactions are not possible due to the risk it holds for the patient. Since stents are mechanical solutions to biological problems, it is necessary that their exact mechanical properties be known The FEM has proved to be useful in optimising stent mechanical properties, leading to better long term effectiveness [1-3, 5, 6, 8].

Although structurally similar, many differences exist between the investigated support structure and intravascular stents. Selected FEM models of intravascular stents will be discussed in this section. These models all have different objectives but in this section attention will be focussed on the strategies followed in creating the models. Later the differences between models in this section and the wire support structure modelled in this work will be discussed.

Migliavacca et al [2] showed how FEM can be used to model intravascular stents by conducting experimental tests and comparing the results to the FEM results. Three dimensional CAD model was created of he stent geometry. The model was meshed using ten-noded tetrahedral elements and a sensitivity analysis was conducted to determine the optimal mesh density. A Von-Mises plasticity model with hardening was used to describe the 316L stainless steel material. A uniform linearly increasing radial pressure was applied to the internal surface of the stent. The model was analysed using ABAQUS/Standard with the Newton-Raphson solution method due to the non-linearity

caused by the material plasticity. Mechanical properties of the stent after load removal were investigated. Values at corresponding stent diameters in experimental and computational tests were compared, results at corresponding pressure values differ due to some of the pressure being absorbed by the balloon in the experimental tests. Mechanical properties for which FEM was shown to be a useful investigative tool were stress distribution and displacement results such as longitudinal and radial recoil, foreshortening and dogboning effects.

Migliavacca et al [3] also conducted FEM studies to show the effect of the variation of geometrical features on a stent's mechanical behaviour in order to optimise the design of intravascular stents. A three dimensional model of a typical diamond shaped intravascular stent was created as well as models with geometric variations on this design. Variations in slot length, strut thickness and metal/artery area index were considered. Only one twelfth of the circumference and half of the length was modelled on account of symmetry. The stent models were meshed with eight-noded brick elements and a sensitivity analysis was conducted to determine the effect of mesh density on the results. The material model used was Von Mises-Hill plasticity with parameters describing 316LN stainless steel. Boundary conditions were applied to account for the symmetry simplifications. The main limitations of this study are the absence of contact between the stent and the artery, balloon and/or blood flow. Linearly increasing pressure loading was applied directly to the inner surface of the stent and then removed to simulate the balloon removal. The fact that material and geometric non-linearities in these problems are difficult to simulate was highlighted. Output quantities were displacement results (distal radial recoil, central radial recoil, longitudinal recoil, foreshortening and dogboning) as well as stress distribution [3].

Tan and Liu [1] analysed the difference in mechanical behaviour resulting from variations in stent geometry while establishing a general FEM procedure to model a coronary stent. The geometry was developed in the x-y plane and then mapped onto a cylindrical coordinate system. Slight variations in the stent geometries were also considered. Meshing was done with beam elements and a material approximating surgical steel was implemented. An artery with a solid plaque protrusion was added to the model geometry. The loading of the stent was conducted through radial displacement of the stent nodes inside the stenosed artery. Stress distributions, deployment pressure necessary and strain results were discussed and it was reported that subtle variation in

design could considerably affect the deployed state of the stent which was related to the biological response of the artery through comparison experimental results.

The goal of the model created by Dumoulin and Cochelin [4] was to show how FEM can be used to analyse the mechanical behaviour of endovascular prosthesis during and after implantation. After consideration of in vitro test results, it was decided to model a unit cell of the stent pattern and assume infinite prosthesis under uniform radial expansion. A three dimensional curved cell was subjected to internal pressure and found to have larger circumferential than radial stresses during expansion. The final model consisted of a two dimensional planar cell meshed with two dimensional quadratic continuum elements. Elastic and perfectly plastic material models were used to describe 316L stainless steel. Boundary conditions were used to account for the symmetry simplifications and the cell was deployed by prescribed displacement under plane stress assumptions. The results analysis focussed on the response of the stent to external compressive stresses, displacements, as well as stress and strain distributions [4].

Etave et al [5] studied a number of mechanical properties of intravascular stents as well as the effect of geometric variations on these properties. Four geometric variations were considered. A material model for stainless steel 316L was implemented with the used of a standard stress strain curve for the annealed material and boundary conditions were applied to limit flexion. Lack of realistic contact between the stent and a deformable balloon and artery model is given as a limitation of this study. Loading consisted of each node in a model first undergoing increasing radial displacement followed by decreasing radial displacement, simulating the deployment through balloon inflation followed by the balloon removal. 7 mechanical parameters were studied: Pressure necessary for stent deployment, determination of intrinsic elastic recoil, resistance of stent to external compressive forces, stent foreshortening, stent flexibility as well as stress and residual strain distributions [5].

Walke et al [6] conducted a study which focussed on determining mechanical behaviour of stents to aid in the optimization of the design. To show that realistic results were obtained from the FEM models used, numerical results were compared to experimental results. A three dimensional model of a single segment of the design was used as the geometry of the model due to the repetitiveness of the design. A material model describing 316L stainless steel was used for the stent structure. Appropriate initial and

boundary conditions were added to describe the experimental behaviour of the structure. An artery was modelled as a thin walled pipe of equal length than the stent section and was assigned a linearly elastic material model. Contact between the stent and the artery was modelled. Radial expanding pressure was increased incrementally on the inner surface of the stent from 0 to 3750mmHg, simulating balloon expansion. Experimental tests results correlated well with that of the numerical analysis. Deployment pressure, stress and strain distributions in the stent and luminal surface of the artery were discussed.

David Chua et al [90] aimed to investigate the interaction between the stent and artery with plaque protrusion. A three dimensional model of one eighth of the stent was created due to circumferential symmetry. Linear brick elements are used and the element numbers for all the different components are given. A finer mesh is used at the proximal anastomosis, as the plaque protrusion was modelled here and this area is therefore predicted to be important for accurately capturing the stress distribution. The stent was modelled using a model for stainless steel 304. Boundary conditions accounting for the symmetry simplification were applied as well as conditions preventing rigid body motion and longitudinal motion of any of the components. A model for the artery and balloon delivery system was included and contact was defined between all surfaces which could come into contact. Pressure was increased on the inner surface of the balloon from 0mmHg to just over 18 000mmHg and then decreased again to 0mmHg. Stress distributions in both the stent and the artery were determined and deployment pressure, elastic recoil and foreshortening of the stent was discussed.

Holzapfel [22, 91] went even further in analysing the interaction between the stent and the artery wall. They established a technique of modelling different stent designs inserted into a stenosed artery, the geometry of which can be determined from MRI imaging and can therefore be patient specific. A three dimensional artery structure was created from MRI images and three different stent geometries were modelled. The artery is modelled with linear 8-noded hexahedral elements, but with linear 20-node elements in contact regions; the stents are modelled with quadratic (second order) hexahedral elements. A stainless steel was modelled for the stent through the use of a neo-hookean material model. Boundary conditions are applied to prevent rigid body motion and longitudinal motion of the artery. Frictionless contact was defined between the stent and the artery. Due the absence of a balloon model, numerical results were expected to deviate from

experimental tests as in a physical situation the balloon exerting the pressure would bulge between the stent struts. A pressure load is applied directly to the stent as this is allows more realistic displacement behaviour of the stent than displacement loading. The group studied variations is strut thickness, diameter mismatch and unit cell geometry and reported on the pressure concentration on the arterial wall lumen. Focus was placed on the intimal pressure concentration caused by the stent struts, the stress change within the arterial wall and the luminal changes during stenting. This was done as endothelial cell damage and medial SMC damage are determinants for restenosis after stenting. [22, 91].

As different stent designs have different restenosis rates, Lally et al [7] analysed the interaction of the stent with the artery wall showing how two different stent designs provoke different levels of stress in the vascular wall. The modelled geometry also consisted of three dimensional models of the repeatable units of the stents due to the high circumferential symmetry. The models were generated in a plane and then mapped onto a three dimensional cylindrical coordinate system. Higher mesh density was defined in regions of contact and high stress gradients. A linearly elastic model for 316L stainless was used to describe the stent material. Boundary conditions were applied to prevent rigid body motion and account for circumferential symmetry. An artery, represented by an idealized cylindrical vessel, and a localized crescent shaped stenosis was modelled on the lumen. Both were described by Mooney-Rivlin hyperelastic material models. Frictionless contact was defined between bodies and both were allowed to deform. The loading definition consisted of the vessel being expanded to an inner diameter larger than the outer diameter of the stent. The luminal pressure on the vessel was then decreased from an expanded state to 100mmHg, resulting in compressive forces being placed on the stent structure. Radial retraction was different for the different stent designs and the optimum stent should retract enough during the cardiac cycle to prevent overstretching the vessel wall and minimizing tissue-prolapse (tissue protrusion between stent struts). Radial retraction, tissue prolapse, contact area, stress distribution The main limitation to this study is that no rupture or damage mechanism is defined for the plaque, with the level of the stress that was observed was high enough to cause plaque rupture [7].

Petrini et al [8] investigated stent flexibility in both the expanded and unexpanded state by means of FEM and compared for different designs towards the optimization of the stent design. The stent designs that were modelled consisted of tubular-like rings which support the vessel after deployment and bridging members which link he rings in a

flexible way to aid in the delivery process. Only a portion of the stent was studied due to the repetitiveness of the design (2 rings and a bridging member). Two different designs were considered. The mesh consisted of 10-nonded tetrahedral elements and was sufficiently refined to ensure the solution was independent from the mesh. Von Mises-Hill plasticity with isotropic hardening with material parameter for 3161 stainless steel was use to describe the material behaviour. The longitudinal ends of the model were rotated by a predefined angle and bending was considered about both axes perpendicular to the longitudinal axis. ABAQUS/Standard was used with the Newton-Raphson solution method to account for the material non-linearity. The study reinforced that the methodology is able to quantitatively describe local details in stent structural behaviour. The main limitation in this model is the absence of a delivery system.

Perry et al [92] discussed how FEM can be used in determining the fatigue life of stents if the magnitude and nature of the cyclic loading is known. The small size of implantable stent devices limits the significance of quantitative measurements, but with the incorporation of FEM these devices can be tested before expensive prototypes are manufactured. The fatigue depends on the mean and alternating stress states. A Goodman or Modified Goodman analysis can be performed. This graphical approach uses the amplitude of alternating stress, the mean stress and the stress limits of the material. A fatigue limit is then defined by a line drawn from the endurance limit on the y-axis (alternating stress axis) to the ultimate strength of the material on the x-axis (mean stress axis). The study also notes that experimental testing and simulation enhance each other as methods of characterisation of devices.

A study by McGarry et al [32] looked at the performance of stents on a micromechanical level. They only modelled a unit cell of the stent design due to the periodicity of the design and used a two-dimensional representation with generalized plane strain.. 316 stainless steel was described by two different material models. The first was isotropic elasticity with plastic deformation defined through J_2 flow theory. The second used a crystal plasticity material model. Boundary conditions were added to account for symmetry simplifications. Loading included stent deployment defined through displacement separation of stent struts, then recoil upon balloon deflation. This was followed by a simulation of a cardiac cycle defined through planar expansion and contraction of an arterial pressure pulse. The first model showed a stress and strain field which spatially varied smoothly while the crystal plasticity showed non-uniform and

localized stress and strain fields. There was however a strong correlation between the global model predictions and experimental data also strongly supports the results. The recoil values are lower for the crystal plasticity, while the foreshortening values are the similar. Most importantly, higher factors of safety are predicted for the crystal plasticity based on a Goodman diagrams. This model shows the benefit of using a microscale material model as the more realistic values allows for a more effective design [32].

The previous models all described the behaviour of balloon-expandable stents, while the next models will deal with self expandable stents. Self expandable stents differ mainly in fatigue life and stiffness and are often made of Nitinol. Upon release from the delivery system these stents undergo a transformation from the Martensite to the Austenite phase during which they expand to support the artery. The structure then responds to systole-diastole-driven cyclic distension of the vessel due the employment of its pseudoelastic range [9, 10].

A Nitinol stent model was created by Gong and Pelton [9]. They highlight that the material behaviour of Nitinol generates analysis difficulties due to its highly non-linear behaviour and raise the fact that an efficient constitutive model needs to be implemented since numerical iteration will be necessary during the analysis. A single diamond shaped unit cell of the stent was modelled to represent the stent design. The strong non-linearity of Nitinol's material behaviour discourages complicated analyses. A Nitinol UMAT is used to define the material behaviour in ABAQUS and is based on a general plasticity description by Aurichio and Taylor [79, 80]. The UMAT has been previously demonstrated to predict both uniaxial material response and stent behaviour accurately. They propose that the Austenite finish temperature could be changed to achieve the optimum design. Load and displacement results were compared to experimental data and shown to agree well. Stent stiffness was also accurately predicted. They showed that FEM modelling of Nitinol stents with the developed ABAQUS Nitinol UMAT can be used to analyse fatigue life and optimize the device functionality [93].

Self expandable Nitinol stents were also discussed by Whitcher [10]. A model of a self expandable Nitinol stent was created with minimum detail using all the available axes of symmetry. One eighth of a symmetric unit cell was modelled and meshed using 27-node elements and a sensitivity analysis was done to verify the results' dependence on mesh density. The Von Mises yield-criterion elastic-plastic material model in ADINA was

chosen. Boundary conditions were defined to account for the symmetry simplifications and pressure loading was applied directly to the stent. The regions of peak stresses were identified and a fatigue analysis was done through the use of a Goodman diagram [10].

CHAPTER 3: MATERIALS AND METHODS

3.1 Nitinol Material Characterisation

A uniaxial tensile test was conducted on Nitinol wire samples, the same as those used in creating the reinforcing structures. The purpose of the tests was to characterise the Nitinol material by extracting values needed for the material model definition used in the FEM analysis.

3.1.1 Experimental Setup

The following equipment was used:

- Instron 5544 tensile testing machine with 500N static load cell
- Water bath
- Heating element
- Thermometer
- Temperature Controller
- Customised clamps
- Clamp adaptors

The experimental setup is shown in *Figure 3-1 (a)*. Tests were conducted on an Instron 5544 tensile testing machine with a 500N static load cell. Samples remained submerged in distilled water at 37°C (physiological temperature) throughout the test. The water bath (*Figure 3-1(b)*) contained the heating element and thermometer which were both connected to the external temperature controller. Customised clamps (*Figure 3-1(c), (d)*) were used to connect the samples to the Instron machine.

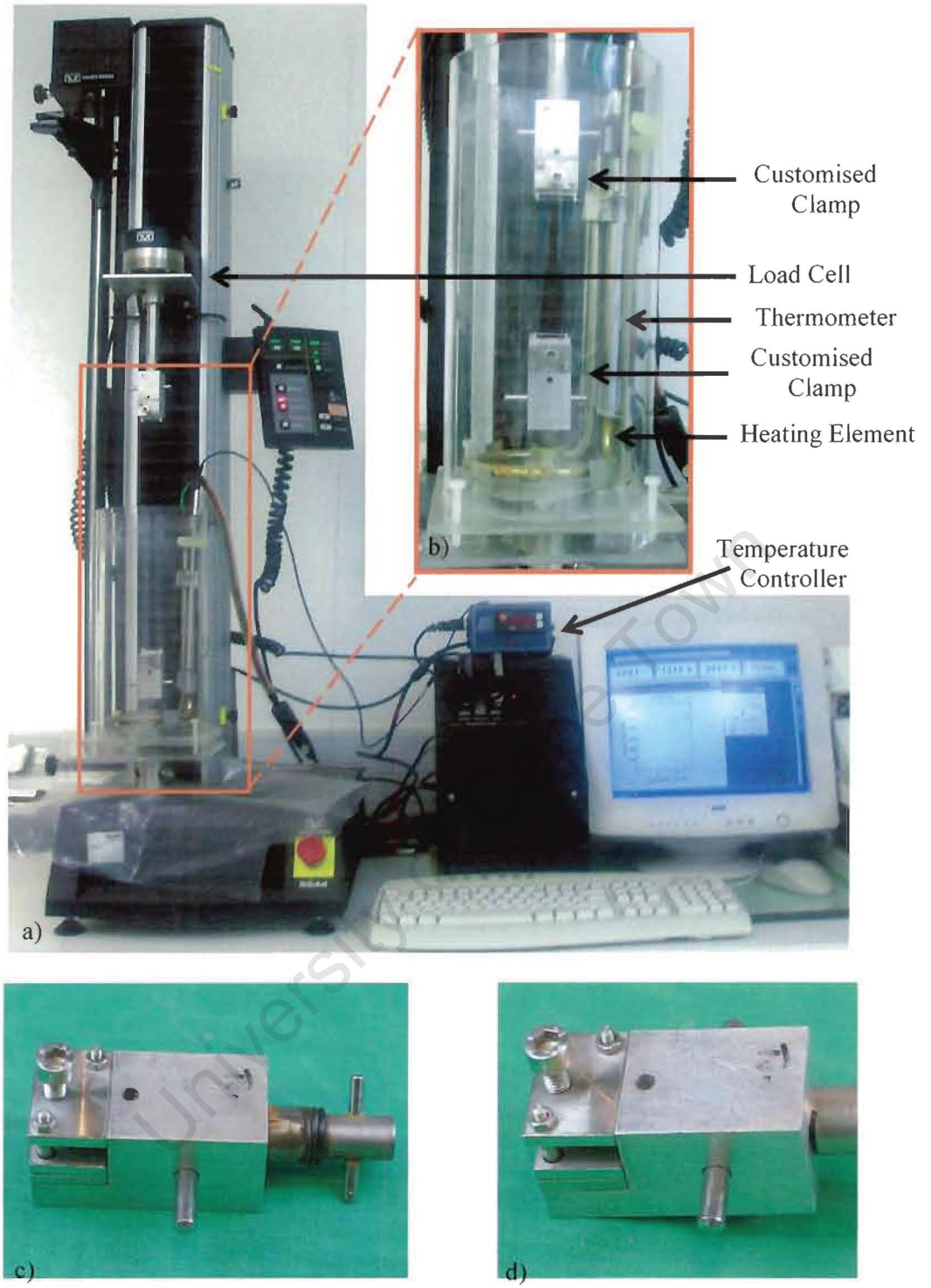

Figure 3-1: (a) Equipment setup for the tensile test, (b) the water bath with heating elements, thermometer and clamps, (c) bottom clamp and (d) top clamp.

3.1.2 Test Samples

A total of 12 Nitinol wire (BB grade for medical application) samples were tested; three different wire diameters with four samples of each diameter. The three diameters were 0.05m, 0.0635mm and 0.075mm. The samples were all 100 mm in length and were heat treated in the same way as that of the knitted wire support structures.

3.1.3 Sample Preparation

To prevent pullout of the clamps, the Nitinol wires were fixed to aluminium plates which were inserted into the clamps. Each plate surfaces were made slightly course with fine grain sandpaper and then cleaned with alcohol to remove all residues. Wires were attached to the plates with two-component epoxy glue such that the wire length between the plates was 100mm. A prepared sample is schematically illustrated in *Figure 3-2*.

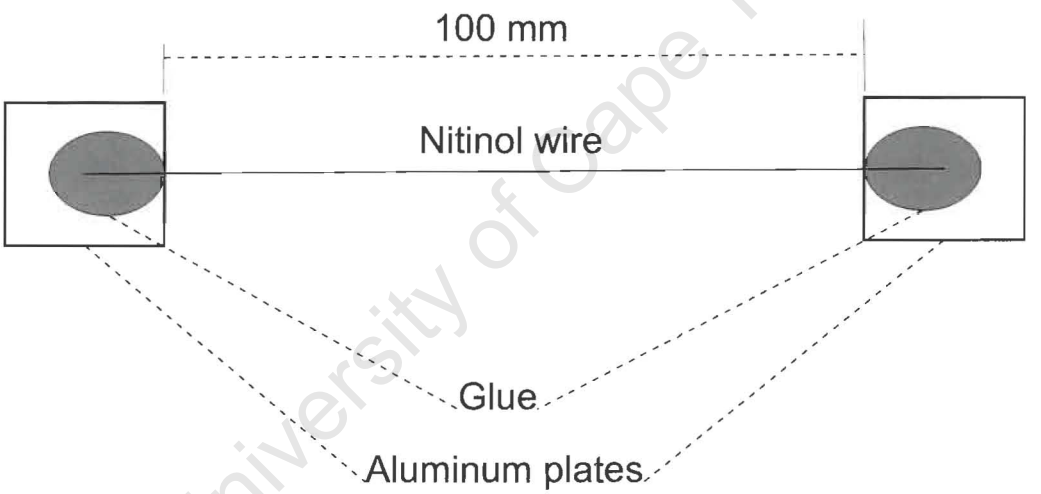

Figure 3-2: Prepared Nitinol wire sample for tensile testing.

3.1.4 Testing Procedures

The uniaxial tensile test procedure comprised 99 cycles from 1% to 4.5% strain (the first cycle started from 0% strain). Of these 99 cycles data was captured for the first 3 cycles and the last 2 cycles. This was followed by two cycles from 1% strain to 8% strain and a cycle from 1% to 20% strain for which data was recorded. The cycling was conducted at a cross-head speed of 38mm per minute. The speed was chosen to be the same as the speed used in these previous tests, as the data was also used in different study to compare

to this previous test data. Merlin Software associated with the Instron machine controlled the testing procedure.

3.1.5 Data Analysis

The data files created by the Merlin software package were processed in Excel. Data for each sample was obtained from a stress (MPa) vs. strain (%) plot of the cycles for which data was recorded. Each sample produced more than one data set per region, as data was captured from multiple cycles. The stress/strain graphs for each sample can be separated into 4 regions: The Austenite region, Loading Transformation region, Martensite region and Unloading Transformation region as shown in *Figure* 3-3.

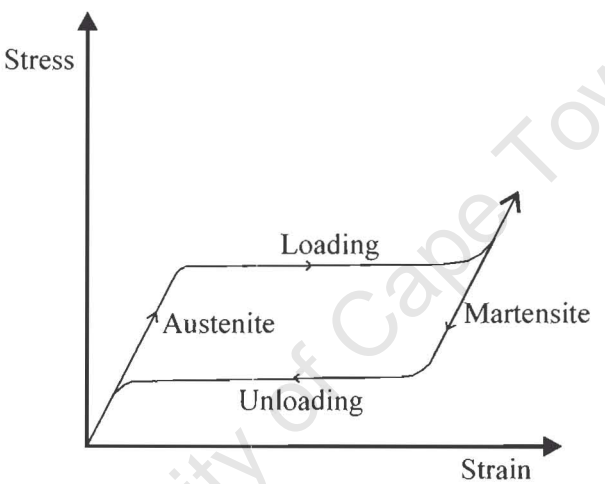

Figure 3-3: Theoretical stress vs. strain plot for Nitinol with the four different regions indicated.

Linear equations describing the different regions were obtained from cycles 98 to 102 for all the samples, by adding trendlines to the relevant regions and then determining the average trendline for each region. The following figures all have cycle 1 to 3 plotted for comparison. In *Figure 3-4* the stress vs. strain plot for cycles 98 and 99 is shown. Two equations were obtained for the Austenite region and two for the Loading Transformation region from the data ranges indicated.

In *Figure 3-5* the stress vs. strain plot for cycles 100 and 101 is shown. One equation was obtained for the Austenite region (from cycle 100), one for the Loading Transformation region (from cycle 100), two for the Martensite region and two for the Unloading Transformation region, with the relevant data ranges indicated.

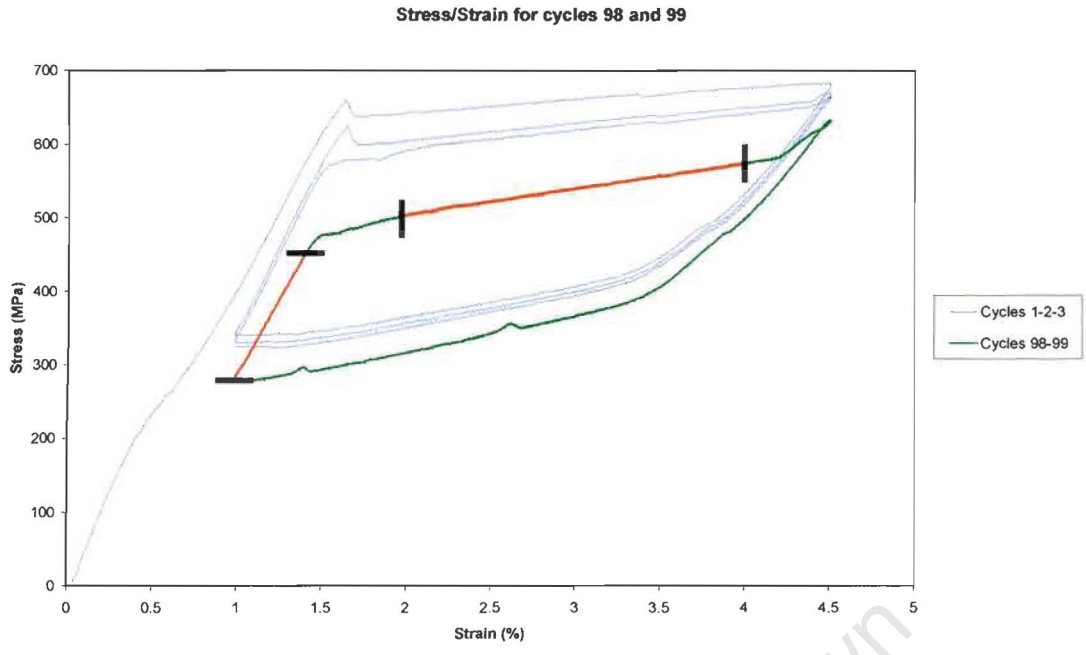

Figure 3-4: The stress vs. strain curve for tensile test cycles 98 and 99, extending up to 4.5% strain.

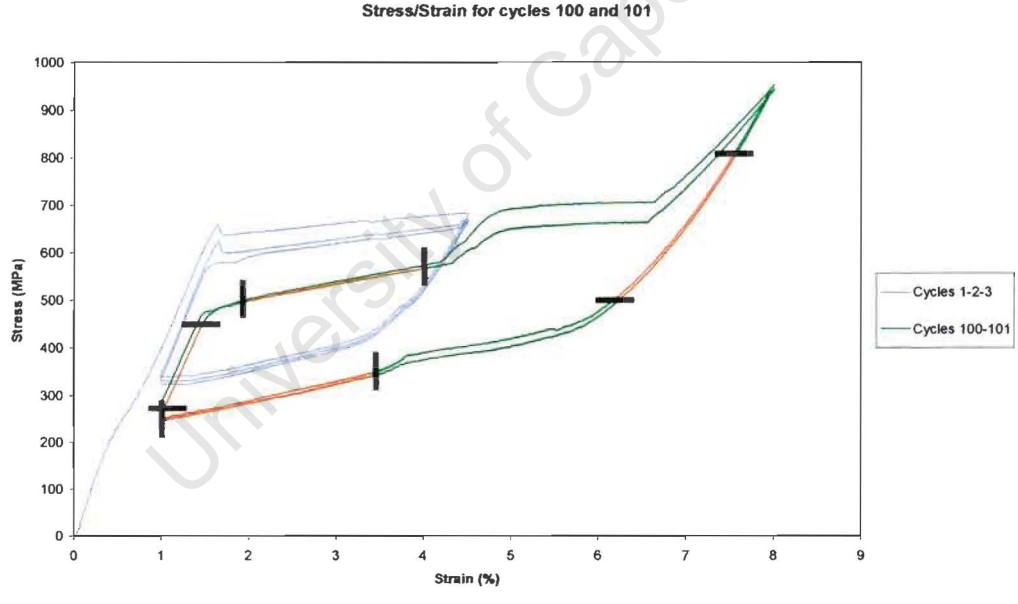

Figure 3-5: The stress vs. strain curve for tensile test cycles 100 and 101, extending up to 8% strain.

In *Figure 3-6* the stress vs. strain plot for cycle 102 is shown. One equation was obtained for the Martensite region, with the relevant data ranges indicated.

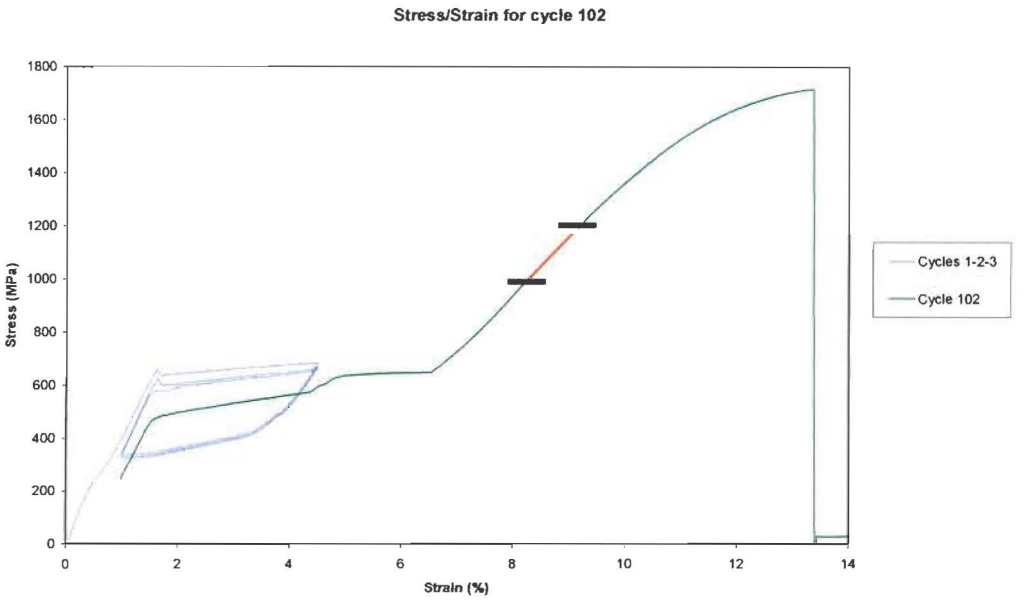

Figure 3-6: The stress vs. strain curve for tensile test cycle 102, extended up to 20% strain, but failing at around 13,2%.

For each region, an average equation was obtained by considering all relevant equation in all the samples. The following values were obtained and are indicated in *Figure 3-7*:

- Austenite young's modulus: The average gradients from the Austenite region equation (*Figure 3-7* (1)).
- Martensite young's modulus: The average gradient from the Martensite region equation (*Figure 3-7* (2)).
- Transformation strain: The strain–intercept of the Martensite region equation (*Figure 3-7* (3)).
- Start of transformation loading stress: Determined by extrapolating the point of intercept between the average equation for the Austenite and Loading Transformation regions (*Figure 3-7* (4)).
- End of transformation loading stress: Determined by extrapolating the point of intercept between the average equation for the Loading Transformation and Martensite regions (*Figure 3-7* (5)).
- Start of transformation unloading stress: Determined by extrapolating the point of intercept between the average equation for the Martensite and Unloading Transformation regions (*Figure 3-7* (6)).

- End of transformation unloading stress: Determined by extrapolating the point of intercept between the average equation for the Unloading Transformation and Austenite regions (*Figure 3-7* (7)).

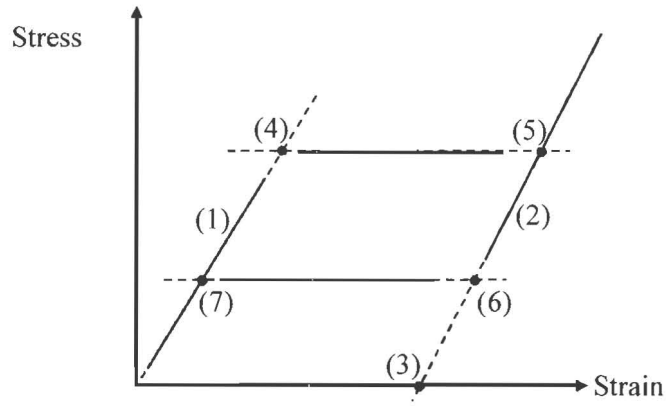

Figure 3-7: Extrapolated values used in the definition of the Nitinol material model.

3.2 Finite Element Models

3.2.1 Model Description

A metal support structure, which represents a component of a vascular graft, was analysed using the FEM. The structure consisted of eight wire-loop pairs (a pair consists of a loop in both longitudal directions) around the circumference of the cylindrical knitted geometry. All the loops were equal in size. This design is illustrated in *Figure 3-8*. This structure has been manufactured to undergo physical testing.

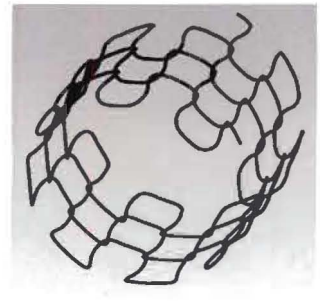

Figure 3-8: Solid 3D geometry of the even loop wire support structure.

3.2.1.1 Geometry

Three dimensional centreline geometry of one single-loop of the structure (provided by Pro-Consulting, Minneapolis, MN, USA, according to request) was used in the model. A

solid single-loop part, illustrated at the centre of *Figure 3-9,* was created from this three dimensional centreline geometry using Pro-Engineer Wildfire 2.0 (Parametric Technology Corporation, Needham, MA, USA). The single-loop solid geometry was imported into ABAQUS CAE 6.4-5 (Abaqus Inc., Providence, RI, USA) and partitioned in the longitudinal and circumferential wire directions to aid in the mesh assignment and contact definitions. The longitudinal partitions are shown in expanded form in *Figure 3-9*. The partitioning allowed separation of the loop into parts with small curvature and large curvature for improved FEM mesh definition while circumferential quarter-partitioning of the wire surface assisted in contact definition. The final assembly is shown in Figure 3-10.

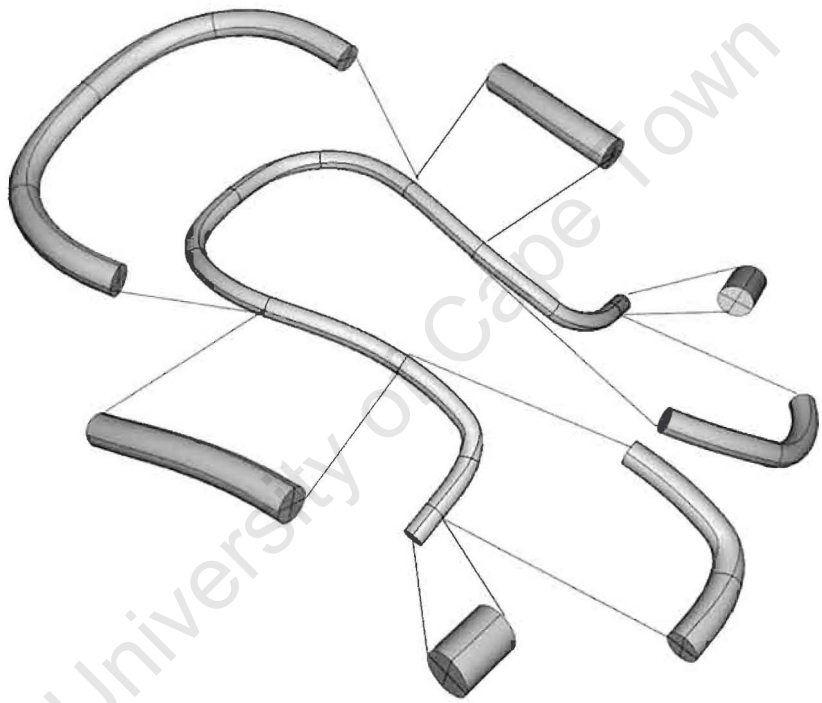

Figure 3-9: Single-loop solid even loop geometry, partitioned in longitudinal and circumferential wire direction. The original geometry is shown in the centre with an expanded view of the circumferential partitions.

The portions making up the loop geometry were added to the assembly in a fashion to represent three loops in the longitudinal direction of the tubular structure. In circumferential direction, the single loop represents a 45^{O} section of the structure. This was sufficient to capture the geometrical features of two circumferentially adjacent loops.

Additional sections of a single loop were incorporated into the assembly geometry and can be seen in the positions indicated as front and back in *Figure 3-10 (a).* These sections

were used for definition of boundary conditions which account for the longitudinal geometric simplification.

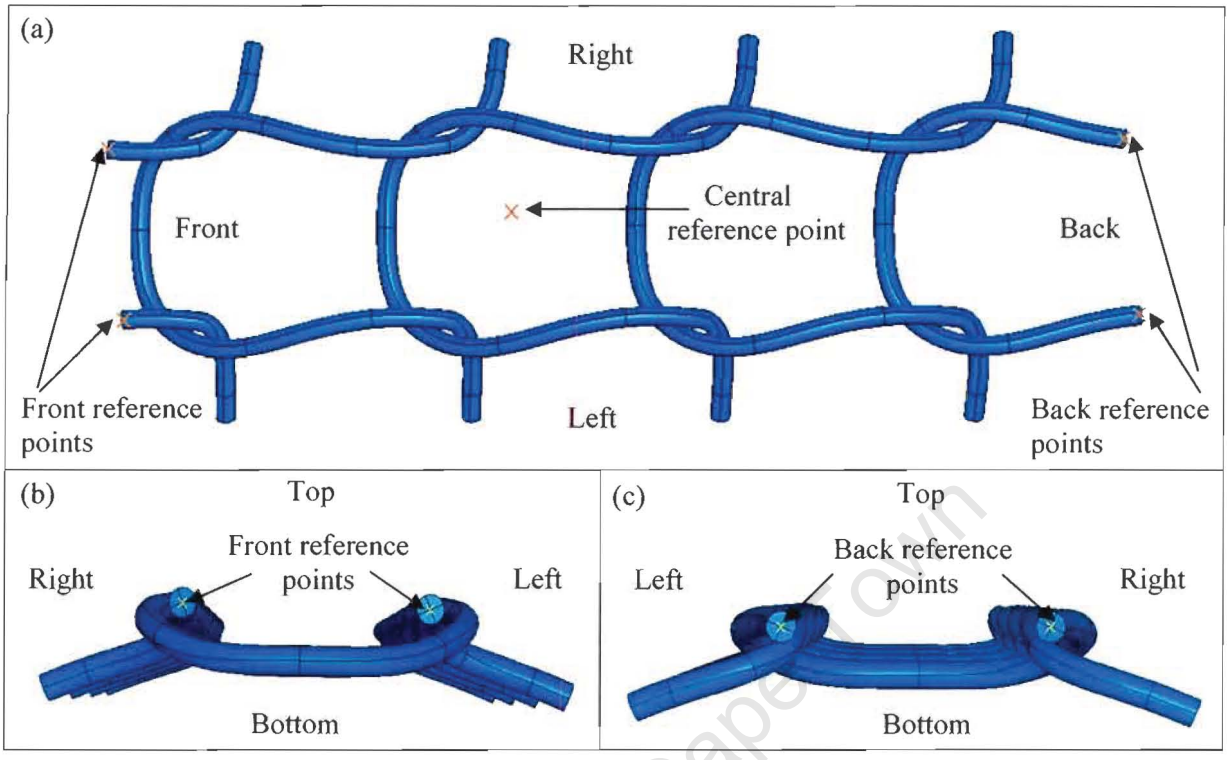

Figure 3-10: Naming conventions for (a) Loop assembly, (b) Front view, (c) Back view.

A central reference point, positioned at the origin of the assembly coordinate system, was used to facilitate the definition of an 'expander' structure used for the loading definition. Four other reference points were created and were used in defining the boundary condition. They are indicated in *Figure 3-10 (a), (b), and (c)*. *Figure 3-10* also illustrates the naming conventions used throughout this thesis.

3.2.1.2 Finite Element Mesh

The single-loop geometry (*Figure 3-9*) was meshed using 8-noded brick elements. Loop regions of low curvature (straighter sections) were assigned four elements through the wire thickness (shown in *Figure 3-11* (b)) and regions with high curvature (more bent section) and were assigned six elements in the one direction through the wire thickness and eight elements in the perpendicular direction through the wire thickness (shown in *Figure 3-11 (c)*). The complete meshed loop is shown in *Figure 3-11 (a)*. Automatic meshing, controlled by user defined seeding, was used to generate the FEM mesh.

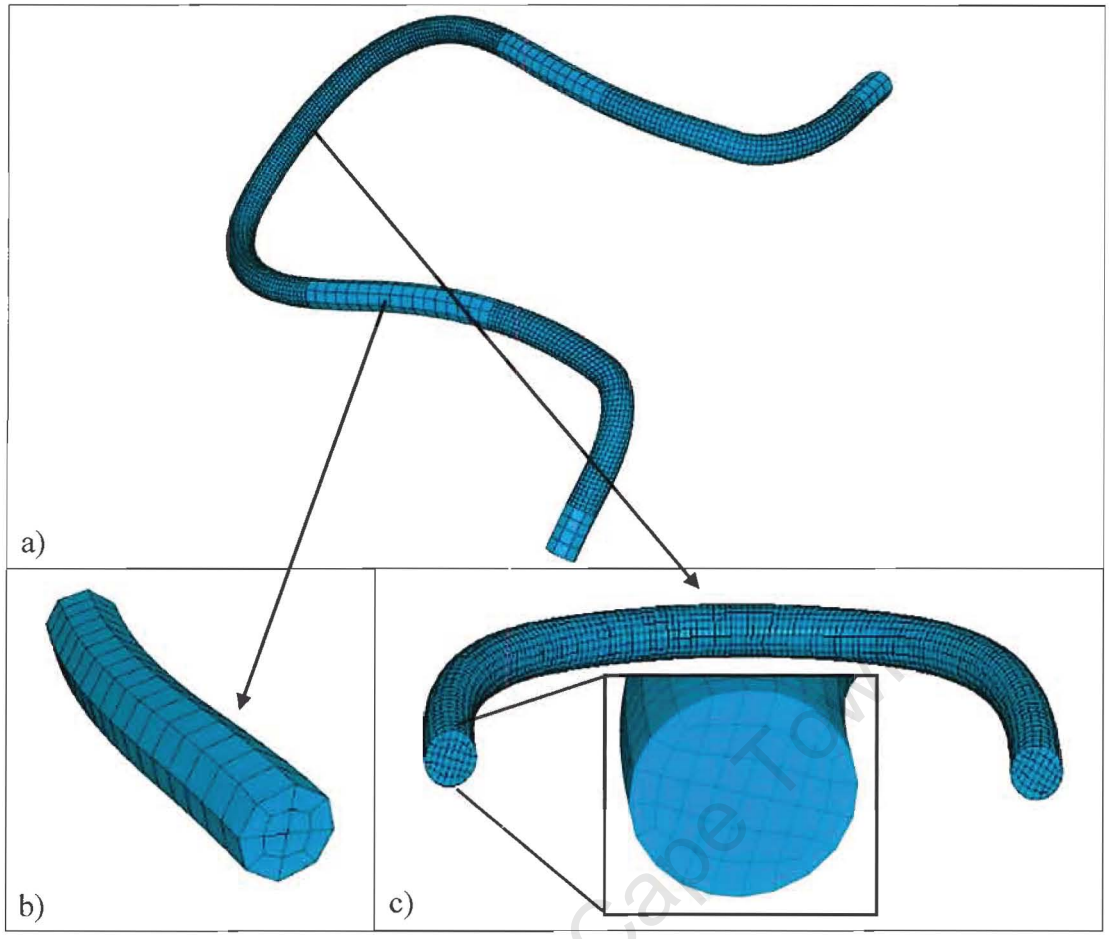

Figure 3-11: Different mesh densities: a) Complete meshed loop (b) Coarse mesh (4 elements through wire thickness) (c) Fine mesh (6/8 elements through wire thickness).

3.2.1.3 Nitinol Material Model

The SMA material model discussed in Section 2.5.4 was used to define the wire material. The material parameters were determined from the experimental tensile tests described in Section 3.1. The properties $\left(\frac{\partial \sigma}{\partial T}\right)_L$, $\left(\frac{\partial \sigma}{\partial T}\right)_{II}$ and ε_V^L could not be obtained from experimental tensile testing and were used as obtained from Medtronic Vascular, Galway, Ireland. All the values are listed in *Table 3-1*.

Table 3-1: Material parameters used for the Nitinol material model.

Parameter	Abbreviation	Unit	Value
Austenite Young's Modulus	E_A	MPa	38992
Austenite Poison's ratio	ν_A	-	0.46
Martensite Young's Modulus	E_M	MPa	21910
Martensite Poison's ratio	ν_M	-	0.46
Transformation Strain	ε^L	-	0.042
Loading Temperature Derivative of Stress	$\left(\frac{\partial\sigma}{\partial T}\right)_L$	MPa/°C	0
Loading Start of Transformation Stress	σ_L^S	MPa	483
Loading End of Transformation Stress	σ_L^E	MPa	610
Reference Temperature	T_0	MPa	37
Unloading Temperature Derivative of Stress	$\left(\frac{\partial\sigma}{\partial T}\right)_U$	MPa/°C	0
Unloading Start of Transformation Stress	σ_U^S	MPa	388
Unloading End of Transformation Stress	σ_U^E	MPa	256
Loading Start of Transformation Stress (Compression)	σ_{CL}^S	MPa	610
Volumetric Transformation Strain	ε_V^L	-	0.04
Number of Annealings to be Performed During Analysis	N_A	-	0

3.2.1.4 Boundary Conditions

Various boundary conditions were assigned to the loop assembly in order to approximate realistic physical behaviour of the structure and to account for geometrical simplifications, i.e. to simulate the effect of stent parts which were not incorporated in the model. The positions of the boundary conditions are indicated in *Figure 3-12*.

The first boundary condition (A in *Figure 3-12*) accounts for the circumferential simplification and symmetry of the structure. It is worth noting that a single loop (therefore also the whole structure) is not truly symmetric since it has a helical component. The movement of all cross-sectional wire surfaces on left and right wire-loop ends in the assembly were restrained to only allow movement in radial direction. This is indicated in *Figure 3-13*.

Partial loop geometries at the front and back of the assembly accounted for the longitudinal geometric simplifications. The boundary conditions on these partial loops (B in *Figure 3-12*) prevented rigid body motion of the structure in the longitudinal direction.

They were applied by restricting motion of front and back reference points, which lie in the centre of their respective cross-sectional end surfaces. Each reference point's motion was coupled to its respective surface, allowing boundary conditions to be defined on the reference points instead of the surfaces themselves. The reference points (and therefore the end surfaces) were prevented from moving in the longitudinal direction, but were allowed to move in the radial and tangential directions. The only rotation allowed was about the longitudinal direction. *Figure 3-14* shows the permitted motion of the right front reference point.

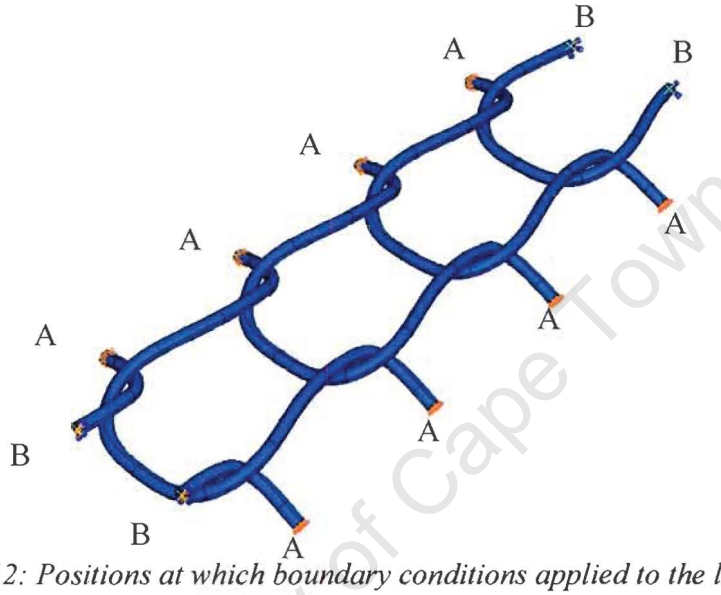

Figure 3-12: Positions at which boundary conditions applied to the loop assembly.

Figure 3-13: Direction of motion permitted for the wire-loop end surfaces at the right and left sides of the assembly (Boundary condition A).

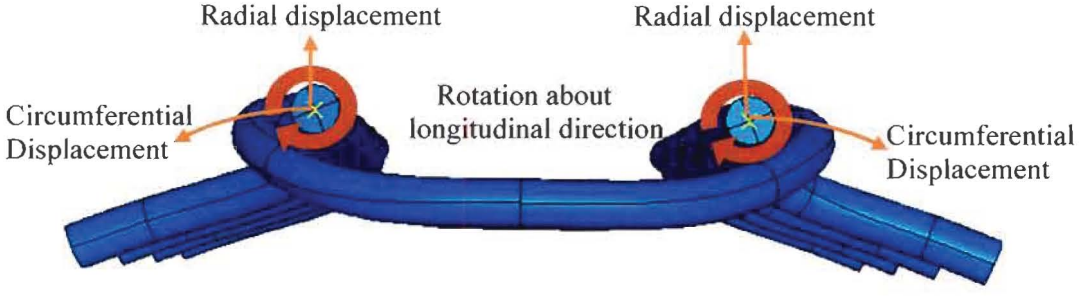

Figure 3-14: Motion permitted for the reference points (Boundary condition B).

This boundary condition (B in *Figure 3-12)* had to be defined via the coupled reference point as the linear brick elements used in the mesh assignment do not support any rotational degrees of freedom. If these rotational degrees of freedom were not restrained from moving, the front and back of the wire assembly would be allowed to lift off the expander during loading, which is inconsistent with the physical problem.

3.2.1.5 Contact Definitions

Contact definitions were required for:

- Contact between the expander surface and the loop wire surfaces (1)
- Contact between different wire surfaces at wire cross-over sections (2)
- Contact at the interfaces of partitions of a single loop. (3)

Wire-expander (condition 1) and wire-wire (condition 2) contact definitions employed Master-Slave Surface-to-Node contact with finite sliding as defined in *Section 2.6.1* The normal and tangential behaviour was defined by softened contact with exponential pressure overclosure and frictionless behaviour respectively. For the wire-expander contact (condition 1), the expander surface was assigned as master surface and the wire surface was assigned as slave surface. In wire-wire contact, the bottom wire was defined as the master surface and the top wire as slave surface. The Pressure-Clearance parameters for the softened contact with pressure overclosure were set to (500 000 MPa, 0mm) and (0MPa, 0.0005mm) as described in *Section 2.6.1*. The contact pairs were set to be adjusted for initial overclosure at the start of the analysis.

In the partition contact definition (3), the wire interfaces were connected to each other using tie constraints. The interface with the higher mesh density was designated the master surface while the lower mesh density surface was the slave surface.

3.2.1.6 Loading

The radial expansion of the graft structure was simulated using a cylindrical surface aligned with the longitudinal axis and positioned luminally to the wire assembly. Radial displacement loading was limited to the expander part and was defined linearly over time. Geometry and motion of the expander was implemented though a user defined rigid cylindrical surface with the use of FORTRAN code. The initial diameter of the expander surface was defined approximately that of the inner diameter of the loop assembly.

Figure 3-15 shows the front view of the wire loop assembly, with the expander surface. No image of the expander is available, since it is not inserted into the ABAQUS assembly, but rather defined through a mathematical description in FORTRAN.

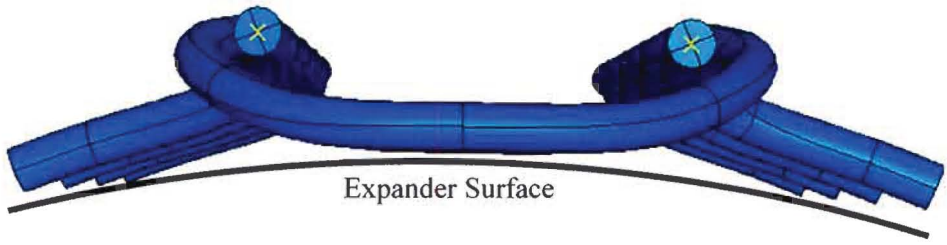

Figure 3-15: Front view of the model assembly, with the expander surface included (Sketch not to scale).

3.2.1.7 Numerical Analysis

The displacement-based analysis was executed in ABAQUS/Standard CAE 6.4-5 in two steps. In the first step contact was established between the expander surface and the wire surfaces and between the wire surfaces. The second step was the analysis step consisting of the radial displacement loading of the expander surface. Automatic time incrementation was used with minimum and maximum admissible time increment size set to $1\text{x}10^{-9}$ and 0.02 respectively. The parameters used to control the incrementation (defined in *Section 2.6.1*) were used with their default values of $I_G = 4$, $I_L = 10$, $D_D = 1.5$ and $D_B = 0.75$. The convergence parameters (also defined in *Section 2.6.1*) were also used with their default values of $R = 0.005$ and $C = 0.01$. Steps were executed using the stabilisation option, with the default dissipated energy fraction of 2×10^{-4}, as described in *Section 2.6.1*. After running the model, the total strain energy was compared to the energy dissipated by automatic stabilisation. The dissipated energy fraction was decreased and the model re-run until the energy dissipated by automatic stabilisation was a reasonable amount. It was decided that a reasonable amount of stabilisation (which does not significantly impact the mechanical behaviour of a model) is stabilisation energy which is a maximum of 15% at 80mmHg and decreases to below 5% of the total stabilisation energy in the model. The final model was defined to have a dissipated energy fraction of 2×10^{-5} for stabilisation.

3.2.2 Application of Model

The strategy described in *Section 3.2.1* was applied to different geometries. The objective was to investigate the effect of geometric variations on the mechanical behaviour of the structure. In order to create these different models, some modifications had to be made to the model described in *Section 3.2.1*. Six models were analysed: Two different loop geometries (shown in *Figure 3-16*), each with three different wire thicknesses. The even loop geometry has already been described and was used for the original model. Another knitted wire structure design was investigated, comprising of eight loop-pairs around the circumference. Loops in one longitudinal direction were narrower and loops in the opposite direction broader compared to that of the even loop geometry. The wire thicknesses used were 0.05mm, 0.0635mm 0.075mm.

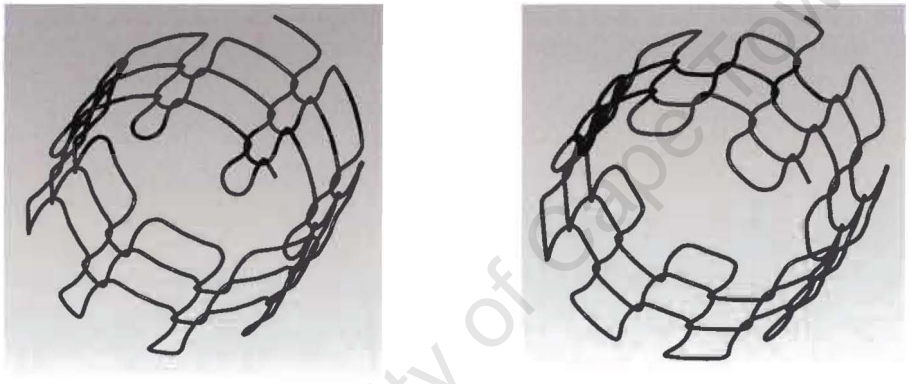

Figure 3-16: Solid geometry of (a) uneven and (b) even loop knitted wire structure.

3.2.2.1 Even Loop Geometry

Two new models were created with the same even loop geometry as the original model (*Section 3.2.1*) but with different wire diameters. The format used to refer to these even loop geometries is: EL(wire diameter in mm), i.e. the original model will be referred to as EL(0.0635). The two new models with wire diameters of 0.05mm and 0.075mm and are referred to as EL(0.05) and EL(0.075) respectively. In *Table 3-2* a summary is given of the parameters differences between the even-loop models. The original model, EL(0.0635), is indicated in bold print in the table

The change in wire diameter leads to a variation in geometry, therefore the single loop centreline geometry used to create EL(0.0635) could not be used for EL(0.05) and EL(0.075). Existing single loop centreline geometries were imported into ProEngineer.

This single loop was then extruded with the respective wire diameter and imported into ABAQUS.

The new models were created as described in *Section 3.2.1*. The three even loop models had different wire thicknesses, but were all meshed with the same number of elements through the wire thickness. Due to the wire thicknesses variation, each model contained different element sizes. The thickest wire (with the largest elements) would have fewer elements in the longitudinal direction than the thinner wires. The total number of nodes and elements in each model is given in *Table 3-2*.

Since mesh definition is one of the factors influencing the stabilisation energy, it had to be verified, for each model, that the energy dissipated due to automatic stabilisation was less than 15% of the total strain energy at 80mmHg, decreasing to less than 5% at 200mmHg. For EL(0.05) and EL(0.075) and the default dissipated energy fraction value of 2×10^{-4} satisfied the predefined limits (see *Table 3-2*).

Model EL(0.05) terminated soon after reaching a radial displacement corresponding to 80mmHg due to lack of convergence. It was re-run with increased softened contact to assist convergence. The Pressure-Clearance parameters were changed from (500 000 MPa, 0mm) and (0MPa, 0.005mm) to (500MPa, 0mm) and (0MPa, 0.005mm). It was verified that 500MPa was still significantly higher than the maximum contact pressure experienced in the model during the analysis. This change improved the convergence rate and the model ran to completion. The original model was named EL(0.05)Auto while the new model with improved convergence retained the name EL(0.05) and was the final model for this design.

Table 3-2: Even loop geometry model variation summary.

Models	Dissipated Energy Fraction	Softened Contact Parameters (MPa, mm)	No Nodes	No Elements
EL(0.05)	2×10^{-4}	(500 , 0) (0, 0.0005)	68373	53648
EL(0.0635)	2×10^{-5}	(500 000, 0) (0, 0.0005)	59640	47444
EL(0.075)	2×10^{-4}	(500 000, 0) (0, 0.0005)	44889	34752

3.2.2.2 Uneven Loop Geometry

One narrow single loop section was used to create the assembly and is shown in *Figure 3-17*.

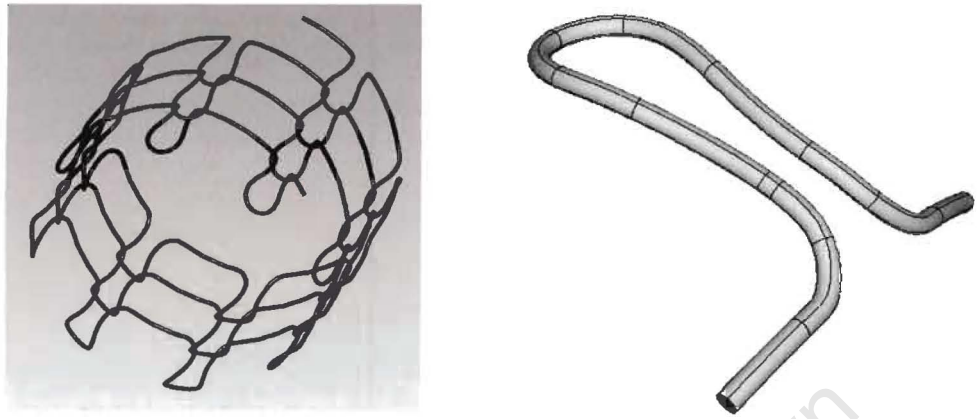

Figure 3-17: Single narrow loop for uneven loop geometry.

A broad single loop section was also modelled to verify that the geometric simplification is an acceptable approximation of the geometry and is described in the verification section.

Three models were created for this geometry with three different wire diameters: UL(0.05) (wire diameter of 0.05mm), UL(0.0635) (wire diameter of 0.0635mm) and UL(0.075) (wire diameter of 0.075mm). They were all created in the same way as EL(0.0635) (described in *Section 3.2.1*). Some variation in parameters was however necessary and are described in this section.

Three different centreline single loop geometries (one for each of the three models) were imported into ProEngineer, extruded to the correct wire diameter and then imported into ABAQUS/CAE. All three models were originally created and run with default value for the dissipated stabilisation fraction (2×10^{-4}). Models had similar mesh definitions to the even loop models and the total number of nodes and elements in each of the three models is given in *Table 3-3*.

The three final models, UL(0.05), UL(0.0635) and UL(0.075), were run with dissipated stabilisation fractions of 2×10^{-4}, 2×10^{-4} and 2×10^{-5} respectively, after confirming that the energy dissipated by automatic stabilisation was below the predefined limits. The first model for UL(0.075), which was run with the default stabilisation value 2×10^{-4}

was renamed UL(0.075)Auto. The difference between the final models are summarised in *Table 3-3.*

Table 3-3: Uneven loop geometry model variation summary.

Models	Dissipated Energy Fraction	Nr Nodes	Nr Elements
UL(0.05)	2×10^{-4}	63305	49408
UL(0.0635)	2×10^{-4}	53045	41296
UL(0.075)	2×10^{-5}	45383	35280

3.2.3 Post Processing Procedures

For each loop design, a graph of the dissipated energy as a fraction of total strain energy was drawn with respect to the equivalent luminal pressure. Graphs of the radial displacement (as a percentage of the initial diameter) were also plotted. Other output variables are the diametric compliance, maximum principal stress and maximum principal strain.

In order to calculate the diametric compliance of the various models, the reaction force of the loop assembly onto the expander surface was recorded during the numerical analysis. The corresponding luminal pressure was then calculated by using a formula dependent on both the effective reaction force and expander radius (dependent on time).

The expander surface was represented by a reference point at the longitudinal centre of the expander's radially central axis and the effective reaction force on this reference point was recorded and can then be given by

$$F_{eff} = (F_x^2 + F_y^2)^{1/2}. \tag{3.1}$$

The z-component (longitudinal component) is not included as it will be zero due to symmetry. One longitudinal half of the expander is shown in *Figure 3-18* together with the reference point representing it.

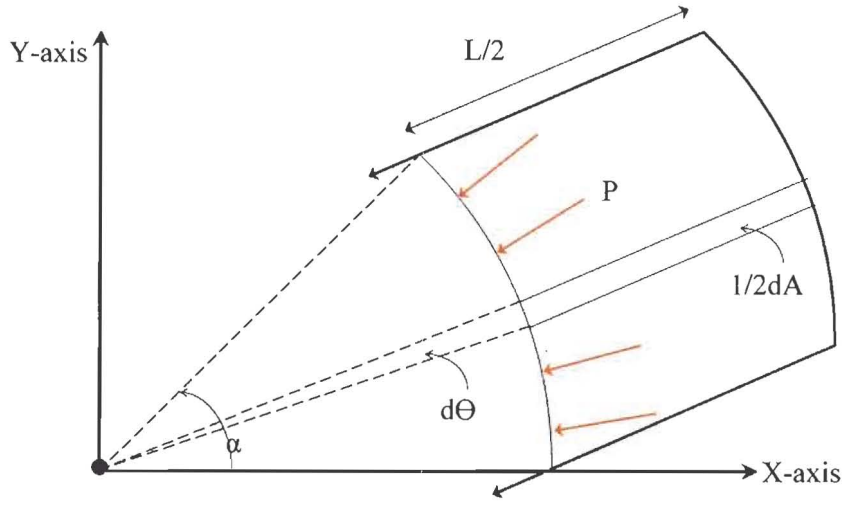

Figure 3-18: An illustration of longitudinal half of the expander surface.

F_x and F_y (*Figure 3-18*) can be written as

$$F_y = -\int_0^{\alpha} P\sin\theta dA \qquad F_x = -\int_0^{\alpha} P\cos\theta dA$$

$$= -\int_0^{\alpha} PLR\sin\theta d\theta \quad \text{and} \quad = -\int_0^{\alpha} PLR\cos\theta d\theta$$

$$= PLR[\cos\theta]_0^{\alpha} \qquad = -PLR[\sin\theta]_0^{\alpha}$$

$$F_y = PLR(\cos\alpha - 1) \qquad (3.2) \qquad F_x = -PLR\sin\alpha\,. \qquad (3.3)$$

Then equation (3.1) can be written as

$$F_{eff} = PLR(\sin^2\alpha + (\cos\alpha - 1)^2)^{1/2}$$
$$= PLR\sqrt{\sin^2\alpha + \cos^2\alpha + 1 - 2\cos\alpha}$$
$$= PLR\sqrt{2 - 2\cos\alpha}$$

and luminal pressure can be calculated from

$$P = \frac{F_{eff}}{LR\sqrt{2 - 2\cos\alpha}} \qquad (3.4)$$

where F_{eff} is the effective reaction force on the reference point, L is the length of the expander surface in longitudinal stent direction , R is the expander radius calculated from the time increment and α is the circumferential section of the expander surface (45^o in

this case). An internal pressure value can be calculated, at each time increment i of the numerical analysis, from the effective reaction force and expander radius at that increment, as L and α remains constant with time.

The compliance C_D can be calculated from two pressure-diameter pairs, (P_i, D_i), by

$$C_D = \frac{D_2 - D_1}{(P_2 - P_1)D_1}. \tag{3.5}$$

The maximum principal stress and strain value at every integration point of the model was recorded for each time increment during the analysis. All data pertaining to the partial loops at the longitudinal ends of the loop assembly were disregarded, as these loops function only as boundary conditions. The elements on the boundaries between partitions were also disregarded since results at tie-constrained surfaces can be unreliable. The maximum principal stress and strain value in each model were documented at luminal pressures of 80mmHg and 120mmHg as well as the values over all the time increments up to 200mmHg were also recorded. The positions at which these values occurred were also shown.

3.3 Verification of Finite Element Models

Different models were created to verify various aspects of the final model give acceptable results. Aspects that were verified include the element type, mesh density, boundary conditions, variation in softened contact definition, Nitinol material model and the loop geometry for the uneven loop geometry.

3.3.1 Elements Type Verification

Three verification models were created from model EL(0.0635) by replacing the eight-noded linear brick elements with ten-noded quadratic tetrahedral elements of differing mesh densities. Five different mesh densities were originally created; however in all five models the energy dissipated due to stabilisation was much higher than the predefined limit. Only the three most coarsely meshed models converged once the dissipated energy fraction was decreased. The final three models used in the element type verification were (in order of increasing mesh density): EL(0.0635)Trhr1, EL(0635)Trhr2 and EL(0.0635)Trhr3, with convergence not being achieved with acceptable dissipated

energy percentage for EL(0.0635)Trhr4 and EL(0.0635)Trhr5. Model EL(0.0635)Trhr1 was created to have approximately the same number of nodes as EL(0.0635). EL(0.0635)Trhr3 and EL(0.0635)Trhr5 have respectively approximately double and triple the amount of nodes then EL(0.0635). For each of the five models, a finely meshed section is shown in *Figure 3-19* to aid in the visualisation of the meshes, while a summary of the different models is given in *Table 3-4*. There is not an obvious difference in mesh density visible between adjacent meshes in *Figure 3-19*, but in *Table 3-4* there is a clear difference in the number of nodes present in the model. In these models the elements are ten-noded, and therefore even a small increase in the number of elements has a large increase in node numbers to effect.

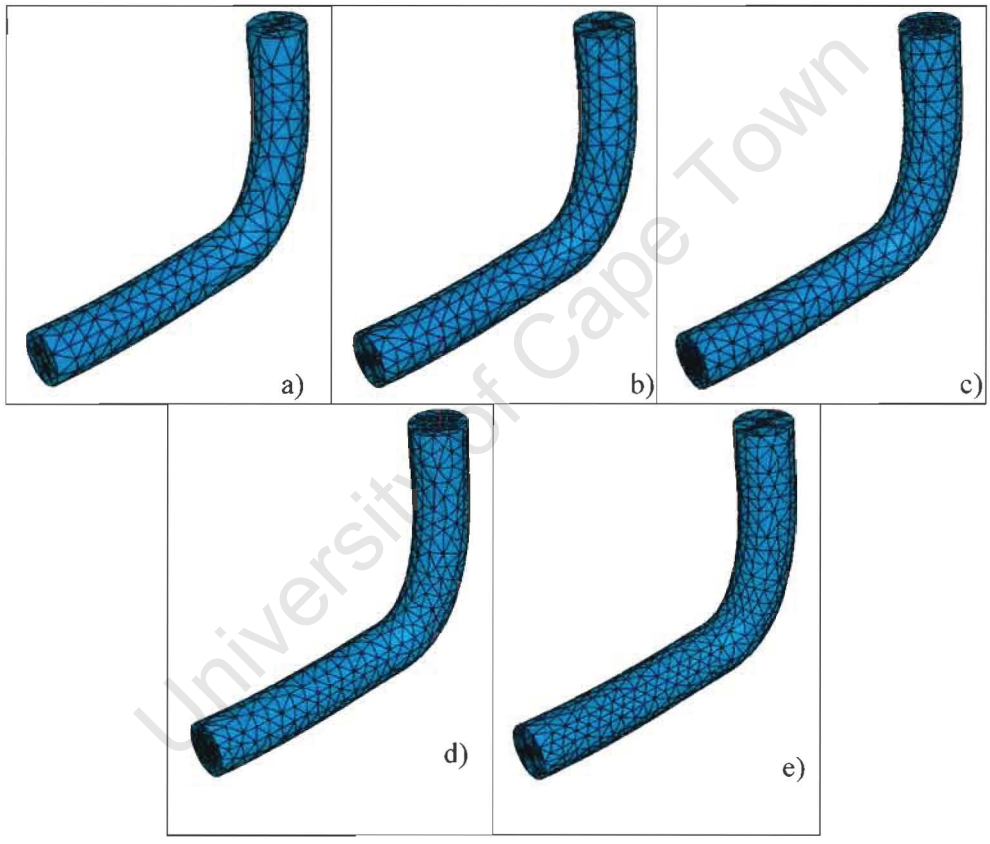

Figure 3-19: Models of increasing mesh refinement (a) EL(0.0635)Trhr1, (b) EL(0.0635)Trhr2, (c) EL(0.0635Trhr3, (d) EL(0.06345)Trhr4 and (e) EL(0.0635)Trhr5.

Table 3-4: Tetrahedral element model variation summary.

Models	Dissipated Energy Fraction	Nr Nodes	Nr Elements
EL(0.0635)Trhr1	2×10^{-6}	52 244	29 992
EL(0.0635)Trhr2	5×10^{-6}	70 388	40 312
EL(0.0635)Trhr3	1×10^{-5}	90 344	53 304
EL(0.0635)Trhr4	No suitable value	105 580	62804
EL(0.0635)Trhr5	No suitable value	134 712	81 288

3.3.2 Mesh Refinement Verification

To verify the sensitivity to mesh density of model EL(0.065), three models were created from model EL(0.0635) by varying the density of the original linear brick element mesh. EL(0.0635)Coarse was meshed more coarsely than EL(0.0635), with approximately one third of the number of nodes. EL(0.0635)Fine2 was assigned a finer mesh than EL(0.0635), with approximately double the amount of nodes and EL(0.0635)Fine3 was assigned an even finer mesh with approximately three times the amount of nodes of EL(0.0635). A sample of the mesh from a finely meshed region is presented in *Figure 3-20* for each of the three models as well as EL(0.0635). It can be seen that the mesh was not only refined along the length of the wire, but also through the wire diameter.

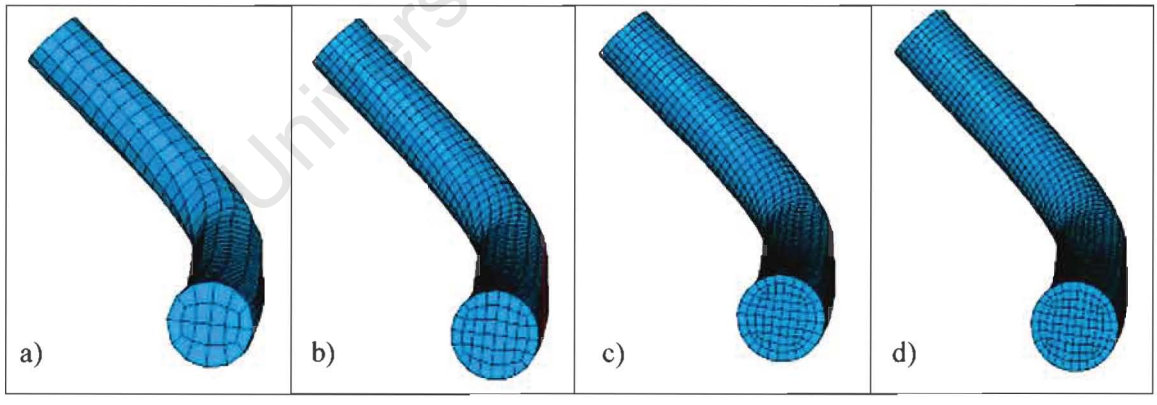

Figure 3-20: Different hexahedral element meshes in (a) EL(0.0635)Coarse (b) EL(0.0635) (c) EL(0.0635)Fine2 and (d) EL(0.0635)Fine3.

The dissipated energy fraction of each model was adjusted until the energy dissipated by automatic stabilisation was within the predefined limits. Other parameters remained as for EL(0.0635). Parameter variations are summarised in *Table 3-5*.

Table 3-5: Mesh refinement model variation summary.

Models	Dissipated energy fraction	Softened Contact Parameters	Nr Nodes	Nr Elements
EL(0.0635)Coarse	1×10^{-5}	(500 000 , 0) (0, 0.0005)	20 568	14 704
EL(0.0635)	2×10^{-5}	(500 000, 0) (0, 0.0005)	59 640	47 444
EL(0.0635)Fine2	1×10^{-4}	(500 000, 0) (0, 0.0005)	123 610	104 536
EL(0.0635)Fine3	2×10^{-4}	(500, 0) (0, 0.0005)	178 004	153 248

Some problems occurred with EL(0.0635)Fine3 terminating due to too low convergence rate shortly after reaching a radial displacement corresponding to 40mmHg. This was rectified by employing the same strategy as used for EL(0.05): modifying the softened contact definition. The dissipated stabilisation energy as percentage of total strain energy was 20% at 80mmHg (5% higher than the predefined value), but decreased to less than 5% at 200mmHg. The value could not be decreased further as a lower dissipated energy fraction lead to premature termination of the model (before 200mmHg) due to lack of convergence. Therefore the model had to be used as is, even though the dissipated stabilisation energy is elevated.

3.3.3 Material Model Verification

Two different sets of material parameters for the material model were implemented to verify the material model used in the wire loop models and four different models are described in this section. It was verified that the final material model input values used resulted in the anticipated stress and strain output predicted by the theory.

Tensile Test Finite Element Model

A tensile test model was created to compare response of the ABAQUS Nitinol material model to stress and strain data expected from theory. The tensile test model was run with the Nitinol material properties determined from the experimental tensile test. Since these values were determined as averages from several tests, the output stress/strain curve could not be directly compared to that of the experimental tensile tests. Instead the tensile test model's stress vs. strain output curve was checked against the expected output curve for the given input material model values. This was done to verify the accuracy of the Nitinol material model that was used throughout this thesis.

The geometry for the tensile test model consisted of a wire (length 10mm) with a circular cross section (diameter 0.0635mm). This geometry was chosen to represent the wire used in the experimental testing. The length, however, was chosen to be 10mm in stead of the experimental 100mm due to computer memory constraints. The results of the 10mm model were compared to a more computationally expensive 50mm model to verify that the length difference between the experimental test and the FEM model did not impact the stress and strain results.

The two boundary conditions and their positions are indicated in *Figure 3-21* showing the geometry of the wire as well as enlarged end section on which the boundary conditions are defined.

- The cross-sectional end surface (1) at one end of the wire was prevented from moving in any direction.
- On the opposite cross-sectional end surface (2), a displacement boundary condition was applied. In the first step a longitudinal displacement (displacement to the right in *Figure 3-21*) of 1,3 mm (7,5mm in the case of the 50mm model), equivalent to 13% strain, was applied to the surface. In the second step the surface returns to its original position. The 13 % strain was chosen since the experimental test showed that the austenite to martensite transformation is complete by the time this strain value is reached.

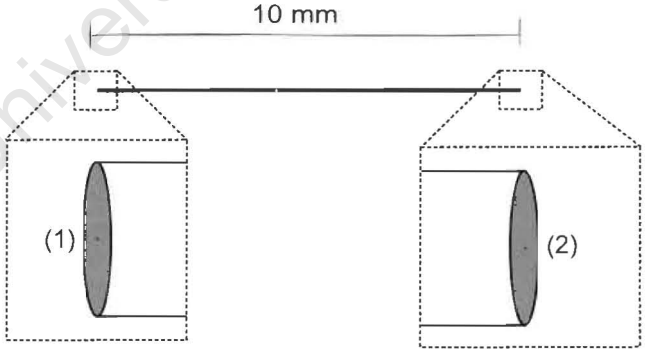

Figure 3-21: The tensile test wire geometry with enlarged sections indicating the positions of the boundary condition.

The wire was meshed with six elements through the thickness in one direction and four through the thickness in the perpendicular direction, the same mesh as the coarsely meshed, straighter sections in model EL(0.0635). The displacement-based analysis was executed in ABAQUS/Standard CAE 6.4-5 in two steps. During the first step,

displacement at surface (2) was linearly increased with time to the maximum value. In the second step the displacement was decreased linearly with respect to time back to the initial position.

Automatic time incrementation was used with minimum and maximum admissible time increment size respectively set to $1x10^{-5}$ and 0.1 and the parameters were used to control the incrementation (defined in *Section 2.6.1*) with their default values $I_G = 4$, $I_L = 10$, $D_D = 1.5$ and $D_B = 0.75$. The convergence parameters (also defined in *Section 2.6.1*) were also used with their default values $R = 0.005$ and $C = 0.01$. The steps were executed using a dissipated energy fraction value of 1×10^{-4}. These models will be referred to as Tensile1_short and Tensile1_long respectively.

Non-Zero Temperature Derivative without Temperature Field

Figure 3-22 shows the one-dimensional transformation process, described in *Section 2.5.4*, as implemented for the material model used in Tensile1 and the wire-loop models. The Stress-Temperature derivatives were defined to be zero. This effectively means that the transformation boundary lines in *Figure 3-22* (where the F values are equal to 0) run parallel to the temperature axis, which means a tensile test will exhibit the same transformation stress values irrespective of the temperature (eg. T_1 or T_2) at which the test occurs.

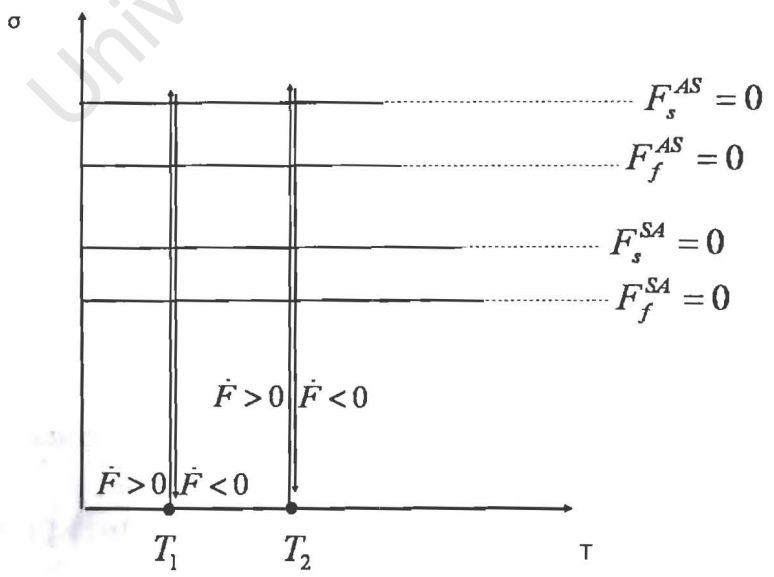

Figure 3-22: One-dimensional SMA transformation process for Tensile1 material model.

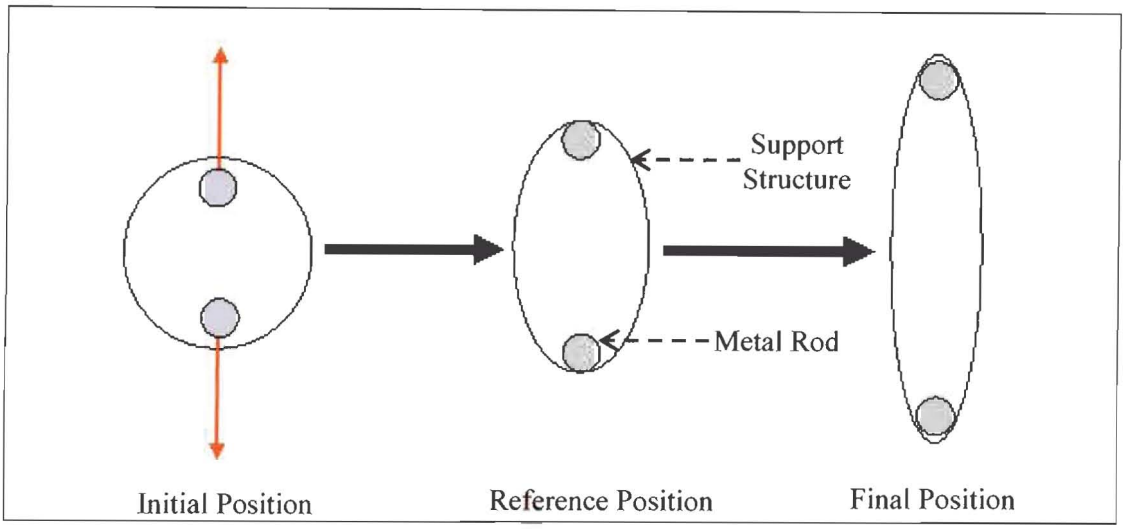

Figure 3-25: Cross-section of the elliptical deformation of a metal support structure during circumferential tensile testing.

Initially the metal rods were displaced until the circular cross-section of the structure was deformed to the longest elliptical shape still comprising the same circumference as the original circular cross section. This position was used as the 0% circumferential strain reference configuration. From extension past the reference position the load and displacement data was captured the compliance of the structure over the pressure range 80mmHg to 120mmHg was calculated. The deformation of the structure in this test differs to that experienced in vivo and to the displacement modelled in the FEM models in this thesis.

Dynatek Dalta conducted volumetric compliance tests and then calculated the diametric compliance from the determined volumetric compliance. The experimental setup included a lumina latex liner and loading was established through varying water pressure inside the liner. The cyclic tests were conducted at room temperature with the water inside the liner at 37°C and with the pressure cycling at a frequency of 72 bpm (1.2 Hz), the standard frequency used in vitro to represent an average heart rate. The Latex liner accounts for some of the compliance of the total structure. Calculations were done and measuring pressures adapted so as to exclude the effect of the latex liner on the final compliance of the system. These tests differ from the FEM models in that the inner liner used in loading is deformable and that the procedure is cyclic.

Medtronic MBC also conducted compliance tests with latex liner and water pressure, but did not correct for the effect of the liner. Compliance was determined by measuring the outer diameter by means of a laser micrometer. Tests were conducted at room

temperature at a frequency of 72 bpm (1.2 Hz). The tests differ from the FEM model in that the loading surface is deformable, the tests are cyclic and the effect of the liner is not accounted for.

CHAPTER 4: RESULTS

4.1 Nitinol Material Characterisation

Wire samples were tested as described in *Section 3.1*. Not all tested samples produced results, as some wires pulled out of the glue (and the clamp) during the test. Tests of the following samples produced results that could be used: 3 samples from the 0.05mm diameter wires, 2 samples of the 0.0635mm diameter wires, 4 samples of the 0.075mm diameter wire. Nitinol material parameters listed in *Table 4-1*.

Table 4-1: Nitinol material parameters calculated from the experimental tensile test.

Parameter	Abbreviation	Unit	Value
Austenite Elasticity	E_A	MPa	38992
Martensite Elasticity	E_M	MPa	21910
Transformation Strain	ε^L	-	0.042
Loading Start of Transformation Stress	σ_L^S	MPa	483
Loading End of Transformation Stress	σ_L^E	MPa	610
Unloading Start of Transformation Stress	σ_U^S	MPa	388
Unloading End of Transformation Stress	σ_U^E	MPa	256

Other input parameters could not be determined from the tensile tests conducted and were therefore used as supplied by Medtronic Vascular, Galway, Ireland.

4.2 Finite Element Analysis Results

The luminal pressure values were calculated using the reaction force of the wire structure on the expander surface (measured at the reference point) and the expander radius (which increases linearly with time) as described in *Section 3.2.3*. The FEM analysis was conducted incrementally over time with time increments automatically controlled to ensure fastest possible convergence. For this reason the pressure increments are not always equal in size and the exact equivalent pressure at an increment could not be explicitly controlled. Increments with pressure values as close as possible to the desired pressure are used in the analyses, as results are compared at physiological pressure values (80mmHg, 120mmHg, 200mmHg).

4.2.1 Stabilisation and Strain Energy

For each model, the energy dissipated due to stabilisation was calculated as a percentage of the total strain energy. In *Figure 4-1* curves for the dissipated stabilisation energy (% of strain energy) was plotted vs. luminal pressure for the even loop geometry models EL(0.0635)Auto, EL(0.0635), EL(0.05) and EL(0.075). In *Figure 4-2* curves are plotted for the uneven loop geometry UL(0.0635), UL(0.05), UL(0.075)Auto and UL(0.075). Limits for the stabilisation energy percentage were discussed in *Section 3.2.1.7*. This same analysis procedure was followed for subsequent stabilisation analysis sections.

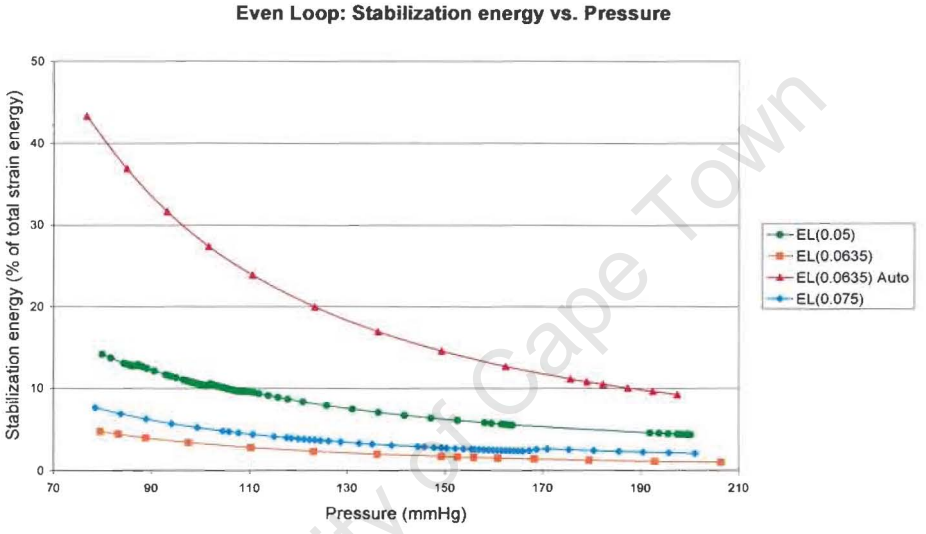

Figure 4-1: Energy dissipated by stabilisation plotted for the even loop models.

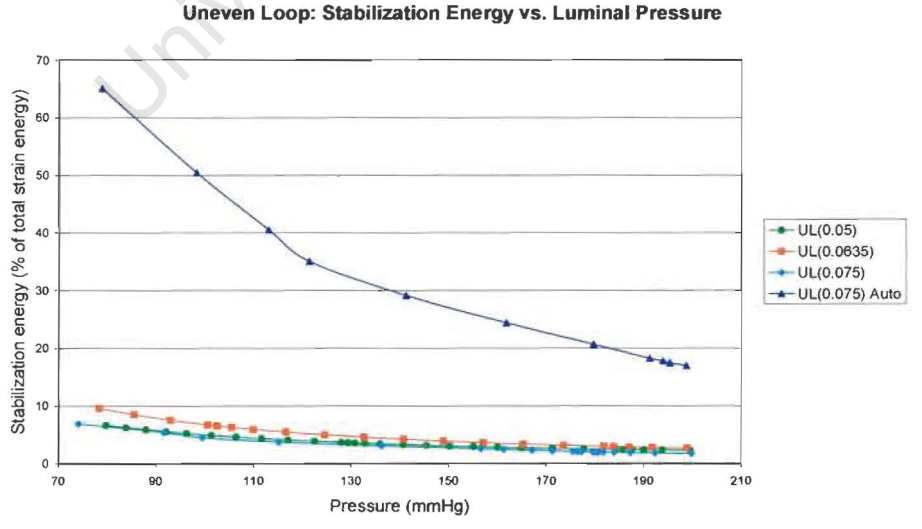

Figure 4-2: Energy dissipated by stabilisation plotted for the uneven loop models.

For EL(0.0635)Auto (in *Figure 4-1*) the stabilisation energy is much higher than the proposed limit when the default value for dissipated energy fraction is used. The stabilisation energy curve decreases from more than 40% at 80mmHg to just lower than 10% at 200mmHg. For the three final even loop models these values lie within the proposed limits. For UL(0.075)Auto (in *Figure 4-2*) the stabilisation energy is also much higher than the proposed limits when the default value for dissipated energy fraction is used. The stabilisation curve decreases from more than 60% at 80mmHg to just below 20% at 200mmHg. For the three final uneven loop models, as with the even loop models, the stabilisation values fall within the proposed range.

4.2.2 Radial Deformation

In *Figure 4-3* and *Figure 4-4* graphs were plotted of luminal pressure (mmHg) vs. internal diameter increase (% change from initial diameter at 0mmHg) for the even and uneven loop models respectively. Although expansion of the metal structure is dependent on the luminal pressure increase, it is generally accepted in the medical field that pressure is plotted on the y-axis for compliance graphs. A percentage was used rather than an absolute diameter value to allow comparison between different models starting from slightly different initial diameters. Values are plotted from 0mmHg to approximately 200mmHg to cover the physiological range and separate graphs were plotted for the even and uneven loop geometry.

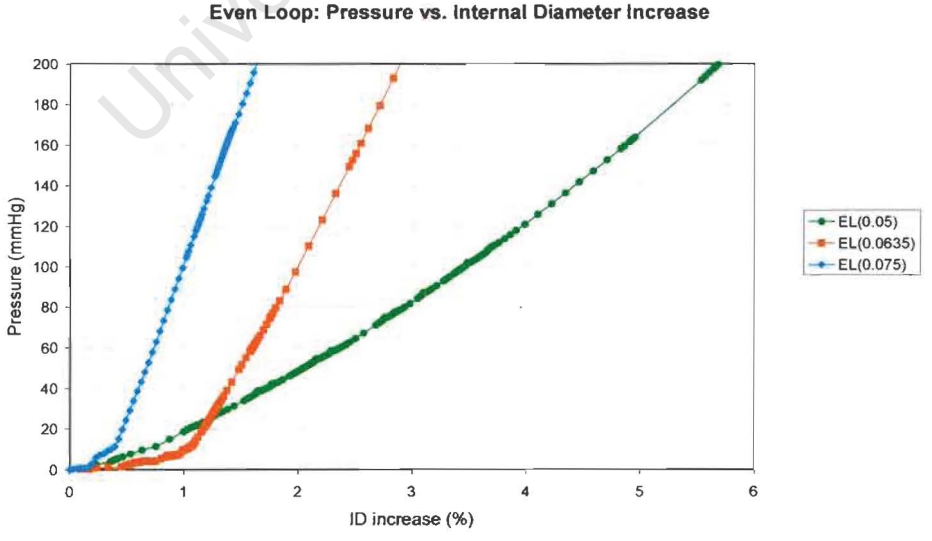

Figure 4-3: Graph of Luminal Pressure (mmHg) vs. Internal Diameter Increase (%) for the even loop models.

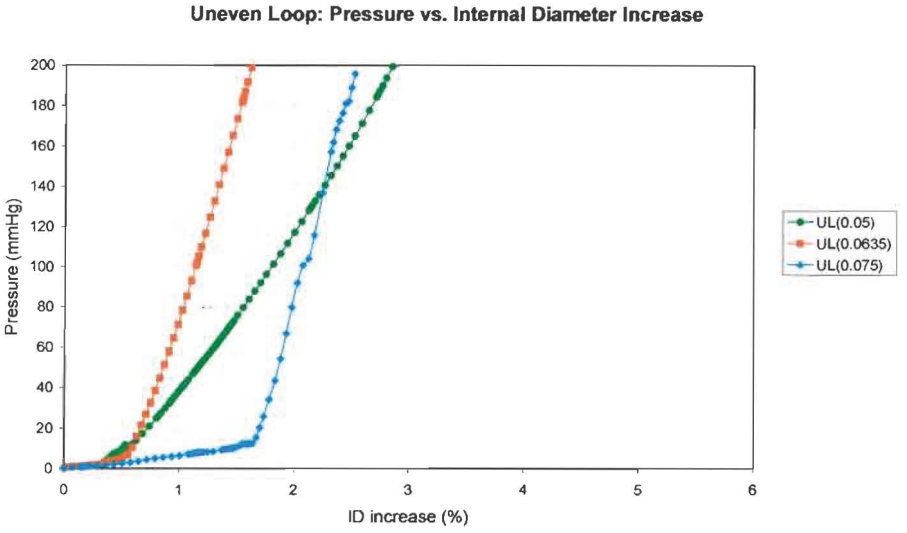

Figure 4-4: Graph of Luminal Pressure (mmHg) vs. Internal Diameter increase (%) for the uneven loop models.

The even loop model have of the thinnest wire produced a curve with smoother diameter increase, while the curves for the two thicker wires exhibits a distinct change in the gradient at around 10mmHg. In further descriptions, these will be referred to as the initial and final gradients for the gradients at low and high pressure respectively. The region of the final gradient show the rate of diameter increase decreasing with increasing wire thickness. In the uneven geometry (*Figure 4-4*) a similar trend is followed for the 0.0635mm and 0.05mm diameter models. The absolute diameter increase is however considerably less (almost half) than that of the even loop geometry models. The final gradients also follow the same trend as even loop models, with the gradient increasing with increasing wire thickness. The absolute deformation in UL(0.075) however differs from the trend observed in the even loop geometry. Its total radial deformation is more than that of the smaller diameter wires. Its larger final diameter is due to the final gradient only being reached at a higher diameter increase, even though the final gradient follows the trend observed in the even loop models.

4.2.3 Compliance

Table 4-2 reports the compliance values calculated between the pressure values that lie closest to 80mmHg and 120mmHg, with the exact pressures specified in the table. Compliance values were calculated as described in *Section 3.2.3* in % per 100 mmHg.

Table 4-2: Compliance values for uneven and even loop models.

Model	Compliance (%/100 mmHg)	Pressure Range (mmHg)	
		Minimum	Maximum
EL(0.05)	2.51	80	121
EL(0.0635)	0.92	80	123
EL(0.075)	0.63	79	120
UL(0.05)	1.17	80	123
UL(0.0635)	0.52	78	117
UL(0.075)	0.51	74	115

Compliance increases with decreasing wire thickness in both the uneven and even loop designs. The increase in compliance from 0.0635mm diameter to 0.05mm diameter models is much more pronounced than the compliance increase from 0.075mm to 0.0635mm diameter models. The even loop models show significantly higher compliances and greater compliance variation with wire diameter than the uneven loop geometry.

4.2.4 Maximum Principal Stress

The stress distributions in the even and uneven loop geometries are illustrated in *Figure 4-5* and *Figure 4-6* respectively for EL(0.0635) and UL(0.0635). The maximum principal stress for each of the six models is recorded in *Table 4-3* at pressures closest to 80mmHg, 120mmHg and 200mmHg. Distributions for other wire thicknesses are similar. The maximum stress positions are circled in black.

Table 4-3: Maximum principal stresses at 80mmHg, 120mmHg and 200 mmHg for even and uneven loop models.

Model	80 mmHg		120 mmHg		200 mmHg	
	P (mmHg)	Stress (MPa)	P (mmHg)	Stress (MPa)	P (mmHg)	Stress (MPa)
EL(0.05)	80	177.2	121	268.3	200	420.5
EL(0.0635)	80	87.0	123	131.9	206	218.3
EL(0.075)	79	58.0	120	91.0	201	144.3
UL(0.05)	80	116.0	123	174.9	200	283.4
UL(0.0635)	78	62.3	117	83.9	199	146.1
UL(0.075)	74	63.6	115	79.5	200	128.6

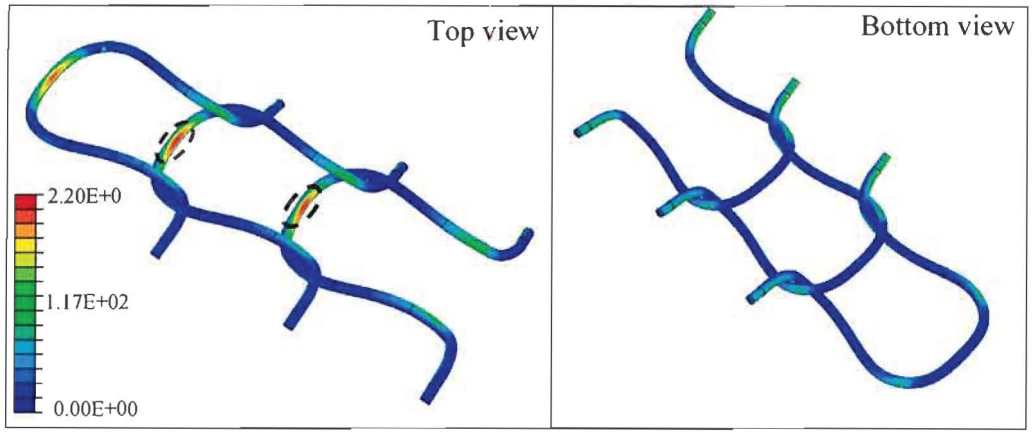

Figure 4-5: Stress distribution for even loop geometry with positions of maximum stress indicated.

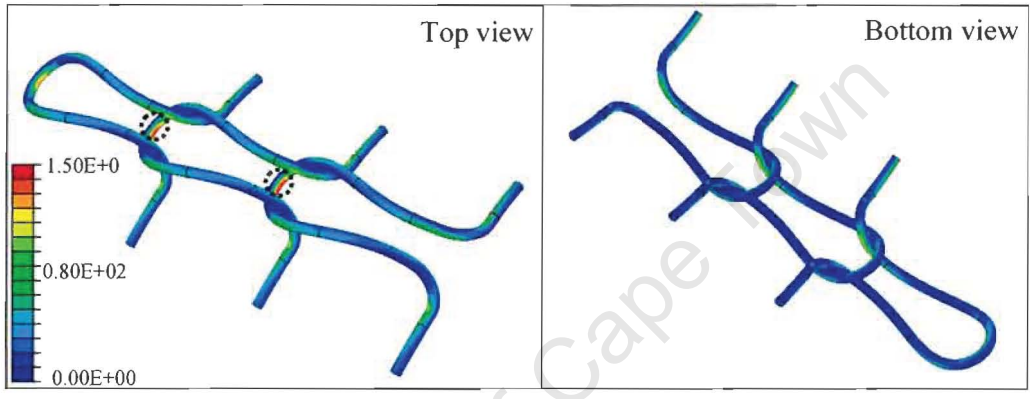

Figure 4-6: Stress distribution for uneven loop geometry with positions of maximum stress indicated.

Both the uneven and even loop geometry display a similar trend in maximum principal stress: the models of thinnest wire diameter experiences the highest stress and stress values increase with both decreasing wire thickness and increasing luminal pressure. In the uneven and even loop geometry the maximum principal stress values for the 0.05mm wire models are significantly higher than for the other two thicknesses (about double that of the 0.0635mm wire model). In some cases the overall observed trends are not followed. UL(0.0635) displays a lower maximum principal stress than UL(0.075) at 80mmHg. The two values are very close to each other and by the time the luminal pressure reaches 120mmHg the values follow the overall observed trend. The even loop geometry displays higher values for all the thicknesses and pressures, except in the case of the thickest wire (0.075mm) at 80mmHg, where the uneven loop model has a higher value.

4.2.5 Maximum Principal Strain

In *Table 4-4* the maximum principal strain at the pressures closest to 80mmHg, 120mmHg and 200mmHg respectively are given for each geometric variation. The strain distributions in the even and uneven loop geometries are given *Figure 4-7* and *Figure 4-8* respectively. The distributions are for EL(0.0635) and UL(0.0635) as distributions for the other wire thicknesses are similar. The areas where maximum strain occurs are circled in black.

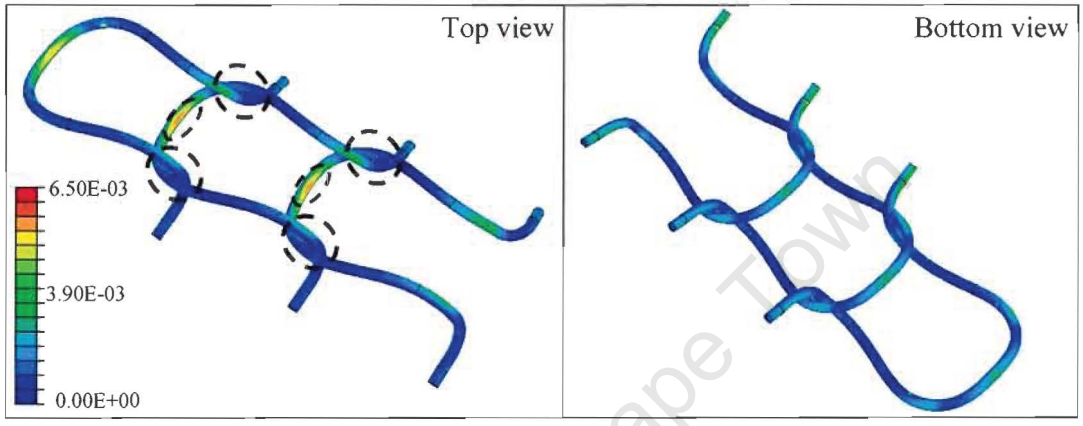

Figure 4-7: Strain distribution in even loop geometry with positions of maximum strain indicated.

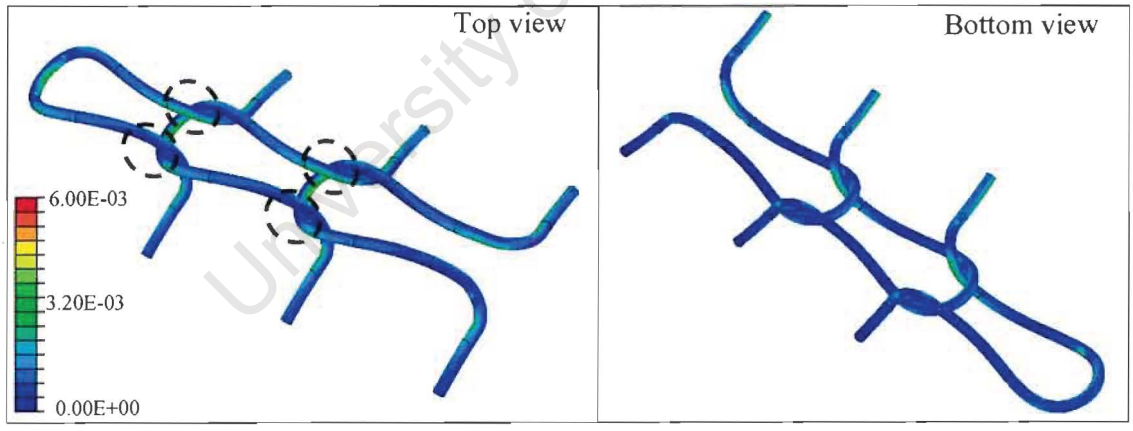

Figure 4-8: Strain distribution in uneven loop geometry with positions of maximum strain indicated.

Table 4-4: Maximum principal strain at 80, 120 and 200 mmHg for the even and uneven loop models.

Model	80 mmHg		120 mmHg		200 mmHg	
	P(mmHg)	Strain (%)	P(mmHg)	Strain (%)	P(mmHg)	Strain (%)
EL(0.05)	80	0.46	121	0.70	200	1.10
EL(0.0635)	80	0.32	123	0.43	206	0.66
EL(0.075)	79	0.24	120	0.39	201	0.67
UL(0.05)	80	0.37	123	0.71	200	1.15
UL(0.0635)	78	0.34	117	0.41	199	0.59
UL(0.075)	74	0.24	115	0.32	200	0.81

Both the uneven and even loop geometry displayed a similar trend in maximum principal strain. The thinnest wire thickness experiences the highest strain with the strain values decreasing with increasing wire thickness. At 200mmHg, the 0.0635mm diameter models however display a lower maximum principal strain than the 0.075mm diameter models. The difference between the strain in the thinnest wire and that in the other two wire thicknesses becomes more pronounced with increasing pressure. This differs from the situation for maximum principal stress where the thinnest wire model already experiences a significantly higher stress from 80mmHg. The strain values also differ from the stress values in that strain values for the uneven and even loop models are much more similar than their stress values.

4.3 Results for Verification of Finite Element Models

The same parameters analysed for the main FEM models were analysed for verification models. Each model was analysed according to stabilisation, deformation, compliance, maximum principal stress and maximum principal strain.

4.3.1 Element Type Verification

Stabilisation and Strain energy

Dissipated energy (% of strain energy) is plotted vs. luminal pressure (mmHg) in *Figure 4-9*. Curves for EL(0.0635), EL(0.0635)Trhr1, EL(0.0635)Trhr2 and EL(0.0635)Trhr3 are shown, where EL(0.0635) is the original model being verified.

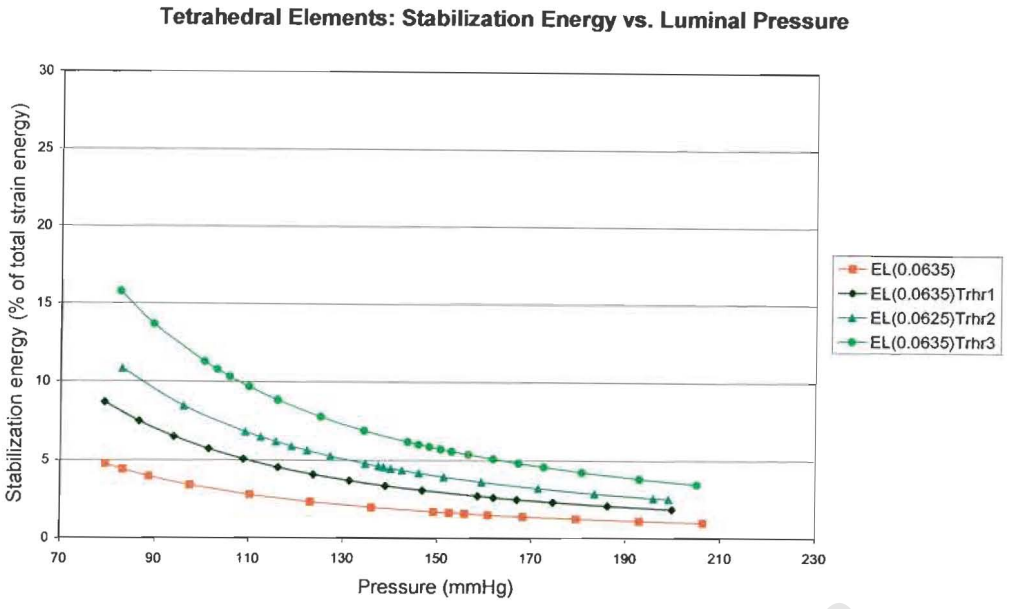

Figure 4-9: Energy dissipated through stabilisation vs. luminal pressure, plotted for different mesh refinements with tetrahedral elements as well as EL(0.0635).

Although the curve for EL(0.065)Trhr3 starts slightly above 15%, it decreases to below 5% by 200mmHg. The initial value falls slightly outside the predefined limit, but the dissipated energy fraction parameter could not be decreased further without encountering convergence difficulties. Stabilisation energy for the other models falls within the predefined limits. The stabilisation energy increased with increasing mesh refinement and all the tetrahedral element models had higher stabilisation energy values than EL(0.0635).

Radial Deformation

In *Figure 4-10* a graph is plotted of luminal pressure (mmHg) vs. internal diameter increase (% change from initial diameter at 0mmHg) for the tetrahedral mesh verification models.

The point of distinct gradient change occurs at a slightly larger ID increase for the tetrahedral models than for EL(0.0635). Other than that the curves are similar. All three of tetrahedral models exhibit the same displacement curves.

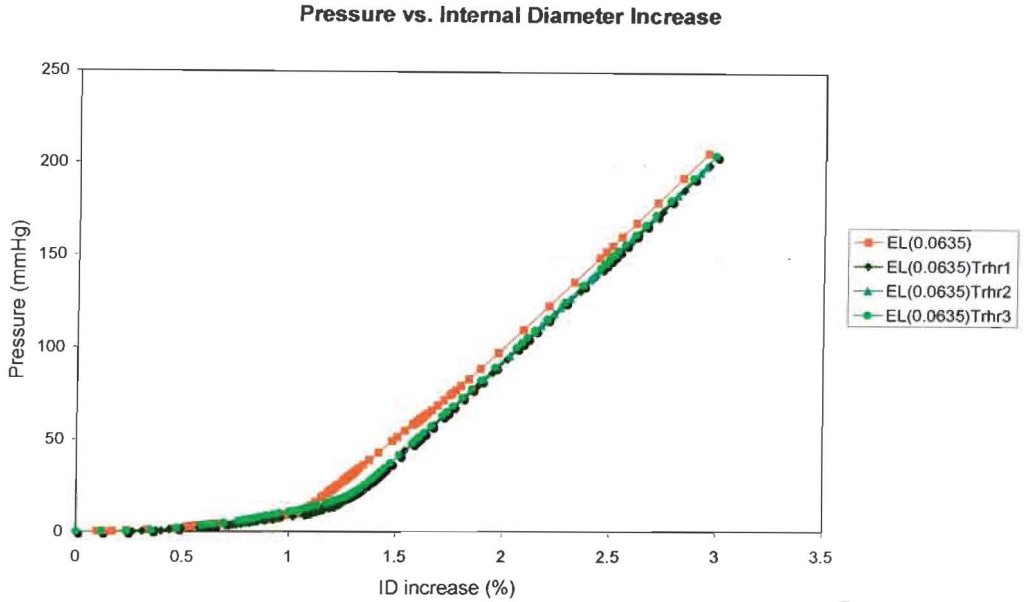

Figure 4-10: Graph of Luminal Pressure (mmHg) vs. Internal Diameter (%) for the tetrahedral mesh models as well as EL(0.0635).

Compliance

The compliance values as well as the pressure ranges over which they were calculated are given in *Table 4-5*.

Table 4-5: Compliance values over for tetrahedral models and EL(0.0635).

Model	Compliance (%/100 mmHg)	Pressure Range (mmHg)	
		Minimum	Maximum
EL(0.00635)	0.921	80	123
EL(0.0635)Trhr1	0.906	79	124
EL(0.0635)Trhr2	0.879	82	122
EL(0.0635)Trhr3	0.893	82	125

The compliance of the tetrahedral models is only slightly lower than that of EL(0.0635). There does not appear to be trend in the compliance variation with mesh refinement and all three compliance values are approximately the same.

Maximum Principal Stress

The maximum principal stresses in the models were recorded at pressures close to 80mmHg, 120mmHg and 200mmHg respectively in Table 4-6. The stress distributions for the hexahedral and tetrahedral models are shown in *Figure 4-11* and *Figure 4-12* respectively.

Table 4-6: Maximum principal stresses at 80, 120 and 200 mmHg for the tetrahedral element models and EL(0.0635).

Model	80 mmHg		120 mmHg		200 mmHg	
	P (mmHg)	Stress (MPa)	P (mmHg)	Stress (MPa)	P (mmHg)	Stress (MPa)
EL(0.0635)	80	87.0	123	131.9	206	218.3
EL(0.0635)Trhr1	79	96.1	124	143.7	200	224.0
EL(0.0635)Trhr2	83	100.1	122	144.0	199	227.2
EL(0.0635)Trhr3	82	101.3	125	148.3	205	238.1

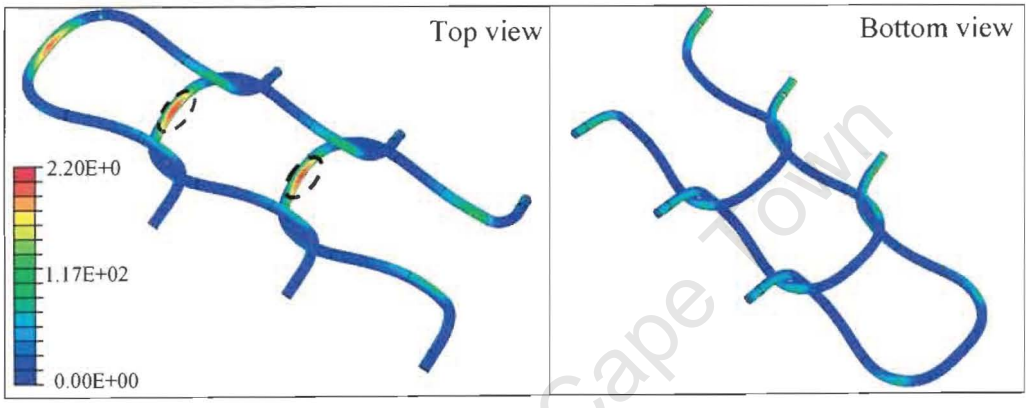

Figure 4-11: Stress distribution of the original even-loop geometry, EL(0.0635), with positions of maximum strain indicated.

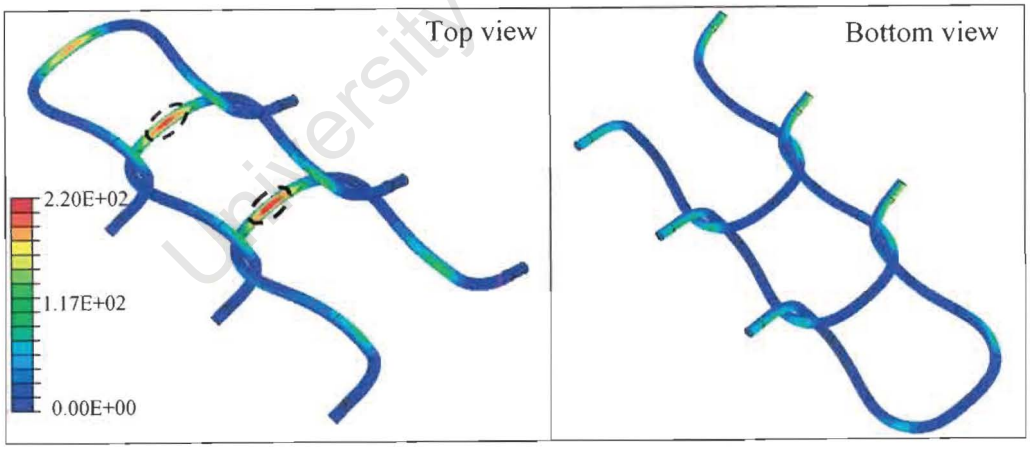

Figure 4-12: Stress distribution for tetrahedral meshed even loop geometry, EL(0.0635)Trhr2, with positions of maximum strain indicated.

The maximum principal stress values for the tetrahedral element models are slightly higher than that of EL(0.0635) at all three pressure values. The stress values also appear to increase with increasing mesh refinement of the tetrahedral elements and increasing

luminal pressure. The positions of maximum principal stress is the same as for EL(0.0635). The stress distribution is also similar to EL(0.0635).

Maximum Principal Strain

The maximum principal strains in the two models are recorded at pressures close to 80mmHg, 120mmHg and 200mmHg *Table 4-7*. The strain distributions are shown in *Figure 4-13* and *Figure 4-14* respectively.

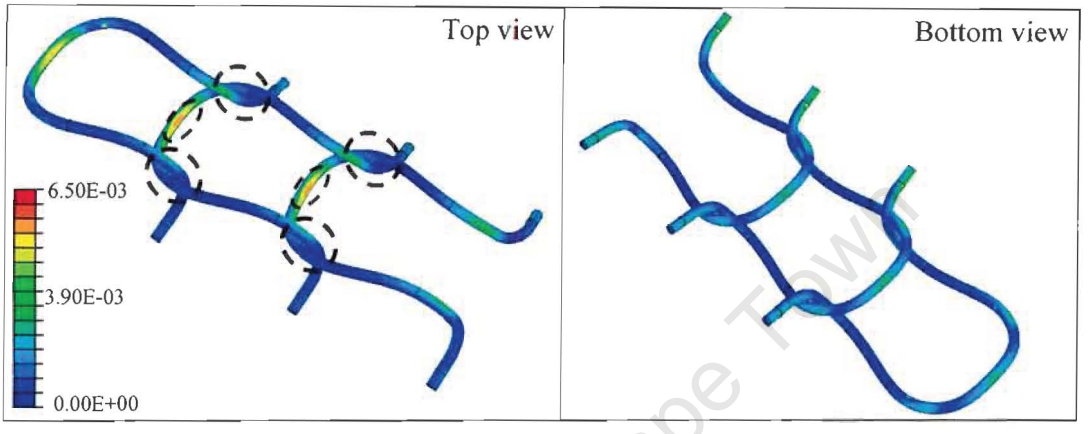

Figure 4-13: Strain distribution for original even-loop geometry, EL(0.0635), with positions of maximum strain indicated.

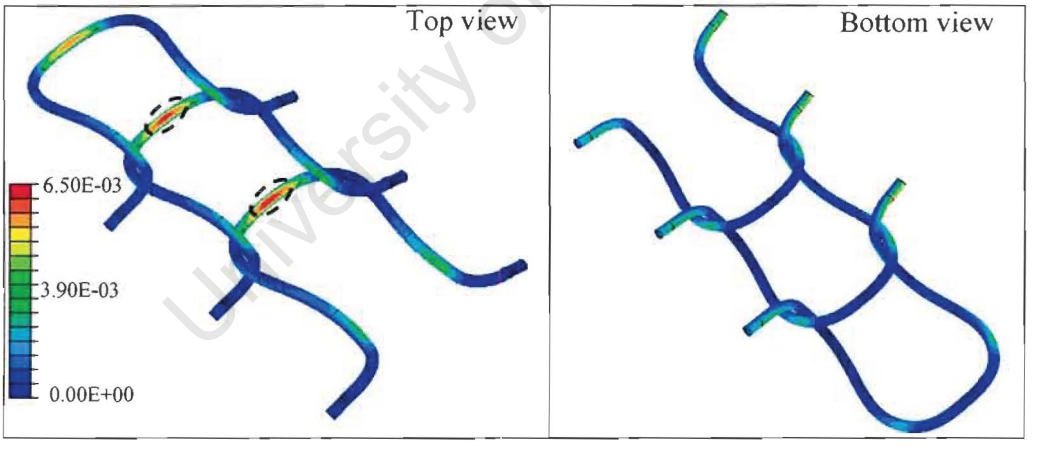

Figure 4-14: Strain distribution in tetrahedral element meshed even-loop geometry, EL(0.0635)Trhr2, with positions of maximum strain indicated.

Table 4-7: Maximum principal stresses at 80, 120 and 200 mmHg.

Model	80 mmHg		120 mmHg		200 mmHg	
	P (mmHg)	Strain (MPa)	P (mmHg)	Strain (MPa)	P (mmHg)	Strain (MPa)
EL(0.0635)	80	0.32	123	0.43	206	0.66
EL(0.0635)Trhr1	79	0.24	124	0.37	200	0.57
EL(0.0635)Trhr2	83	0.25	122	0.35	199	0.56
EL(0.0635)Trhr3	82	0.25	125	0.36	205	0.58

The maximum principal strain in the tetrahedral element models is slightly lower than that of EL(0.0635). There does not appear to be a trend with respect to mesh refinement. The positions of the maximum principal strains are in the centre of the loops, not at the contacts positions observed in the previous hexahedral element models. Maximum principal strain increases with increasing luminal pressure. The strain distribution is also similar to EL(0.0635), but the maximum values only occur in one of the position seen in EL(0.0635).

4.3.2 Mesh Density Verification

Stabilisation and Strain Energy

In *Figure 4-15* dissipated energy is plotted vs. luminal pressure for models with different mesh densities.

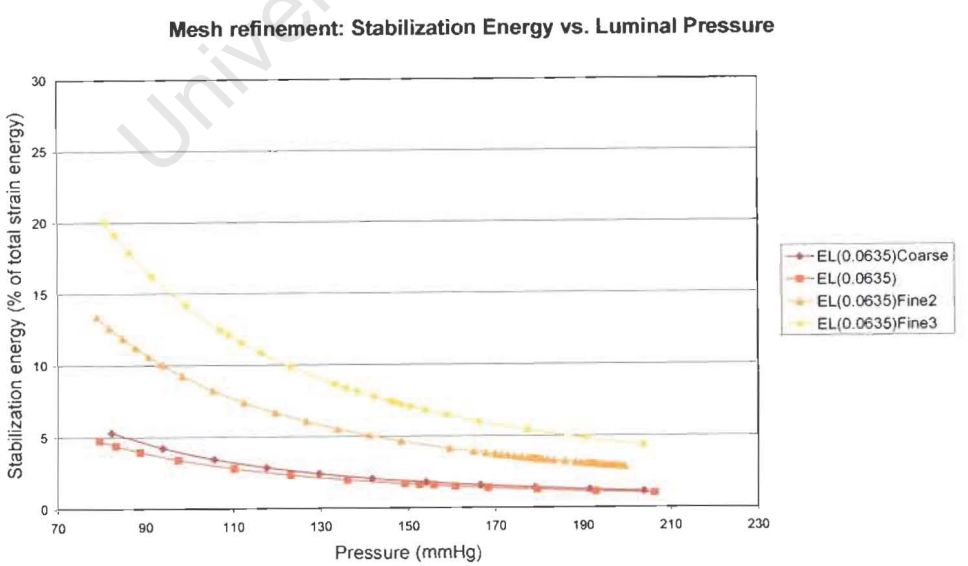

Figure 4-15: Energy dissipated through stabilisation vs. luminal pressure, plotted for different hexahedral element mesh models.

As mentioned in *Section 3.3.2*, EL(0.0635)Fine3 has approximately 20% stabilisation energy a 80mmHg, but decrease to below 5% by 200mmHg. Although this 20% falls outside the predefined limits, the dissipated energy fraction parameter could not be decreased further without encountering convergence difficulties. Stabilisation energy for the other three models falls within the predefined limits. The stabilisation energy increases with increasing mesh density although EL(0.0635)Coarse does not appear to follow this trend.

Radial Deformation

In *Figure 4-16* luminal pressure (mmHg) is plotted vs. internal diameter change (% change from initial diameter) for the mesh verification models as well as the original model, EL(0.0635).

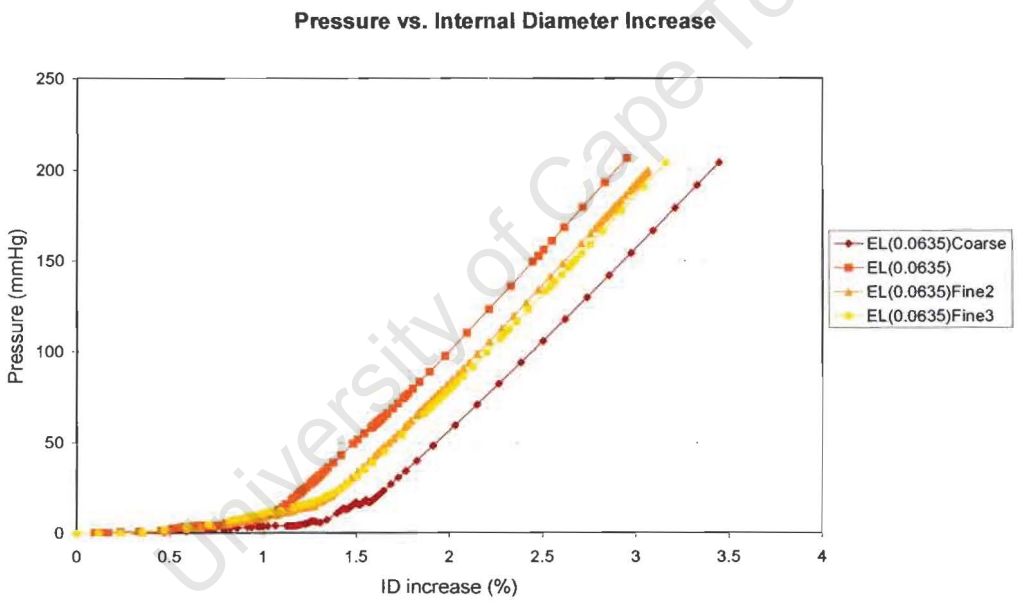

Figure 4-16: Graph of Luminal Pressure (mmHg) vs. Internal Diameter (%) for the hexahedral element mesh models.

The point of distinct gradient change shifts depending on the mesh refinement. The more refined the mesh, the further the ID increases before the gradient change occurs. EL(0.0635)Coarse again does not follow this trend and increases even further than EL(0.0635)Fine3 before the gradient changes. A difference in final gradient can not be observed by simply looking at the curves, this indicates very similar compliance values for the different models. This change is however very small. Again EL(0.0635)Coarse

does not follow the trend observed in the other three models, having an gradient is even less steep than that of EL(0.0635)Fine3.

Compliance

The compliance values as well as the pressure ranges over which they were calculated are given in *Table 4-8*.

Table 4-8: Compliance values for the hexahedral element mesh models.

Model	Compliance (%/100 mmHg)	Pressure Range (mmHg)	
		Minimum	Maximum
EL(0.0635)Coarse	0.98	82	118
EL(0.0635)	0.92	80	123
EL(0.0635)Fine2	0.94	79	120
EL(0.075)Fine3	0.94	81	123

The compliance values decrease with increasing mesh density. EL(0.0635)Coarse however does not follow this trend with a compliance even higher than that of EL(0.0635)Fine3.

Maximum Principal Stress

The maximum principal stresses in the models are recorded at pressures close to 80mmHg, 120mmHg and 200mmHg in *Table 4-9*.

Table 4-9: Maximum principal stresses at 80, 120 and 200 mmHg for the hexahedral element mesh models.

Model	80 mmHg		120 mmHg		200 mmHg	
	P (mmHg)	Stress (MPa)	P (mmHg)	Stress (MPa)	P (mmHg)	Stress (MPa)
EL(0.0635)Coarse	82	98.5	118	135.0	203	244.1
EL(0.0635)	80	87.0	123	131.9	206	218.3
EL(0.0635) Fine2	80	89.2	120	129.8	200	210.0
EL(0.075)Fine3	81	91.5	123	136.8	204	220.7

The maximum principal stress values for EL(0.0635) and EL(0.0635)Fine2 are similar, while values for EL(0.06.35) Fine3 is slightly higher. EL(0.0635)Coarse has higher values than both EL(0.0635) and EL(0.0635)Fine2.

Maximum Principal Strain

The maximum principal strains in the models are recorded at pressures close to 80 mmHg, 120 mmHg and 200 mmHg respectively in *Table 4-10*.

Table 4-10: Maximum principal strains at 80, 120 and 200 mmHg for the hexahedral element mesh models.

Model	80 mmHg		120 mmHg		200 mmHg	
	P (mmHg)	Strain (%)	P (mmHg)	Strain (%)	P (mmHg)	Strain (%)
EL(0.0635)Coarse	82	0.26	118	0.35	204	0.58
EL(0.0635)	80	0.32	123	0.43	206	0.66
EL(0.0635) Fine2	79	0.31	120	0.45	200	0.87
EL(0.0635)Fine3	81	0.48	123	0.67	204	0.81

The strain increases with increasing refinement as well as with increasing luminal pressure. The strain values of EL(0.0635) and EL(0.0.635)Fine2 are very close to each other while the values for EL(0.0635)Fine3 and EL(0.0635)Coarse slightly higher and lower respectively. This indicates that maximum principal strain increases with increasing mesh density. At 2 00mmHg, EL(0.0635)Fine2 does not follow the trend, having a higher maximum principal strain that EL(0.0635)Fine3.

4.3.3 Material Model Verification

Tensile Test Model

Figure 4-17 shows the stress vs. strain curve for Tensile1_short and Tensilt1_long as described in *Section 3.3.3*. It can been seen in *Figure 4-17* that the stress strain response for models of length 10mm and 50mm models are the exactly the same. It can therefore be inferred that the results for 100mm will also be the same as that of the 10mm models. The material model verification will therefore use models which are 10mm in length. The stress values at the start and end of the transformations correspond to the input values. The shape of the curve also corresponds to the shape of a Nitinol tensile test predicted by the theory.

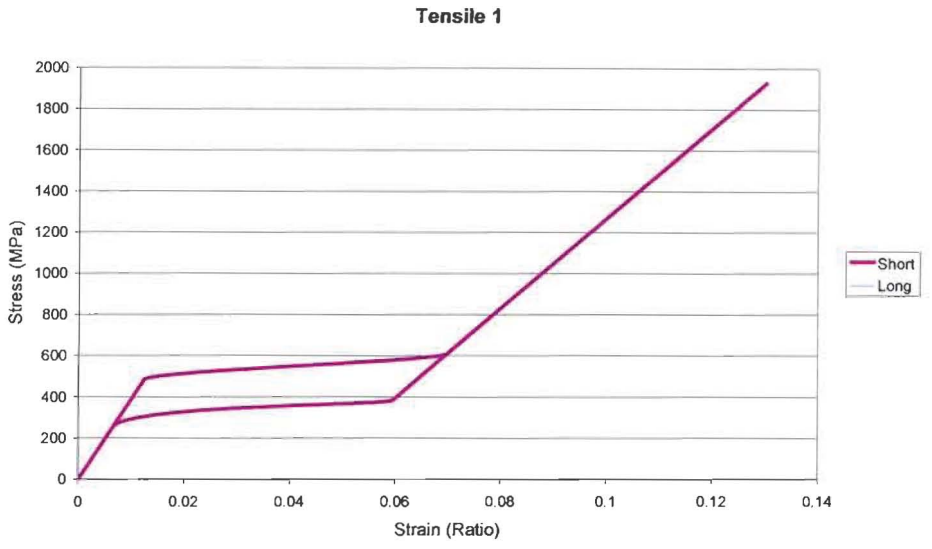

Figure 4-17 The Stress vs. Strain plot for long and short models of Tensile1.

Temperature Derivative without Temperature Field

The transformation stress values were determined by experimental tests conducted at 37°C. These values were seen at the start and end of transformations in model Tensile1. However it is clear from *Figure 4-18* that in model Tensile 2 the transformations started and ended at different values than those entered in the material model. This would be due to the test proceeding at a different temperature than that for which the values were entered (37°C).

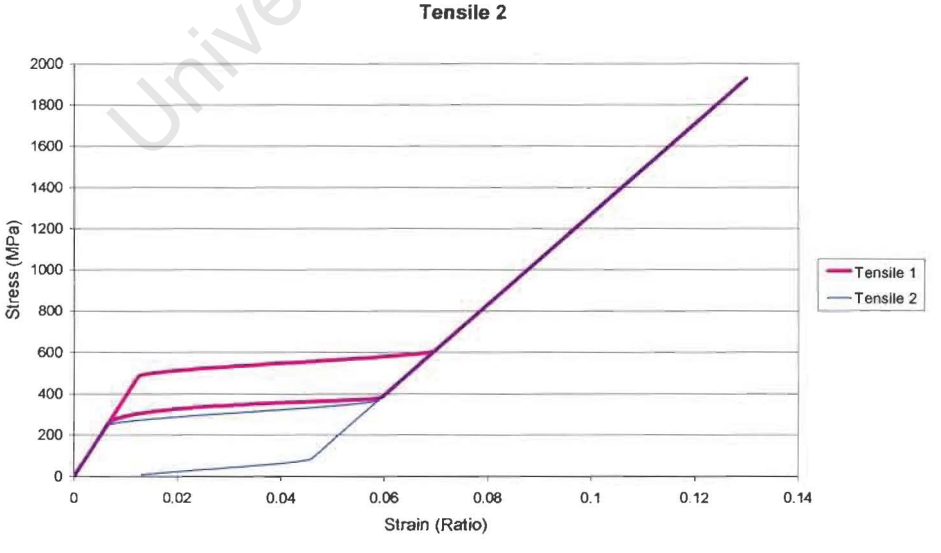

Figure 4-18 Stress vs. strain curve for model Tensile1 and Tensile2.

Temperature Derivative with Temperature Field

To investigate the validity of the material model further, Tensile2 was run again with a temperature field of 37°C defined over the entire geometry. This model was named Tensile3. *Figure 4-19* shows the stress vs. strain curve for Tensile3 together with that for Tesile1. The curves for Tensile1 and Tesile3 are exactly the same.

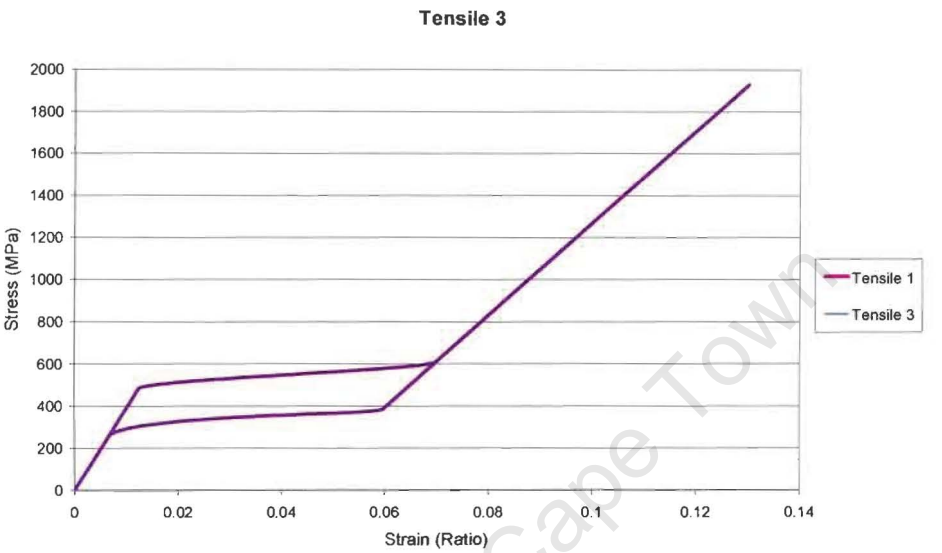

Figure 4-19: The stress vs. strain curves for Tensile1 and Tensile3

It appears that if no temperature field will be defined and the model is run at the same temperature for which the values were entered, then the temperature strain derivatives should be defined to be zero, as done in Tensile 1.

4.3.4 Boundary Condition Verification

In this section, results are given for the models EL(0.0635) and EL(0.0635)BC, described in *Section 3.3.5*.

Stabilisation and Strain Energy

In *Figure 4-20* the dissipated energy (% of strain energy) is plotted vs. luminal pressure for the models with different boundary conditions. Curves are plotted for EL(0.0636)BC and EL(0.0635).

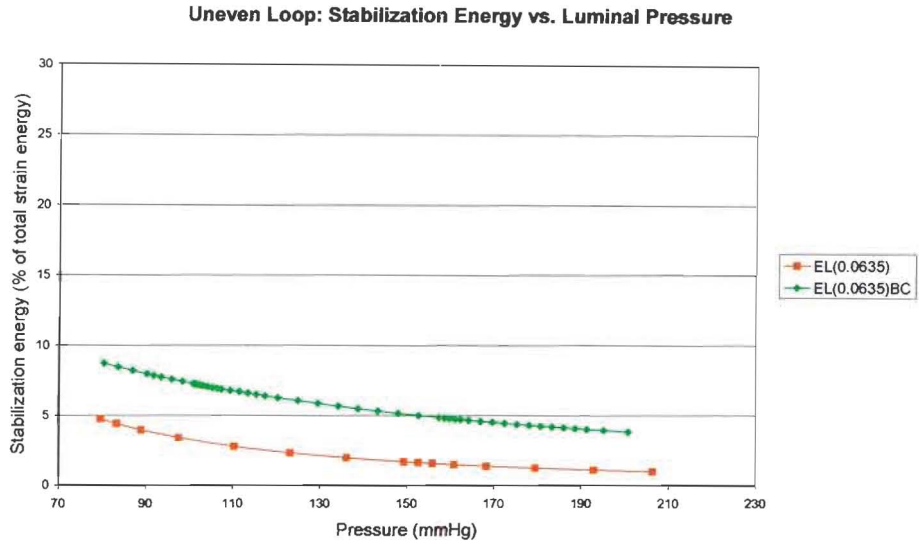

Figure 4-20: Energy dissipated through stabilisation (% of total strain energy) vs. luminal pressure (MPa), for models with slightly varied boundary conditions

EL(0.0635)BC has slightly higher dissipated stabilisation energy percentage than EL(0.0635). The values for both models still fall within the predefined limit.

Radial Deformation

In *Figure 4-21* a graph is plotted of luminal pressure (mmHg) vs. internal diameter change (% change from initial diameter at 0mmHg) was plotted for the boundary condition verification model.

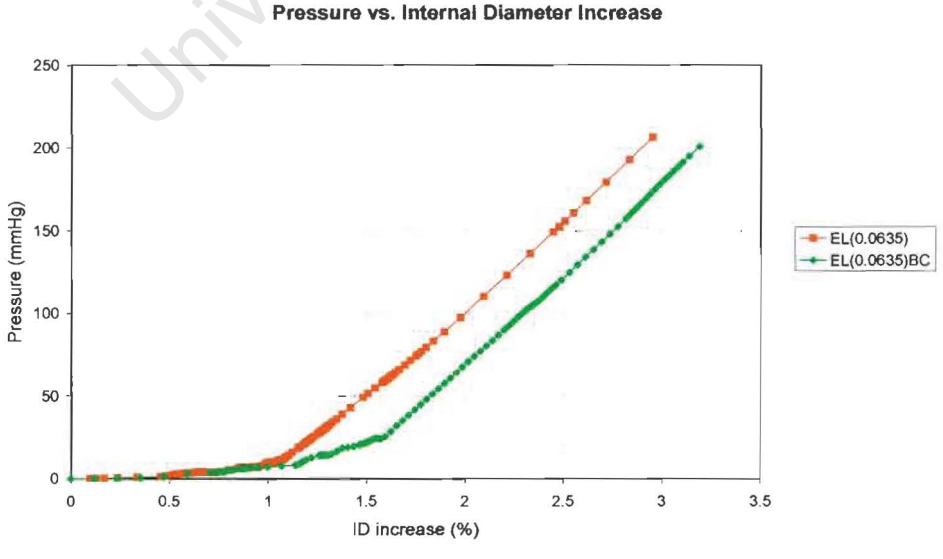

Figure 4-21: Graph of Luminal Pressure (mmHg) vs. Internal Diameter (%) for the boundary condition verification model.

The point of distinct gradient change is shifted slightly further along the ID increase axis for EL(0.0635)BC. The final gradients of the two models are very similar.

Compliance

The compliance values as well as the pressure ranges over which they were calculated are given in *Table 4-11.*

Table 4-11: Compliance values for EL(0.0635) and EL(0.0635)BC..

Model	Compliance (%/100 mmHg)	Pressure Range (mmHg)	
		Minimum	Maximum
EL(0.0635)	0.92	80	123
EL(0.0635)BC	0.93	80	120

The compliance values for both models in *Table 4-11* are very similar. The change in boundary conditions did not adversely affect the compliance results.

Maximum Principal Stress

The maximum principal stresses in the two models are recorded at pressures close to 80mmHg, 120mmHg and 200mmHg in *Table 4-12.* The stress distribution was the same as indicated in *Figure 4-5.*

Table 4-12: Maximum principal stresses at 80, 120 and 200 mmHg for EL(0.0635) and EL(0.0635)BC..

Model	80 mmHg		120 mmHg		200 mmHg	
	P (mmHg)	Stress (MPa)	P (mmHg)	Stress (MPa)	P (mmHg)	Stress (MPa)
EL(0.0635)	80	87.0	123	131.9	206	218.3
EL(0.0635)BC	80	111.4	120	167.0	200	259.5

Even though the stress values of EL(0.0635)BC is consistently higher than that of EL(0.0635), the position of maximum principal stress was the same for both EL(0.0635) and EL(0.0635)BC.

Maximum Principal Strain

The maximum principal strains in the two models are recorded at pressures close to 80 mmHg, 120 mmHg and 200 mmHg respectively in *Table 4-13.* These stress distribution was the same as in *Figure 4-7.*

Table 4-13: Maximum principal strains at 80, 120 and 200 mmHg for EL(0.0635) and EL(0.0635BC).

Model	80 mmHg		120 mmHg		200 mmHg	
	P (mmHg)	Strain (MPa)	P (mmHg)	Strain (MPa)	P (mmHg)	Strain (MPa)
EL(0.0635)	80	0.32	123	0.43	206	0.66
EL(0.0635)BC	80	0.48	120	0.68	200	1.73

The maximum principal strain values are also consistently higher for EL(0.0635)BC compared to EL(0.0635). As with maximum principal stress, the positions of maximum principal strains are the same in both models.

4.3.5 Contact definition verification

Strain energy and stabilisation

Dissipated energy (% of strain energy) is plotted vs. luminal pressure for the models with different contact definition in *Figure 4-22*. Curves are plotted for EL(0.05)Auto and EL(0.05).

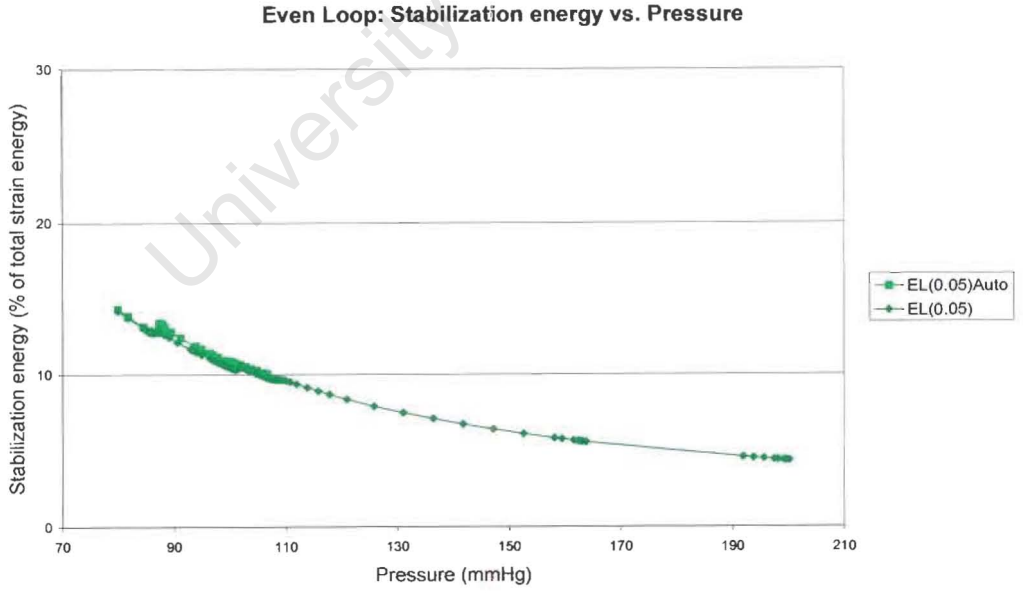

Figure 4-22: Energy dissipated through stabilisation (% of total strain energy) vs. luminal pressure, plotted for models with different contact definitions.

EL(0.05)Auto and EL(0.05) has very similar stabilisation energy percentages.

Radial Deformation

In *Figure 4-23* a graph is plotted of luminal pressure (mmHg) vs. internal diameter increase (% change from initial diameter at 0mmHg) for EL(0.05)Auto and EL(0.05). Values are plotted from 0 mmHg to approximately 200mmHg.

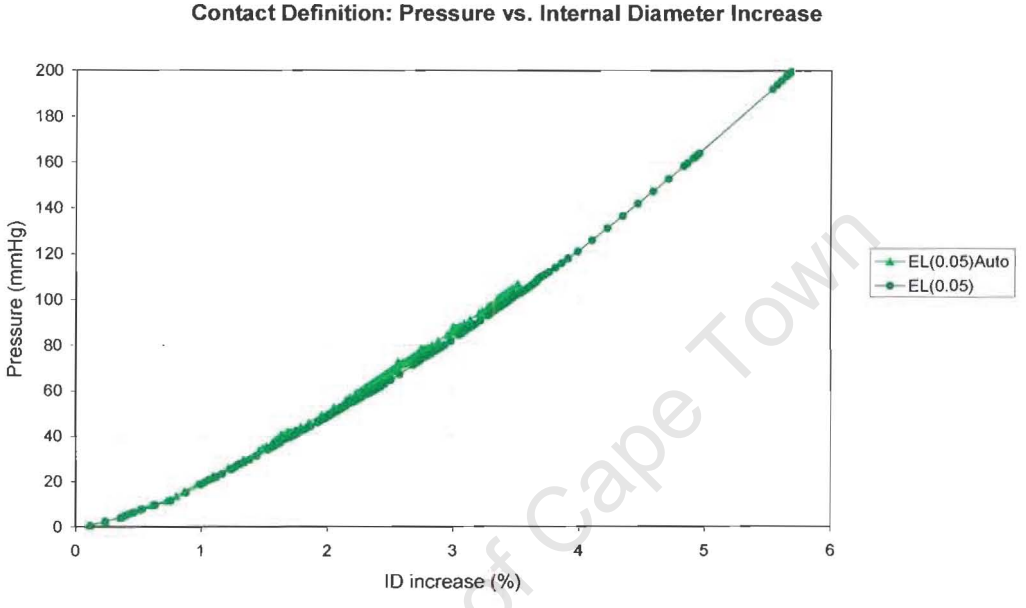

Figure 4-23: Luminal Pressure (mmHg) vs. Internal Diameter (%) for the contact verification model.

The difference between the results of the two models is negligible.

Compliance

As EL(0.0635)Auto terminated shortly after reaching an internal diameter corresponding to 80 mmHg, the compliance between 80 and 120 mmHg could not be calculated. Compliance results can therefore not be used to compare the results of these two models.

Maximum Principal Stress

The maximum principal stresses in the two models are recorded at pressures closest to 80mmHg in *Table 4-14*. The maximum principal stress of EL(0.0635)Auto was not available at 120mmHg and 200mmHg due to premature termination of the model and therefore these values could not be compared.

Table 4-14 : Maximum principal stresses at 80 mmHg for EL(0.05) and EL(0.05)Auto.

Model	80 mmHg	
	P (mmHg)	Stress (MPa)
EL(0.05)	80	177.2
EL(0.05)Auto	80	178.1

The maximum principal stress values at 80 mmHg are very close.

Maximum principal strain

The maximum principal strains in the two models are recorded at pressures closest to 80mmHg in *Table 4-15*. As before, the maximum principal strain of EL(0.0635)Auto was not available at 120mmHg and 200mmHg and therefore cannot be compared.

Table 4-15 : Maximum principal strain at 80 mmHg for EL(0.05) and EL(0.05)Auto.

Model	80 mmHg	
	P (mmHg)	Strain (MPa)
EL(0.05)	80	0.46
EL(0.05)Auto	80	0.59

The maximum principal stress values for EL(0.0635) and EL(0.0635)Auto are very close to each other at 80mmHg.

4.3.6 Verification of Geometry for Uneven Loop Models

Strain Energy and Stabilisation

Dissipated energy (% of strain energy) is plotted vs. luminal pressure (mmHg) in Figure 4-24. Curves are plotted for UL(0.0635) and UL(0.0635)Large.

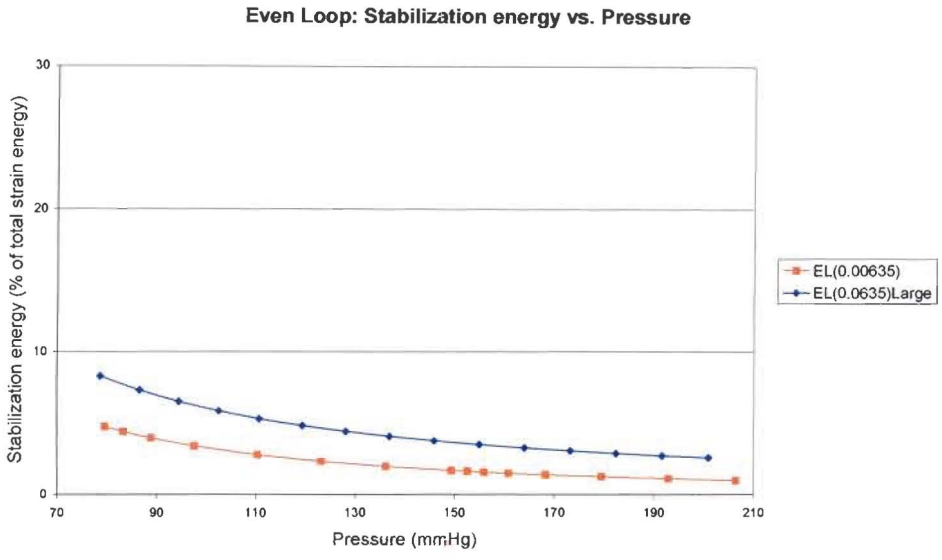

Figure 4-24: Energy dissipated through stabilisation (% of total strain energy) vs. luminal pressure, plotted for models with different loop geometries.

UL(0.05)Large has higher dissipated stabilisation energy percentage than UL(0.05), but for both models, the values fall within the predefined parameters.

Radial Deformation

In *Figure 4-25* a graph is plotted of luminal pressure (mmHg) vs. internal diameter change (% change from initial diameter) for EL(0.05)Auto and EL(0.05). Values are plotted from 0 mmHg to approximately 200 mmHg.

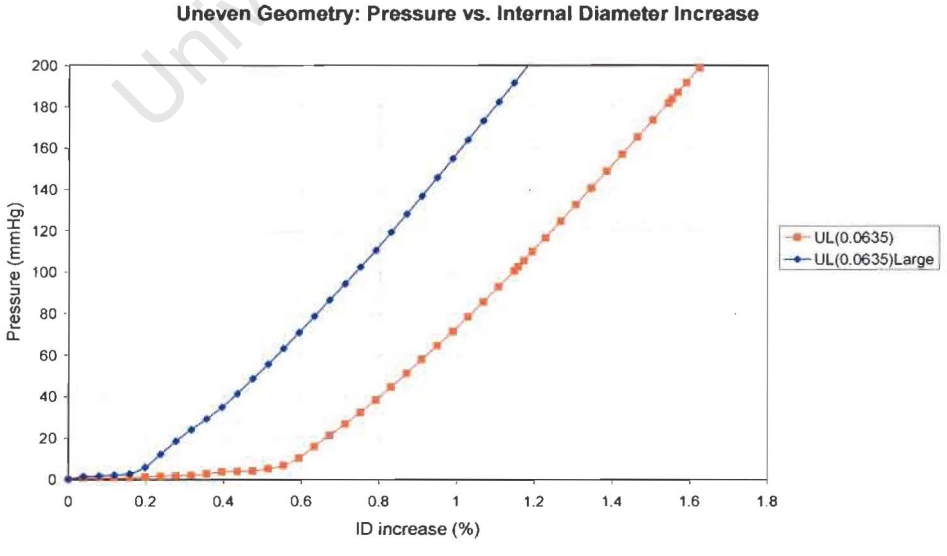

Figure 4-25: Graph of Luminal Pressure (mmHg) vs. Internal Diameter (%) for UL(0.0635) and UL(0.0635)Large.

The model created from the large loop geometry, UL(0.05)Large, has a slightly steeper gradient than UL(0.05). UL(0.05)Large also has an earlier gradient change at around 0.2% ID increase, compared to UL(0.05), which changes gradient at around 0.5% ID increase.

Compliance

The compliance values as well as the pressure ranges over which they were calculated are given in *Table 4-16*.

Table 4-16: Compliance values for UL(0.0635) and UL(0.0635)Large.

Model	Compliance (%/100 mmHg)	Pressure Range (mmHg)	
		Minimum	Maximum
UL(0.0635)	0.52	78	117
UL(0.0635)Large	0.48	79	119

The compliance results are close enough to be able to be explained by the change in boundary condition only.

Maximum Principal Stress

The maximum principal stresses in the models are recorded at pressures of 80 mmHg, 120 mmHg and 200 mmHg respectively in *Table 4-17*. The stress distributions at 200 mmHg for models EL(0.0635) and EL(0.0635)Large are shown in *Figure 4-26* and *Figure 4-27*.

Table 4-17: Maximum principal stress at 80, 120 and 200 mmHg for UL(0.065) and UL(0.0635)Large.

Model	80 mmHg		120 mmHg		200 mmHg	
	P (mmHg)	Stress (MPa)	P (mmHg)	Stress (MPa)	P (mmHg)	Stress (MPa)
UL(0.0635)	78	62.3	117	83.9	199	146.1
UL(0.0635)Large	79	66.6	119	95.9	201	164.7

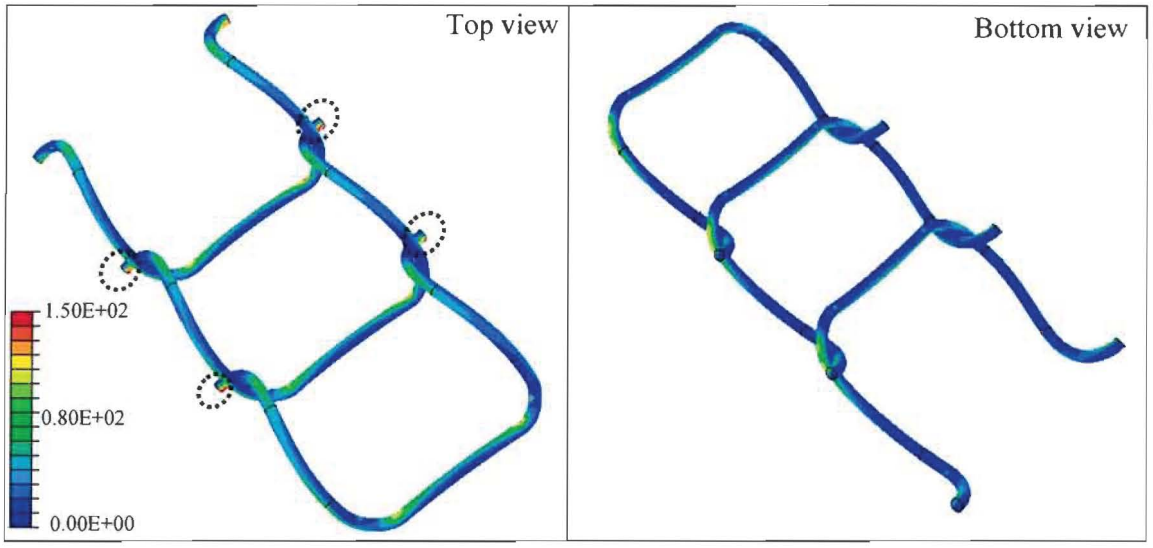

Figure 4-26: Stress distribution for uneven large loop geometry, UL(0.0635)Large, with positions of maximum strain indicated.

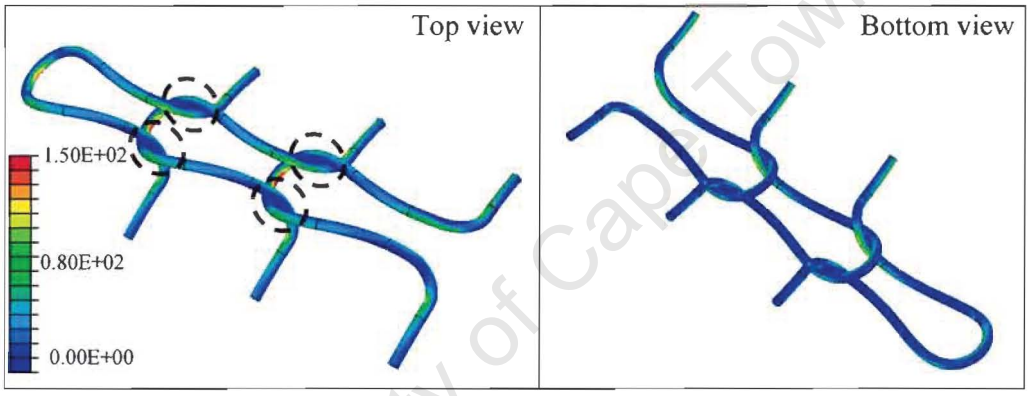

Figure 4-27: Stress distribution for uneven small loop geometry, UL(0.0635), with positions of maximum strain indicated.

Even though the maximum stress value present in EL(0.0635)Large is greater than EL(0.0635), the overall stress distribution appears very similar. The maximum values also occurred at the same positions.

Maximum Principal Strain

The maximum principal strain values are recorded at pressures of 80mmHg, 120mmHg and 200mmHg respectively in *Table 4-18*. The strain distributions at 200mmHg for models EL(0.0635) and EL(0.0635)Large are given in *Figure 4-28* and *Figure 4-29* respectively.

Table 4-18: Maximum principal strain at 80, 120 and 200 mmHg for UL(0.0635) and UL(0.0635)Large.

Model	80 mmHg		120 mmHg		200 mmHg	
	P(mmHg)	Strain	P(mmHg)	Strain	P(mmHg)	Strain
UL(0.0635)	78	0.34	117	0.41	199	0.59
UL(0.0635)Large Loop	79	0.39	119	0.58	201	0.97

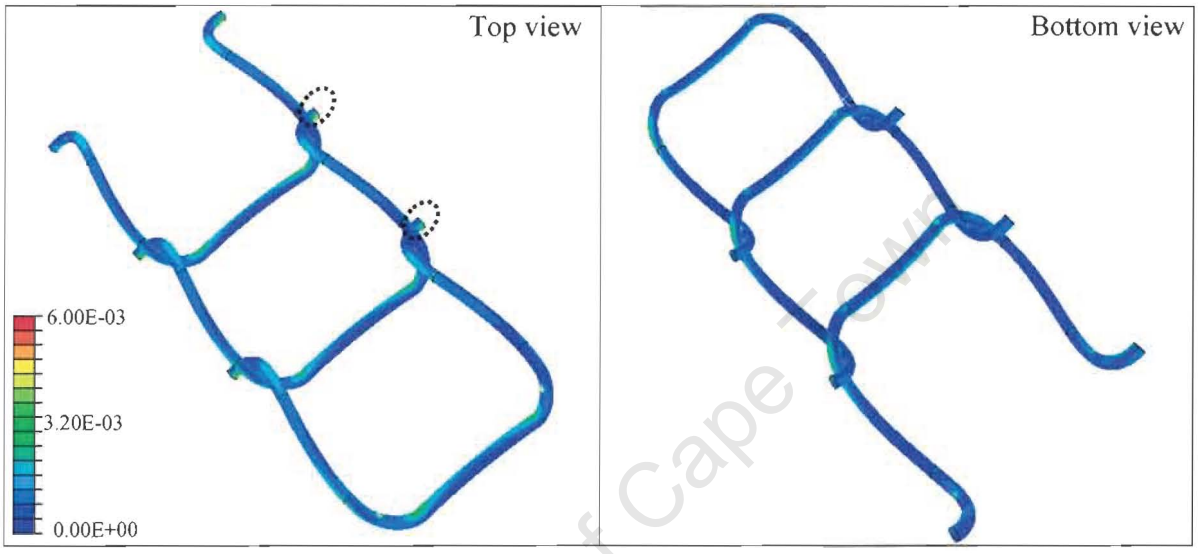

Figure 4-28: Strain distribution in uneven large loop geometry, UL(0.0635)Large, with positions of maximum strain indicated.

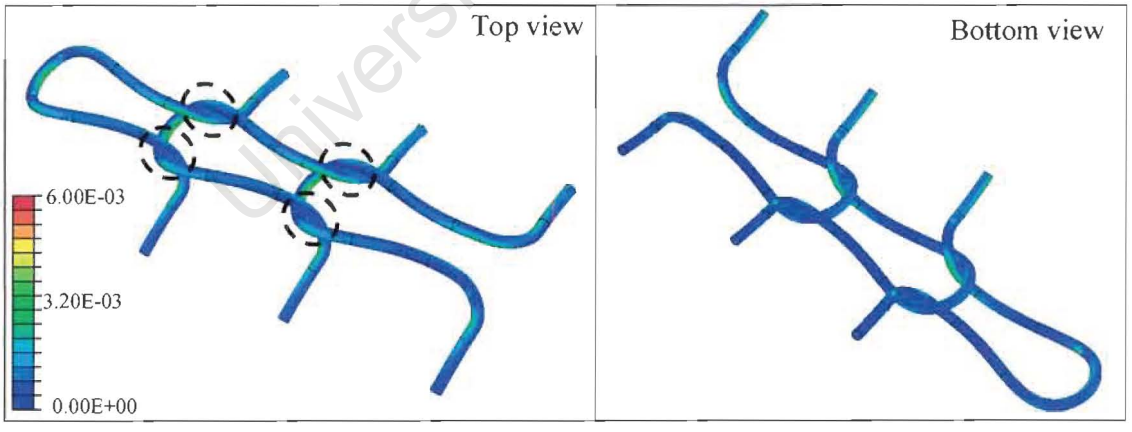

Figure 4-29: Strain distribution in uneven small loop geometry, UL(0.0635), with positions of maximum strain indicated.

Even though the maximum strains present in EL(0.0635)Large is greater than EL(0.0635), the overall strain distribution appears very similar. The maximum values also occurred at the same positions.

4.3.7 Comparison to Experimental Compliance Values

The compliance values obtained from the FEM models were compared to the different experimental values. Graphical representations of the compliance values of the even loop models are given in *Figure 4-30* and for the uneven loop models in *Figure 4-31*.

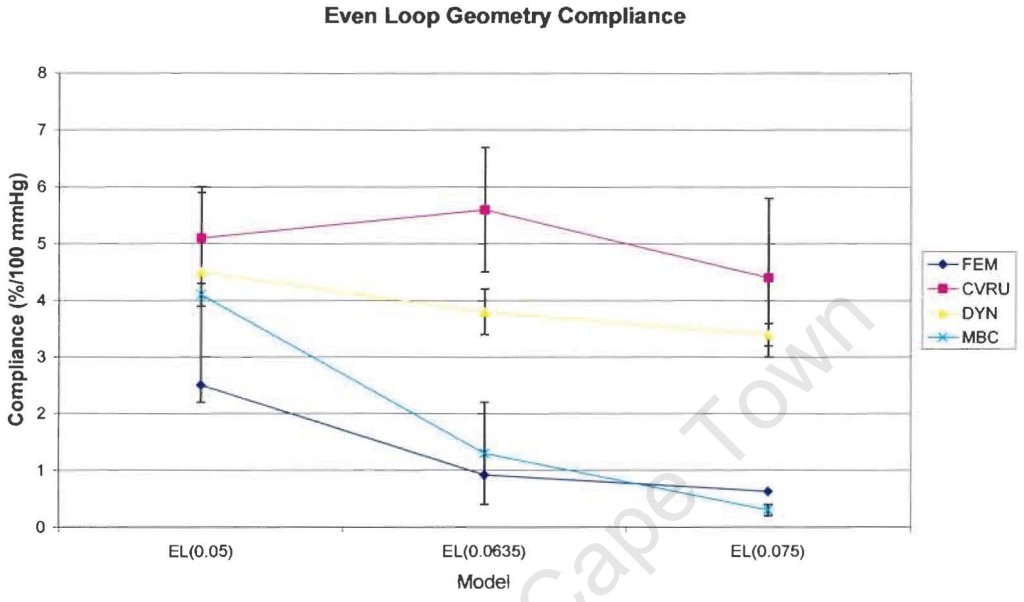

Figure 4-30: Comparison between compliance values of the FEM models and those from different experimental tests for the even loop models.

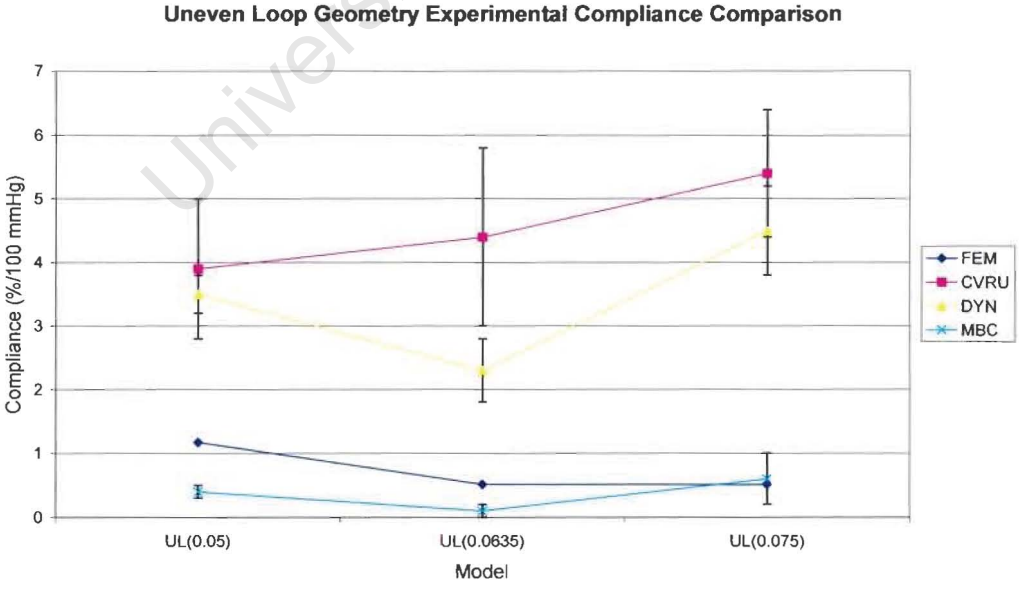

Figure 4-31: Comparison between compliance values of the FEM models and those from different experimental tests for the uneven loop geometry.

As can be seen the results for the different test vary considerably. It is important to bear in mind that the all the tests are based on different procedures and principles, all with their individual shortcomings. For the even loop structures the overall trend in all the numerical models and experimental tests appear to be a decrease in compliance with increasing wire thickness. EL(0.0635) does not follow this trend for the CVRU tests. Both the Dynatek Dalta tests, Medronic MBC tests and FEM models indicate a larger decrease from EL(0.05) to EL(0.0635) than from EL(0.0635) to EL(0.075). For all uneven loop experimental tests, the overall trend appears to be an increase of compliance with increasing wire thickness, a trend not displayed by the FEM models. Dynatek Dalta tests, Medtronic MBC tests and FEM results all show a decrease in compliance from UL(0.05) to UL(0.0635), while all three experimental tests show an increase in compliance from UL(0.0635) to UL(0.075). This increase is not seen in the FEM model where the compliance values of UL(0.0635) and UL(0.075) are very close to each other. With the exception of EL(0.05), the MBC values lie in the same region as those from the FEM models, while values from CVRU and Dynatek Dalta are much higher; the CVRU values being the highest of these two.

CHAPTER 5: DISCUSSION

The development of the six models, EL(0.05), EL(0.0635), EL(0.075), UL(0.05), UL(0.0635) and UL(0.075), is discussed in *Section 5.1*. Comparisons are made to the modelling approaches followed by authors analysing the mechanical behaviour of intravascular stents. In *Section 5.2* results of the six models are discussed and compared to each other and to experimental results from different groups. While discussing these six models, the results of models used in the verification of the different aspects of their construction are also referred to. The results analysed in intravascular stents models were also listed, however the actual values cannot be compared to the results reported in this thesis due to structural differences. In *Section 5.3* the FEM results of the six models analysed in this thesis are compared to experimental tests which were previously conducted on the same structures. Finally, in *Section 5.4*, the relevance of the FEM models results to the medical field is highlighted.

5.1 Creating the Finite Element Model

The geometry of each of the six models analysed in this thesis was created by implementing a three-dimensional repeatable unit cell as wire overlap is one of the major geometric characteristics of the knitted structure and can only be accounted for in three dimensions. In literature three-dimensional geometries were implemented in the creation of intravascular stents models and can be split into the following categories (in order of increasing degree of simplification):

- Models without geometrical simplification [2, 91]
- Models with some degree of symmetry simplification [3, 5, 8, 90]
- Models using a repeatable unit cell [4, 6, 9]
- A model consisting of one eighth of a symmetric unit cell [10]

Some authors implemented planar geometries for intravascular stent models. This was done in four ways:

- Creating the entire stent geometry in two dimensions and then mapping it onto a cylindrical coordinate system [1]

- Creating the planar unit cell geometry and then mapping it onto a cylindrical coordinate system [7]
- Keeping a unit cell geometry in a planar state throughout the analysis [32]
- The use of a two dimensional unit cell to create different geometries, justified by showing how a three dimensional geometry experienced much larger stresses in the circumferential than in the radial direction[4].

Dumoulin and Cochelin [4] used tie-constraints to link end surface behaviour of the unit cell in such a way as to assume infinite stent length. They analysed a highly symmetrical structure whereas the wire structures analysed in this thesis has helical climb angle in the design and overlap between the wires necessitating the addition of another unit cell at each longitudinal end of the model. One unit cell consisted of a single loop and therefore the basic assembly consisted of three single loops, although extra half loop sections were also added to the longitudinal ends of this structure to aid in the boundary condition definition.

To define the mesh in the wire loop assembly, tri-linear (first order) brick elements were used. Elements used in the literature to mesh intravascular stent models include:

- Quadratic tetrahedral elements [2, 8]
- Tri-quadratic brick elements [10]
- Tri-linear brick elements [3, 90, 91]
- Beam elements [1]
- Quadratic two-dimensional elements [4]

In this the current models, linear brick elements were used to generate the mesh, even though quadratic tetrahedral elements behave better under bending conditions. Tetrahedral elements are not advised for use with contact definitions, which occur abundantly in these models, and they are computationally more expensive. For these reasons tri-linear brick elements were chosen, even though they have a tendency to behave overly stiff under bending conditions where a coarse mesh is used. To counter this negative trait a finer mesh was implemented in regions of high curvature. It is also useful to mesh the areas of contact with a finer mesh as the smoother surface leads to easier convergence. In the loop assembly, areas of contact coincided with areas of high curvature. In addition, the regions of large curvature were expected to be of greater

interest with regard to deformations, stresses, and strains. The single loops were longitudinally partitioned into regions of high and low curvature in order to accommodate the different mesh density definitions. A fine mesh could alternatively have been applied throughout the entire loop geometry without negatively impacting the results, however assigning a coarser mesh to regions of low curvature aimed at reducing the computational requirements of the numerical models without compromising the results. In literature, a refined mesh has previously been used in regions where mechanical properties were of more interest [7, 90] as well as regions of expected contact [7, 91].

Six verification models were created from EL(0.0635) to investigate the sensitivity to mesh density and element type. Sensitivity analyses are an established measure for determining optimum mesh density [2, 3, 8, 10]. Migliavacca et al. [3] additionally conducted a sensitivity analysis to determine whether the element type had any significant impact on the results by analysing three models of increasing mesh density meshed with quadratic tetrahedral elements, compared to the tri-linear elements used to mesh their final models.

Three mesh verification models are presented in this thesis to determine the sensitivity to element type and are described in *Section 3.3.1*. Models EL(0.0635)Trhr1, EL(0.0635)Trhr2 and EL(0.0635)Trhr3 were created with increasing quadratic tetrahedral element mesh density as well as increasing dissipated energy fraction. The dissipated energy fraction had to be increased for increasing mesh density in order to ensure overall model convergence. This however led to an increase of stabilisation energy percentage with increasing mesh density, as can be seen in *Figure 4-9*, with the finest meshed model falling just outside the specified range at 80 mmHg. The stabilisation factor could however not be decreased further without preventing convergence. The tetrahedral element models all produced higher stabilisation energy percentages than EL(0.0635), highlighting the dependence of stabilisation on mesh assignment. Differences in radial deformation are barely detectable in *Figure 4-10* while compliance values, which are slightly lower for the tetrahedral element models, differ with less than 5% from that of EL(0.0635). The distinct change in deformation gradient seems to occur at a slightly higher pressure in the tetrahedral models and could possibly be attributed to inaccurate contact response, as tetrahedral elements are known to perform poorly in contact problems. The maximum principal stress values occurred in

corresponding positions with values in tetrahedral element model being slightly higher; also a possible consequence of less accurate contact response. The difference in these values decreased slightly with increasing pressure and at 200mmHg the tetrahedral model none of the values are more than 10% higher than those of EL(0.0635). The principal strains were smaller for the tetrahedral element models, but occurred at the centre of the loop as in EL(0.0635). However, none of the tetrahedral models have increased strain values at the areas of contact, strengthening the possibility that differences in the results can be ascribed to contact inconsistencies. There seems to be very little variation in results between the different mesh densities of tetrahedral elements and their results correspond well to those of the linear brick elements. It can therefore be concluded that the results are not influenced by the chosen elements type.

A further three verification models (described in *Section 3.3.2)* were created to determine the sensitivity to mesh density. Models EL(0.0635)Coarse, EL(0.0635)Fine2 and EL(0.0635)Fine3 were created using increasing mesh density of tri-linear brick elements, as well as increasing dissipated energy fraction to ensure convergence. For model EL(0.0635)Fine3 convergence could not be achieved with a stabilisation energy percentage falling within the specified limits. To aid in the convergence of this model, the contact definition was further softened (verification that this change only influenced the rate of convergence follows later). The final converged model, EL(0.0635)Fine3, still had stabilisation energy values larger than the defined limits, but this could not be decreased further. In the majority of the mechanical factors analysed, the results obtained from EL(0.0635) did not follow the trend displayed by the other three models. This serves as an indication that a coarser mesh could in fact not be used without compromising the accuracy of the results. The increase in dissipated energy fraction with increasing mesh density again leads to the increase in stabilisation percentage. The radial deformations in *Figure 4-16* are shown to converge as curves for EL(0.0635), EL(0.0635)Fine2 and EL(0.0635)Fine3 are very close to one another. Furthermore no significant differences in compliance, maximum principal stress or maximum principal strain results were noted between EL(0.0635) and EL(0.0635)Coarse. All of these results indicate that the refinement used in EL(0.0635) ensures sufficiently accurate results.

The material used to manufacture the structures was Nitinol, a nickel and titanium SMA. This material is often used in the manufacture of self-expandable intravascular stents. No previous studies comparing different Nitinol stents designs could be found. There is

however a discussion on material parameter variation as a possible optimisation technique for these stents [9] and a fatigue analysis using a FEM model of a Nitinol self-expandable stent [10]. Models of balloon expandable stents used different material models which all described stainless steel [1-8, 90, 91]. McGarry et al. [32] also used a steel material model in their simulations, but the objective was to demonstrate the difference in the results obtained by using two different models for the same material.

The material behaviour of Nitinol generates analysis difficulties, due to the large degree of non-linearity present, and an efficient material model needs to be implemented [9, 10, 93]. Migliavacca et al. [3] also noted that material non-linearities can lead to solution difficulties. Whitcher [10] used a Von Mises yield-criterion elastic-plastic material model in ADINA which has been shown to correspond well with the behaviour of SMAs in isothermal monotonic loading simulations. In the six support structure models the ABAQUS UMAT for Nitinol, which is based on the generalised plasticity theory [79, 80], was implemented to describe the behaviour of the stent; a material description which was also used by Gong and Pelton [9]. Input material parameters used in this thesis were determined from experimental tests conducted on Nitinol wire samples which correspond to the wires constituting the knitted support structures. Some values were not obtainable from one dimensional tensile testing and were obtained from collaborators.

In order to verify the validity of the material model, results of simulated tensile tests were compared to the experimentally determined model. The FEM tensile test wire was meshed with the same number of elements trough the wire thickness as was used in EL(0.0635). Simulating a wire length equal to that of the experimental tensile tests (100mm) presented the numerical problem which was too large to be solved with the available computational resources. It was verified that the stress-strain response of models with 10mm and 50mm wire lengths were exactly the same. This occurs most likely because even the shortest length modelled (10mm), was still large in comparison to the wire diameter (0.0635mm). Model Tensile1 had a value of zero for Loading and Unloading Temperature Derivative of Stress. Results from Tensile2 confirmed that when no temperature field is defined, models run by default at 0 degrees Celsius. This is acceptable if the Temperature Derivatives of Stress is defined to be zero (as in Tensile1), since the transformation stress values will be the same for all temperature values (see *Figure 3-21*). However if these values are non zero, a temperature field should be defined to ensure that models are executed at the correct temperature, as the transformation stress

values will be temperature dependent. The shape of the stress vs. strain curve obtained from the tensile test model corresponds to that of the experimental tests. The curves could not be directly compared, as values used for the material model were averages determined from a number of experimental tensile tests. The FEM output stress vs. strain curves showed a response corresponding to the values which were used as input parameters.

The boundary conditions, which were used to account for geometrical simplifications and prevent rigid body motion, were described in *Section 3.2.1.4*. In literature, most of the intravascular stent models included boundary conditions to account for geometry simplification and to prevent rigid body motion as well as longitudinal motion of the prosthesis [3, 4, 6, 7, 10, 32, 90, 91]. In this thesis a verification model, EL(0.0635)BC (described in *Section 3.3.5)*, was created with a slight variation in boundary conditions still describing similar behaviour as EL(0.0635). This was done in order to ensure that a small change in boundary conditions did not result in a large variation in output, as that would indicate instability within the model. The results, compared in *Section 4.3.4*, do not show a large disparity and therefore the boundary conditions that were chosen appear to result in a stable model.

Due to the three dimensional nature of the knitted design, contact had to be defined between the overlapping wire surfaces in model EL(0.0635). In literature, contact between wire-surfaces of intravascular stents had to be defined only in stent flexibility analyses, as radial expansion of stents will most likely not result in contact between the wires.

Contact was defined between the intravascular stent and balloon and/or artery surface in various models of intravascular stents [1, 6, 7, 90, 91]. The absence of interaction between the stents and one or more of these components was listed as a major limitation of some intravascular stent models [3, 5, 8, 91]. Lally et al [7] named the absence of modelling a rupture or damage mechanism for the plaque as their main limitation. In the models described in this thesis, contact was defined between the rigid expander surface (used for the loading definition) and the luminal surface of our wire structure. Frictionless contact was implemented (as in [7, 91]) to avoid complicating the analysis even further. A highly non-linear material model [3, 9] as well as an abundance of contact definitions already resulted in a highly non-linear set of equations to be solved.

All contact definitions used softened contact, which allowed for easier convergence of the equilibrium equations of the problem. Curved surfaces in FEM problems are never truly smooth, due to the assignment of the mesh. Nodes on the slave surface were less likely to get hooked onto nodes on the master surface when softened contact is used, as surfaces remained a small distance from each other. The parameters used to define softened contact in these models were chosen to approximate hard contact closely in order to ensure as accurate results as possible. In two models, EL(0.05) and EL(0.0635)Fine3, convergence was extremely slow and the analyses terminated before the desired luminal pressure was reached. Their contact definitions were softened further to aid in their rate of convergence. Model EL(0.05) was compared to model EL(0.05)Auto, with the original contact definition, and the stabilisation, radial deformation, stress and strain results variations were barely visible in the curves, and values given differ by very small amounts. It was therefore concluded that the change in contact definition only affected the convergence rate.

The loading definition used in this work was implemented through a rigid surface, lying luminal to the stent and undergoing radial displacement linearly over time. Loading in many of the intravascular stents models consisted of a linearly increasing pressure applied to the inner surface of the stent [2-4, 6, 10, 91], while David Chua et al. [90] applied linearly increasing pressure to a balloon surface which lay luminal to the stent. Displacement loading of the stent was employed by some authors [1, 4, 5, 8, 32]. Holzapfel [91] stated that applying luminal pressure to the stent allows for more realistic behaviour of the stent than displacement loading, as the various regions of the stent will not necessarily undergo the same displacement with the same amount of luminal pressure applied. With displacement applied to an internal expander surface, instead of the stent nodes, this problem was greatly decreased as stent nodes were able to move in different directions during load increase, not only in the increasing radial direction. Tan and Liu [1] separated loading into two steps: first the stent was crimped onto the balloon, followed by the expansion of the balloon while the stent underwent radial compression by the artery. Lally et al. [7] only modelled the compressive forces caused by the artery while Petrini et al. [8] considered only the flexibility of the stents.

The modelling strategy applied to create the models of our six geometry variations were developed from strategies in the available literature while considering the differences between the wire support structure and intravascular stents. All aspects of the final

models were intensively verified through creation of verification models, which confirmed the proposed modelling strategy to deliver models which are adequately stable.

5.2 Comparison between FEM Models

Six different models were created and their simulated mechanical properties analysed. The differences in the results of these six models were analysed and will be discussed. In literature, the effect of variation in intravascular stent design on its mechanical properties has been highlighted [1, 5, 7, 91]. Results reported in literature were not explicitly compared to those from this thesis, as there are too many differences in analysis aims and geometry. Similar output variables were however analysed here, as from literature FEM has already proved to be useful in analysing these results. Results analysed in literature were as follows:

- The pressure necessary for stent deployment was often reported [1, 5, 6, 90].
- Deformation results (eg. recoil values, foreshortening and dogboning) [1-4, 7, 32, 90].
- Stress distributions in intravascular stents [1-7, 32, 90, 91].
- Strain distributions in intravascular stents [1, 4-6].
- Fatigue analyses through the use of a Goodman diagram [10, 32].
- Resistance to compressive forces [5].

Deformation, stress and strain results were analysed also analysed in this thesis. Some deformation results did not apply to the current analysis and will be discussed further later. Resistance to compressive forces was and pressure necessary for stent deployment was not relevant quantities in this analysis. Fatigue analysis could be done in future, but falls outside the scope for this thesis.

The first output variable which was analysed was the total energy dissipated due to stabilisation (see *Section 4.2.1*). Stabilisation had to be implemented to prevent local instabilities in the highly non-linear material model. This option also had to be selected in order for the tensile test model to converge, which indicates that the instability most likely stemmed from the material definition and not the non-linearities resulting from contact or non-linear geometry. Initially the default value for dissipated energy fraction

was used in all six models. This lead to stabilisation energy equalling a high percentage of the total strain energy in EL(0.0635) and UL(0.075) and the dissipated energy fraction was decreased to a value which ensures these models' stabilisation energy was within the predefined limits. The stabilisation energies do not appear to follow a specific trend. This could be explained by the difference in meshing caused by the automatic mesh generation, as the stabilisation matrix depends partly on the mesh definition.

Radial displacements (the main quantifiable deformation results) are reported in *Figure 4-3* and *Figure 4-4* by means of plot of luminal pressure increase vs. internal stent diameter increase. Although luminal pressure was not explicitly used to define the loading condition of the models, it could be calculated from the reaction force of the stent wires onto the expander as explained in *Section 3.2.3*.

If foreshortening was to be determined from the six models analysed in this thesis, the boundary conditions at the longitudinal ends of the model would have to be changed to allow longitudinal movement of these ends. As the greatest influence in determining the foreshortening of the stent within a cardiac cycle is the friction between the support structure and other components of the vascular prosthesis, meaningful foreshortening results can not be determined unless the other components of the prosthesis are also included in the simulation. Such a study was however not feasible with the current computational resources, as the highly non-linear behaviour of the material model as well as the considerable amount of contact surfaces defined already produced a complex numerical problem. Radial recoil and dogboning could also not be determined without the inclusion of a luminal prosthesis component, as neither process will take place against the current rigid luminal expander. In a complete prosthesis, one component should always lay luminal to the support structure, and therefore radial recoil and dogboning would greatly depend on the stiffness of this luminal component. These displacement quantities could possibly be determined in future studies if other components of the prosthesis are included.

The radial deformation of the structures in this thesis are also influenced by the behaviour of other components in a multi-component graft; however the values obtained from this study can be used to compare different proposed geometries by excluding completely the effect of luminal components. In future, studies can be conducted with the inclusion of s variety of different components and these results can then be compared to determine the

respective effects of these components. The current proposed FEM procedure could be adapted to include these components if more computational resources are available.

In *Figure 4-3* and *Figure 4-4* a distinct gradient change can be observed for all the models except EL(0.05), which resulted in a smooth curve. From the deformation plots in ABAQUS, the change in gradient is seen to occur at the point where gaps between the wire-contact surfaces are closed and the radial displacement becomes dependent only on the deformation (bending) of the wires. *Figure 5-1* shows a plot of the wire contact areas just before and after the change in gradient occurred.

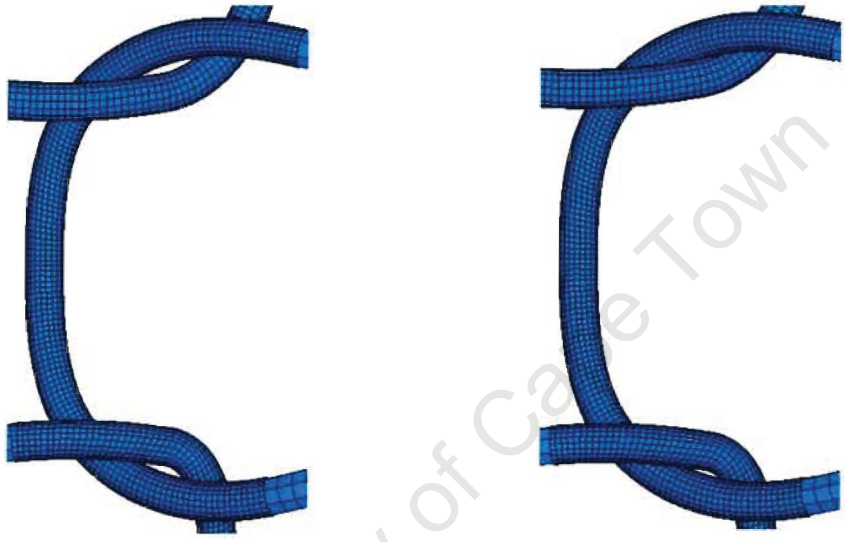

Figure 5-1: Illustrations of the wire-contact areas (a) before and (b) after the change in gradient occurs in the internal diameter increase curve.

The most significant trend that can be observed in both *Figure 4-3* and *Figure 4-4* is the increase in final gradient with wire thickness. The gradients are also in general steeper for the uneven loop geometry than for the even loop geometry. Global trends in diameter increase are offset by the fact that the ID change at which the gradient transition occurs is unpredictable. This value is influenced by the ID change at which the wires lock tightly together, which in turn is affected by the following factors:

- Curvature of the loops
- Thickness of the wires
- Distance between the wire-contact surfaces at the start of the simulation
- The longitudinal distance between the loops at the start of the analysis
- Material stiffness

The curvature of the loops together with the thickness of the wire will determine how closely these contact surfaces will fit together. The distance between these surfaces at the start of the simulation also has an impact. A more loosely knit structure will undergo more internal diameter increase before the gradient change occurs. The longitudinal distance between the loops will also influence how close these bended contact surfaces are to each other. Additionally, the ease with which the wire loops bend is important, as the easier the loop undergoes bending, the less force has to be exerted by the contact surfaces to bend it open. This is the case in the even loop structure. The ABAQUS deformation plot indicates the contact surfaces moving closer to each other while the wire-loops start to bend open at the same time. This is different from the other models where the loops only start to undergo bending once the loops are tightly locked together.

Model EL(0.05) was observed to be the only model not experiencing the gradient change. As this is the only one of the six geometrical variation models with an altered contact definition, a first response would be to ascribe this behaviour to the different contact definition. This is however an unsatisfactory explanation, as one of the verification models, EL(0.0635)Fine3, was also run with the same altered contact definition and exhibited a change in gradient for the ID increase curve (refer to *Figure 4-16*). Furthermore model EL(0.05) is compared to model EL(0.05)Auto (see *Section 3.3.4)* and it can be observed from *Figure 4-26* that even with the original contact definition the model does not exhibit a change in gradient for the ID increase curve. In the other models, varying amounts of force needed to be exerted through the contact surfaces before loops opening occurred. Model EL(0.05) account for the most effortless radial expansion of all the variations analysed, and this is suggested to be the reason for which only EL(0.05) expands without the gradient change seen in other models.

It is important to be aware that the ID change at which gradient transition occurs can be influenced by small geometry variations occurring within a single design. It is proposed that this is due the fact that increase in internal diameter remain a small percentage of initial diameter and therefore the wire loops undergo little overall displacement during the expansion. Variations such as tightness of the knit or longitudinal stretching can lead to large differences in radial displacement of the structure at 200mmHg for the same loop design.

The pressure range at which the compliance values were calculated falls within the region where the final gradients in the ID change curve have already been reached and are not dependent on the absolute IDs. Compliance therefore depends only on the bending stiffness of the wire and the difference in loop design of the wire structures. Compliance values increase with decreasing wire diameter; possibly as thinner wires are likely to bend more easily and therefore can undergo radial expansion more readily. It is also noticeable that the compliance differs more between 0.05mm and 0.0635mm diameter wires than between 0.0635mm and 0.075mm diameter wires for both loop geometries. This indicates that ability to undergo bending during radial distension increased exponentially with a decrease in wire diameter. More wire thicknesses should be tested as confirmation. The lower compliance values of the uneven loop geometry compared to the even loop geometry can be ascribed to the difference in global geometry, which allows more bending in the even loop geometry.

Maximum principal stress distributions were obtained from the analyses and the positions and magnitude of the maximum values are reported in *Section 4.2.4*. From the stress distributions in the six models it was seen that the areas of largest maximum principal stresses lie at the centre of the wire loops. In the uneven loop geometry it occurs in the small loop, with the large loop experiencing lower stress. This is due a more concentrated bending force in the smaller loop. The largest values of maximum principal stress are given in *Table 4-3*. Stress values in the even geometry models are larger than those of the uneven geometry at the same pressure values.

Maximum principal strain distributions were obtained from the analyses and the positions and magnitudes of maximum principal strains are given in *Section 4.2.5*. The regions of largest maximum principal strain occur at areas of contact. For the even loop model the largest maximum principal strain values for EL(0.05) occurs at the same position as the maximum principal stress value. This can be related to the discussion on the variation in radial deformation with pressure previously discussed for model EL(0.05). The loops in this model start to bend open before the gaps between the wires are tightly closed. Less pressure needs to be exerted at the contact areas in order to bend the loop open. The strain values follow a similar trend to the stress values with increasing strain coinciding with decreasing wire thickness at the same luminal pressure. Values for even loop geometry are higher than for uneven loop geometry and larger differences are seen between 0.05mm and 0.0635mm models than between 0.0635mm and 0.075mm models.

Exceptions to these trends occur between the 0.05mm even loop and uneven model at 120mmHg and 20 mmHg. These values can not be explicitly compared, as values for EL(0.05) occur in a different region than those in the other models due to the difference. As proposed before, this is caused by the smooth expansion of EL(0.05) which leads to less pressure being exerted at the areas of contact. Another variation from the trend is that UL(0.075) experiences higher strain than both UL(0.0635) and EL(0.075). This result is suggested to be related to the gradient change seen at a larger ID change (*Figure 4-4*) which leads to a greater final ID. Due to the geometry as well as the wire's bending stiffness, the contact surfaces will push against each other with a more force than in other models, before the wire-loops will start to bend open. This increased force at the contact surface is proposed to be the reason for the high strain value observed in this model as well for as the high ID change value at the gradient transition in *Figure 4-4* .

In order to analyse the fatigue properties of the structure, a Goodman diagram for the specific Nitinol material used would have to be obtained experimentally, as the diagram is material specific. Maximum principal stress or strain, together with cyclic stress or strain values, could be used in future fatigue analyses of the structure.

Resistance to compressive forces was not analysed in this thesis, as no assumptions are made about what material will be used for components lying abluminal to the support structure. They also investigated stent flexibility. This could be useful to investigate in future for the six models discussed here, as the final prosthesis might have to be used in positions where bending is necessary. As the structure will form part of a vascular prosthesis, which will be implanted and not delivered, flexibility during delivery is not relevant.

5.3 Comparison to Experimental Compliance Tests

There is great variation in the compliance results between the three experimental tests and the FEM models. The testing procedures and principals were however very different. Compliance testing experiments were not conducted as part of the current project as these tests are very involved and would require a great deal of study and time.

In literature FEM models are also compared to experimental tests [6, 96, 97]. The geometry of intravascular stents lies in a plane, with no contact between metal wires, as is the case in the currently investigated knitted wire structures. There will be little variation

in longitudinal length between models and experimental samples. The investigated knitted structures however could have been stretched of contracted longitudinally before or during testing which could have a potentially large impact on the compliance, especially considering the small size of the compliance values obtained. It is possible that one set of experimental tests conducted could have some of the structures stretched while others are contracted. This could severely impact the compliance results. In the case of the FEM models, the wire loops there were vary little variation in longitudinal distance between the loops for the different designs. The Dynatek Dalta samples which were tested were 10 cm in length. This corresponds to over a hundred loops in longitudinal direction, leaving a lot of room for contraction and expansion. Tan and Liu [98] showed how small variation in the geometry of a intravascular stent could have a significant impact in its mechanical behaviour. A future study could focus on the effect of longitudinal stretching/contraction on the compliance results. This however does not fall within the scope of the current project.

In the CVRU tests the deformation undergone by the stent was different to that undergone in the other experimental tests and in the FEM models. The structures were not expanded radially, but in an elliptical fashion. We see from the FEM models that with the lower compliance values experienced, model EL(0.05) almost reached a maximum principal stress falling inside the pseudoelastic range. In the elliptical deformation the wire loops didn't deformed equally around the circumference, as some loops underwent more deformation and others less compared to loops undergoing circumferentially uniform deformation (as in the FEM models and for the other experimental tests). Loops undergoing more deformation can enter the superelastic region of the stress strain curve. If this happens, a much larger amount of strain will be experienced for a small increase in stress, leading to an enlarged compliance. The amount which the compliance is enlarged will depend on at which pressure during the analyses the superelastic range was reached. This can be different for the different designs as well as for the different wire thicknesses. If this range is reached at different pressures within the physiological range, the comparison between the different designs' compliance values will also be altered. This effectively means that the difference in deformation can have a larger effect in the compliance for some models than for others. No maximum principal stress or strain results are available for these tests and it is therefore not possible to determine when and if the superelastic effect was employed.

Dynatek Dalta conducted volumetric tensile tests with latex liners inside the wire structures, adjusting the testing pressures to account for the effect of the latex liner compliance from the total compliance of the system. What can however not be adjusted for is the bulging of the liner between the wire loops. This bulging could have a significant effect on the change in volume during the cycle, leading to increased compliance. The amount of bulging will mainly depend on the stiffness of the wire structure and the compliance of the liner. A stiffer wire structure will lead to more bulging of the liner, while a lower compliance of the liner will lead to less bulging. Since the stiffness of the structure is dependent on the design and the wire thickness, different structures will undergo different amounts of compliance increase, changing the comparison between the different designs.

Medtronic MBC also used a latex liner inside the structure to apply the testing pressure. The effect of the compliance of the liner was however not accounted for. The diameter change of the structure of the structure was measured by means of a laser micrometer. Although the volume change caused by the bulging of the liner will not have a significant effect on the compliance results. If the bulging of the liner extends beyond wire structure a larger diameter will most likely be measured than that of the wire structure. UL(0.075) is the only design in the Medtonic MBC tests for which the trend differs from the FEM models. From the FEM models it appeared that UL(0.075) is the stiffest structure. If this is in fact the case, the compliance of this structure could appear larger, due to the increased bulging of the liner. This is a possible reason for the difference in trend seen for UL(0.075) for the Medtronic MBC tests and the FEM models. The effect of the compensation for the liner can be another reason for the difference in results, but the current testing pressure corresponds to a smaller corrected pressure. If the latex liner was accounted for, measurements would have been taken at a higher pressure which is more likely to decrease the compliance further.

Measuring of the diameter of the system, bulging should have a smaller impact on the compliance results than in volumetric tests. For diameter measurements the error only occurs in one dimension, whereas an error due to volume change occurs in three dimensions thereby enlarging its effect. This could be one of the reasons why the compliance values seen in the Medtronic MBC tests are smaller than those for the Dynatek Dalta tests. In the diameter measurements, the bulging effect is also only

measured once, whereas in volumetric measurements, the additive effect of buldging at each loop is recorded.

All experimental tensile tests conducted included parameters that are not present in the FEM models. The purpose of the FEM analysis was to analyse the wire support structure only, without making assumptions of what other component would be included in a final graft. From the experimental tests it can however be seen that the effect of an inner lining on the behaviour of the structure is not necessarily directly related to the behaviour of the structure alone. Analysing the structure on its own does however allow a better understanding of its behaviour and is therefore not futile. The only experimental tests that did not include the effect of another component were the CVRU tests, but this tests was conducted under deformation very different to that of the FEM models or the physiological situation.

5.4 Relevance to Medical Field

The effect of different stent designs on the biological response of the artery has been discussed in literature [1, 6, 7]. As the expander surface (used in the loading definition of the six models) was not created as part of the assembly, but merely existed through an analytical definition using the reference point, it was not possible to determine the stress distribution caused by the support structure on the expander surface. Even if this result was determined, it would be meaningless since the expander is a rigid surface and not deformable as any realistic luminal component of the prosthesis would be. Furthermore, there was no graft component lying abluminal to the support structure in this model on which a stress distribution could be analysed. If other components of a vascular prosthesis are added to the model in future studies, an analysis of the stress exerted on them by the expander will be a useful analysis.

Even though suggestions are not made about the other component of such a composite graft, the support structure is not likely to experience great external compressive forces from possible abluminal components as it was designed to be the stiffest component in a multi-component prosthesis. This means the support structure is likely to contribute the greatest proportion to the stiffness of a proposed prosthesis and other components are unlikely do exert significant external compressive forces on it. The models were therefore

not created to determine the structures response to compressive forces exerted by abluminal surfaces onto the support structure.

The compliance values of all the models are lower than that of arteries and saphenous veins (refer to *Table 4-2*) and EL(0.05) is the only model possessing a compliance value higher than that of ePTFE and Dacron grafts. None of the models analysed in this work reached the physiological compliance, with the most compliant mode EL(0.05) only reaching about half that of an artery. The structure could possibly be used to serve the same purpose as the collagen fibres in natural vessels if used with one or more compliant inner linings. A truly non-linear stress-strain response was only seen in EL(0.05) as all the other models showed a distinct gradient change. This distinct change is dependent on small geometric variations which are likely to occur in practice in a medical setting. It is suggested that an important future study is the determination of degree of dependence which the compliance values have on these small variations.

A possible use of the current stiff structures could be as external support for existing vascular prosthesis. Many external wraps have been applied to a variety of vascular prosthesis resulting in reduced formation of IH, as discussed in *Section 2.3*. These multi-component prostheses appear to function at their peak if the external layer is highly porous allowing more graft healing. The support structure presented here has a knitted design which would allow much more tissue ingrowth compared to any fabric or porous material presented in the previous studies. None of the previous external wraps can compare to it with respect to porosity.

It is important to evaluate the effect of longitudinal stretching or contraction on the behaviour of the structure, as this could easily occur in a final graft. Even if care is taken that the initial length (before application to inner lining) and final length (after application to inner lining) is the same, there can still be some local stretching and compressive effects present in the graft, cancelling out over the complete length. Longitudinal stretching and compression could also be physiologically induced after implantation.

CHAPTER 6: CONCLUSION

The objective of this study was to analyse the mechanical behaviour of an existing wire support structure through the use of FEM and to establish a procedure by which models with geometric variation could easily be created towards mechanical optimisation of the structure. Geometry was successfully imported from CAD models into ABAQUS CAE. The material parameters for the Nitinol material used to create the structures were determined by means of an experimental tensile test. Through multiple verification models, the overall modelling approach proposed in *Section 3.2* has been shown to be numerically stable and can easily be applied to a variety of geometries.

Time constraints prevented more design variations from being analysed. If an optimised design is to be developed, more designs would need to be assessed. New models could look further into effects like:

- Additional wire thicknesses
- Amount of loops around the circumference
- Curvature of the loops
- Variation in helical climb angle
- Tightness of the knit
- The effects of longitudinal compression or expansion of the stent

The degree to which the compliance is dependent on small geometry variations (which would occur in a practical setting) is an important analysis. The models presented in this thesis could be adapted to determine this dependence. It is also possible that different models will have a different degree of dependence on these variations. The least amount of dependence will be preferred, and the presented modelling procedure can be adapted to determine which geometry has the smallest dependence on these variations

The absence of other components of the graft in the model prevents the analysis of quantities like foreshortening, dogboning and radial recoil. However, as the model already generates complex equations to be solved due to the material models and contact definition, more computational power would be needed to include these components. If

one of these components were abluminal to the wire support structure, the effect of external compression could also be analysed.

Another interesting future analysis will be determining the effect of different compliant inner linings on the compliance of the structure. The amount of bulging can be determined, as this will be an important parameter in the physiological setting. A highly bulged luminal surface could cause flow disturbances leading to an increase in IH, a highly undesired response.

A fatigue analysis can also be conducted from by using the maximum principal stress and strain values from the models. For this a Goodman diagram for the specific Nitinol material would first have to be determined experimentally.

Better comparison to experimental tests is needed. Differences between FEM results and experimental tests can be further analysed by adding a deformable luminal component to the current model and applying a pressure loading to the luminal surface, but only if more computational power is made available. Alternatively, a test will have to be developed which models the simplified loading conditions of the models.

Overall, it can be stated that the presented modelling approach lead to a better understanding of the complex mechanical behaviour of the wire support structures. There exists scope for future analyses by implementing the proposed modelling approach to investigate additional parameters helpful for further optimisation of the support structures and vascular grafts utilising these structures.

References

1. Tan, G. and Y. Liu, *Comparative study of deformation-induced martensite stabilisation via martensite reorientation and stress-induced martensitic transformation in NiTi.* Intermetallics, 2004. **12**: p. 373-381.

2. Migliavacca, F., L. Petrini, V. Montanari, I. Quagliana, F. Auricchio and G. Dubini, *A predictive study of the mechanical behaviour of coronary stents by computer modelling.* Medical Engineering and Physics, 2005. **27**: p. 12-18.

3. Migliavacca, F., L. Petrini, M. Colombo, F. Auricchio and R. Pietrabissa, *Mechanical behavious of coronary stents investigated through the finite element method.* Journal of Biomechanics, 2002. **35**: p. 803-811.

4. Dumoulin, C. and B. Cochelin, *Mechanical behaviour modelling of balloon-expandable stents.* Journal of Biomechanics, 2000. **33**: p. 1461-1470.

5. Etave, F., G. Finet, M. Boivin, J. Boyer, G. Rioufol and G. Tollet, *Mechanical properties of coranary stents determined by using finite element analysis.* Journal of Biomechanics, 2001. **34**: p. 1065-1075.

6. Walke, W., Z. Pazenda and J. Filipiak, *Experimental and numerical biomechanical analysis of vascular stent.* Journal of Materials Processing Technology, 2005. **164**: p. 1263-1268.

7. Lally, C., F. Dolan and P.J. Perendergast, *Cardiovascular stent design and vessel stresses: a finite element analysis.* Journal of Biomechanics, 2005. **38**: p. 1574-1581.

8. Petrini, L., F. Migliavacca, F. Auricchio and G. Dubini, *Numerical investigation of the intravascular coronary stent flexibility.* Journal of Biomechanics, 2004. **37**: p. 495-501.

9. Gong, X. and A.R. Pelton. *ABAQUS analysis on Nitinol medical applications*. in *ABAQUS User's Conference*. 2002.

10. Whitcher, F.D., *Simulation of in vivo loading conditions of Nitinol vascular stent structures.* Computers and Structures, 1997. **64**: p. 1005-1011.

11. Ross, J., *Cardiovascular system*, in *Physiological Basis of Medical Practice*, J.B. West, Editor. 1991, Williams and Wilkins: Baltimore.

12. Keener, J. and J. Sneyd, *Mathematical Physiology*. 1998, Springer-Verlag: New York.

13. BBC, Heart disease and stroke: The facts; http://news.bbc.co.uk/hi/english/static/in_depth/health/2000/heart_disease/default.stm; 2000.

14. Sherwood, L., *Human Physiology From Cells to Systems*. 5th edition ed. 2004, Thomson Learning Inc.

15. Vander, A., J. Sherman and D. Luciano, *Human Physiology*. 7th ed. 1998, McGraw-Hill.

16. WHHI, Circulatory system; http://www.whhi.com/circulatorysystem.htm;

17. Shadwick, R.E., *Mechanical design in arteries.* The Journal of Experimental Biology, 1999. **202**: p. 3305-3313.

18. Shadwick, R.E., *Elasticity in arteries.* American Scientist, 1998. **86**: p. 535.

19. Belz, G.G., *Elastic Properties and windkessel function of the human aorta.* Cardiovascular Drugs and Therapy, 1995. **9**: p. 73-83.

20. Nichols, W.W. and M. O'Rouke, *McDonald's Blood Flow in Arteries Theoretical Experimental and Clinical Principles*. 1998, Arnold.

21. O'Rourke, M., *Mechanical principles of arterial disease.* Hypertension, 1995. **26**: p. 2-9.

22. Holzapfel, G.A., T.C. Gasser and R.W. Ogden, *A new constitutive framework for arterial wall mechanics and a comparative study of material models.* Journal of Elasticity, 2000. **61**: p. 1-48.

23. Tiwari, A., K.S. Cheng, H. Salacinski, G. Hamilton and A.M. Seifalian, *Improving the patency of vascular bypass grafts: the role of suture materials and surgical techniques on reducing anastomotic compliance mismatch.* European Journal of Vascular and Endovascular Surgery, 2003. **25**: p. 287-95.

24. Seifalian, A.M., A. Giudiceandrea, T. Schmidz-Rixen and G. Hamilton, *Noncompliance: The silent acceptance of a villain*, in *Tissue Engineering of Prosthetis Vascular Grafts*, P. Zilla and P. Greisler, Editors. 1999

25. Walden, R., G.J. L'Italien, J. Mergerman and W.M. Abbott, *Matched elastic properties and successful arterial grafting.* Archives of Surgery, 1980. **115**: p. 1166-1169.

26. Tai, N.R., H.J. Salacinski, A. Edwards, G. Hamilton and A.M. Seifalian, *Compliance properties of conduits used in vascular reconstruction.* The British journal of Surgery, 2000. **87**: p. 1516-1524.

27. Yeoman, M.S., The Design and Optimisation of Fabric Reinforced Porous Prosthetic Grafts Using Finite Element Methods and Genetic Algorithms. in 2004,University of Cape Town:Cape Town.

28. Weiss, L. and R.O. Greep, *Histology*. 1977, McGraw-Hill.

29. Cox, J.L., D.A. Chiasson and A.I. Gotlieb, *Stranger in a strange land: the pathogenesis of saphenous vein graft stenosis with emphasis on structural and functional differences between veins and arteries.* Progress in Cardiovascular Diseases, 1991. **34**: p. 45-68.

30. Walls, E.W., *The blood vascular and lymphatic system*, in *Cunningham's textbook of anatomy*, G.J. Romanes, Editor. 1979, Oxford university press: London.

31. Schwartz, L.B., M.K. O'Donohoe, C.M. Purut, E.M. Mikat, P.O. Hagen and R.L. McCann, *Myointimal thickening in experimental vein grafts is dependent on wall tension.* Journal of Vascular Surgery, 1992. **15**: p. 176-86.

32. McGarry, J.P., B.P. O'Donnell, P.E. McHugh and J.G. McGarry, *Analysis of the mechanical performance of a cardiovascular stent design based on micromechanical modelling.* Computational Materials Science, 2004. **31**: p. 421-438.

33. Prendergast, P.J., C. Lally, S. Daly, A.J. Reid, T.C. Lee, D. Quinn and F. Dolan, *Analysis of prolapse in cardiovascular stents: A constitutive equation for vascular tissue and finite element modelling.* Transactions of the ASME, 2003. **125**(692-699).

34. Kohler, T.R., T.R. Kirkman and A.W. Clowes, *Effect of rigid external support on vein graft adaptation.* Journal of Vascular Surgery, 1989. **9**: p. 277-285.

35. Lemson, M.S., J.H. Tordoir, M.J. Daemen and P.J. Kitslaar, *Intimal hyperplasia in vascular grafts.* European Journal of Vascular and Endovascular Surgery, 2000. **19**: p. 336-350.

36. Bezuidenhout, D. and P. Zilla, *Vascular grafts.* Encyclopaedia of Biomaterials and Biomedical Engineering., 2004.

37. Burkel, W.E., *The challenge of small diameter vascular grafts.* Medical Progress through Technology, 1988. **14**: p. 165-175.

38. Loth, F., S.A. Jones, C.K. Zarins, D.P. Giddens, R.J. Nasser, S. Glagov and H.S. Bassiouny, *Relative contribution of wall shear stress and injury in experimental intimal thickening at PTFE end-to-side arterial anastomosis.* Transactions of the ASME, 2002. **124**: p. 44-51.

39. Mehta, D., M.B. Izzat, A.J. Bryan and G.D. Angelini, *Towards the prevention of vein graft failure.* International Journal of Cardiology, 1997. **62**: p. S55-S63.

40. Sata, M. and R. Nagai, *Origin of neointimal cells in autologous vein graft.* Arteriosclerosis, Thrombosis, and Vascular Biology, 2004. **24**: p. 1147-9.

41. Surovtsova, I., *Effects of compliance mismatch on blood flow in an artery with endovascular prosthesis.* Journal of Biomechanics, 2005. **38**: p. 2078-2086.

42. Uchida, N., H. Kambic, H. Emoto, J. Chen, S. Hsu and S. Murabayshi, *Compliance effects on small diameter polyurethane graft patency.* Journal of Biomedical Materials Research, 1993. **27**: p. 1269-1279.

43. Salacinski, H.J., S. Goldner, A. Giudiceandrea, G. Hamilton, A.M. Seifalian, A. Edwards and R.J. Carson, *The mechanical behaviour of vascular grafts: a review.* Journal of Biomaterials Applications, 2001. **15**: p. 241-278.

44. Sarkar, S., H.J. Salacinski, H. G. and A.M. Seifalein, *The mechanical properties of infraiguinal vascular bypass grafts: Their role in influencing patency.* European Journal of Vascular and Endovascular Surgery, 2006. **31**: p. 629-636.

45. Kidson, I.G., *The effect of wall mechanical properties on patency of arterial grafts.* Annals of the Royal College of Surgeons of England, 1983. **65**: p. 24-29.

46. Gupta, B.S. and V.A. Kasyanov, *Biomechanics of human common carotid artery and design of novel hybrid textile compliant vascular grafts.* Journal of Biomedical Materials Research, 1997. **34**: p. 341-349.

47. Kinley, C.E. and A.E. Marble, *Compliance: A continuing problem.* Journal of Cardiovascular Surgery, 1980. **21**: p. 163-170.

48. Lei, M., J.P. Archie and C. Kleinstreuer, *Computational design of a bypass graft that minimizes wall shear stress gradients in the region of distal anastomosis.* Journal of Vascular Surgery, 1997. **25**: p. 637-346.

49. Dobrin, P.B., *Mechanical factors associated with the development of intimal and medial thickening in vein grafts subjected to arterial pressure.* Hypertension, 1995. **26**: p. 38-43.

50. Dobrin, P.B., F.N. Littooy and E.D. Endean, *Mechanical factors predisposing to intimal hyperplasia and medial thickening in vein grafts.* Surgery, 1989. **105**: p. 393-400.

51. Zwolak, R.M., M.C. Adams and A.W. Clowes, *Kinetics of vein graft hyperplasia: association with tangential stress.* Journal of Vascular Surgery, 1987. **5**: p. 126-136.

52. Krejca, M., J. Skarysz, P. Szmagala, D. Plewka, G. Nowaczyk, A. Plewka and A. Bochenek, *A new outside stent - Does it prevent graft intimal proliferation.* European Journal of Cardio-Thoracic Surgery, 2002. **22**: p. 898-903.

53. Stooker, W., M. Gok, P. Sipkema, H. Niessen, A. Baidoshvili, N. Westerhof, E.K. Jansen, C.R.H. Wildevuur and L. Eijsman, *Pressure-diameter relationship in the human greater saphenous vein.* Annals of Thoracic Surgery, 2003. **76**: p. 1533-1538.

54. Huynh, T.T.T., M.G. Davies, M.J. Trovato, E. Svendsen and P.O. Hagen, *Alterations in wall tension and shear stress modulate tyrosine kinase signalling and wall remodelling in experimental vein grafts.* Journal of Vascular Surgery, 1999. **29**: p. 334-344.

55. Pedrizzetti, G., F. Domenichini, A. Tortoriello and L. Zovatto, *Pulsitile flow inside moderately elastic arteries, its modelling and effects of elasticity.* Computer Methods in Biomechanics and Biomedical Engineering, 2002.

56. Qiu, Y. and J.M. Tarbell, *Interaction between Wall Shear Stress and Circumferential Strain Affects Endothelial Cell Biochemical Production.* Journal of Vascular Research, 2000. **37**: p. 147-157.

57. Nwasokwa, O.N., *Coronary artery bypass graft disease.* Annals of Internal Medicine, 1995. **123**: p. 528-545.

58. Kowligi, R.R., W.W. von Maltzahn and R.C. Eberhart, *Fabrication and characterization of small-diameter vascular prosthesis.* Journal of Biomedical Materials Research, 1988. **22**: p. 245-256.

59. Dashwood, M.R., G.D. Angelini, S. Wan, A. Yim, D. Mehta, M.B. Izzat and J.Y. Jeremy, *Does external stenting reduce porcine vein-graft occlusion via an action on vascular nerves?* Journal of Cardiovascular Surgery, 2002. **17**: p. 556-560.

60. Sajja, L.R., G. Mannam, N.R. Pantula and S. Sompalli, *Role of radial artery graft in coronary artery bypass grafting.* Annals of Thoracic Surgery, 2005. **79**: p. 2180-2188.

61. Schaner, P.J., N.D. Martin, T.N. Tulenko, I.M. Shapiro, N.A. Tarola, R.F. Leichter, R.A. Carabasi and P.J. DiMuzio, *Decellularized vein as a potential scaffold for vascular tissue engineering.* Journal of Vascular Surgery, 2004. **40**: p. 146-153.

62. Bos, G.W., A.A. Poot, T. Beugeling, W.G. van Aken and J. Feijen, *Small-diameter vascular graft prosthesis: Current status.* Archives of Physiology and Biochemistry, 1998. **106**: p. 100-115.

63. Batellier, J., M. Wassef, R. Merval, M. Duriez and A. Tedgui, *Protection from atherosclerosis in vein grafts by rigid external support.* Arteriosclerosis, Thrombosis, and vascular biology, 1993. **13**: p. 379-384.

64. Mehta, D., S.J. George, J.Y. Jeremy, M.B. Izzat, K.M. Southgate, A.J. Bryan, A.C. Newby and G.D. Angelini, *External stenting reduces long-term medial and neointimal thickening and platelet derived growth factor expression in a pig model of arteriovenous bypass grafting.* Nature Medicine, 1998. **4**: p. 235-239.

65. Dobrin, P.B., F.N. Littooy, J. Golan, B. Blakeman and J. Fareed, *Mechanical and histological changes in canine vein grafts.* The Journal of Surgical Research, 1988. **44**: p. 259-265.

66. Angelini, G.D., C. Lloyd, R. Bush, J. Johnson and A.C. Newby, *An external, oversized, porous polyester stent reduces vein graft neointima formation, cholesterol concentration, and vascular cell adhesion molecule 1 expression in cholesterol-fed pigs.* Journal of Thoracic and Cardiovascular Surgery, 2002. **124**: p. 950-956.

67. de Feyter, P.J., *Percutaneous treatment of saphenous vein bypass graft obstructions: a continuing obstinate problem.* Circulation, 2003. **107**: p. 2284-2286.

68. Thomas, A.C., G.R. Campbell and J.H. Campbell, *Advances in vascular tissue engineering.* Cardiovascular Pathology, 2003. **12**: p. 271-276.

69. Vara, D.S., H.J. Salacinski, R.Y. Kannan, L. Bordenave, G. Hamilton and A.M. Seifalian, *Cardiovascular tissue engineering: state of the art.* Pathologie-Biolgie, 2005. **53**: p. 599-612.

70. Martz, H., G. Beaudoin, R. Paynter, M. King, D. Marceau and R. Guidoin, *Physiochemical characterization of a hydrophilic microporous polyurethane vascular graft.* Journal of Biomedical Materials Research, 1987. **21**: p. 399--412.

71. Muller-Glauser, W., K.H. Lehmann, P. Bittmann, U. Bay, P. Dittes, L. von Segesser and M. Turina, *A compliant small diameter vascular prosthesis lined with functional venous endothelial cells.* ASAIO Transactions, 1988. **34**: p. 528-531.

72. Mattsson, E.J., T.R. Kohler, S.M. Vergel and A.W. Clowes, *Increased blood flow induces regression of intimal hyperplasia.* Arteriosclerosis, Thrombosis, and Vascular Biology, 1997. **17**: p. 2245-2249.

73. Meguro, T., H. Nakashima, S. Kawada, K. Tokunaga and T. Ohmoto, *Effect of external stenting and systemic hypertension on intimal hyperplasia in rat vein grafts.* Neurosurgery, 2000. **46**: p. 963-969; Discussion 969-970.

74. Nagahama, H., Y. Fukushima, T. Hayase, M. Yoshioka and T. Onitsuka, *Reinforcement of saphenous vein graft with ePTFE graft for auxillocoronary bypass grafting.* The Annals of Thoracic Surgery, 2005. **79**: p. 700-701.

75. Brinson, C., I. Schmidt and R. Lammering, *Stress-induced transformation behaviour of a polycrystalline NiTi shape memory alloy: micro and macro-mechanical investigations via in situ optical microscopy.* Journal of the Mechanics and Physics of Solids, 2004. **52**: p. 1549-1571.

76. Meissner, S., On Constitutive Modelling of Shape Memory Alloys within the Finite Element Method. in Engineering,2004,Technical University of Munich:Munich.

77. Shaw, J.A. and S. Kyriakides, *Thermomechanical aspects of NiTi.* Journal of the Mechanics and Physics of Solids, 1995. **43**: p. 1243-1281.

78. Ryhänen, J., Biocompatibility evaluation of nickel-titanium shape memory metal alloy. in Departments of Surgery, Anatomy and Pathology,1999,Oulu University:Oulu.

79. Auricchio, F., R.L. Taylor and J. Lubliner, *Shape-memory alloys: Macromodelling and numerical simulations of the superelastic behaviour.* Computer Methods in Applied Mechanics and Engineering, 1997. **146**: p. 281-312.

80. Auricchio, F. and R.L. Taylor, *Shape-memory alloys: Modelling and numerical simulations of the finite-strain superelastic behaviour.* Computer Methods in Applied Mechanics and Engineering, 1997. **143**: p. 175-194.

81. Gall, K., J. Tyber, V. Brice, C.P. Frick, H.J. Maier and N. Morgan, *Tensile deformation of NiTi wires.* Journal of Biomedical Materials Research, Part A, 2005. **75**: p. 810-823.

82. Rebelo, N. and M. Perry, *Finite element analysis for the design of Nitinol medical devices.* Minimally Invasive Therapy and Applied Technologies, 2000. **9**: p. 75-80.

83. McNaney, J.M., V. Imbeni, Y. Jung, P. Papadopoulos and R.O. Ritchie, *An experimental study of the superelastic effect in a shape-memory Nitinol alloy under biaxial loading.* Mechanics of Materials, 2003. **35**: p. 969-986.

84. Liu, Y., Z. Xie, J. Van Humbeeck and L. Delaey, *Some results on the detwinning process in NiTi shape memory alloys.* Scripta Materialia, 1999. **41**(12): p. 1273-1281.

85. Malvern, L.E., *Introduction to the mechanics of a continuum*, Prentice-Hall.

86. Lai, W.M., D. Rubin and E. Krempl, *Introduction to Continuum Mechanics*, Pergamon Press.

87. Lubliner, J. and F. Auricchio, *Generalized plasticity and shape memory alloys.* International Journal of Solids and Structures, 1996. **33**: p. 991-1003.

88. Desai, C.S., *Introduction to the finite element method: a numerical method for engineering analtsis*. 1972, Van Nostrand Reinhold: New York.

89. Hughes, J.R., *The Finite Element Method: Linear Static and Dynamic Finite Element Analysis*, Prentice-Hall.

90. David Chua, S.N., B.J. Mac Donald and M.S.J. Hashmi, *Finite element simulation of stent balloon interaction.* Journal of Materials Processing Technology, 2003. **143**: p. 591-597.

91. Holzapfel, G.A., *Changes in the mechanical environment of stenotic arteries during interaction with stents: Computational assessment of parametric stent designs.* Transactions of ASME, 2005. **127**.

92. Perry, M., S. Oktay and J.C. Muskivitch, *Finite element analysis and fatigue of stents.* Minimally Invasive Therapy and Applied Technologies, 2002. **11**: p. 165-171.

93. Rebelo, N., N. Walker and H. Foadian. *Simulation of implantable Nitinol stents.* in *ABAQUS user's conference*. 2001.

94. Franz, T., *Personal Communications*. 2006: Cardiovascular Research Unit, University of Cape Town.

95. Wolf, M.F., *Personal Communications*. 2006: Medtronic Inc., Minneapolis, MN.

96. David Chua, S.N., E.J. Mattsson and M.S.J. Hashmi, *Finite-element simulation of stent expansion.* Journal of Materials Processing Technology, 2002. **120**: p. 335-340.

97. Liang, D.K., D.Z. Yang, M. Qi and W.Q. Wang, *Finite element analysis of implantation of a balloon-expandable stent in a stenosed artery.* Internal Journal of Cardiology, 2005. **104**: p. 314-318.

98. Tan, G. and Y. Liu, *Comparative study of deformation-induced martensite stabilisation via martensite reorientation and stress-induced martensitic transformation in NiTi.* Intermetallics, 2004. **12**(4): p. 373-381.